Paleoenvironmental Reconstruction from Lake Sediments of Lago Cástor, North Patagonian Andes

Master's thesis

Faculty of Science
University of Bern

presented by

Richard Wartenburger

2010

Supervisor:
Prof. Dr. Martin Grosjean

Advisor:
Julie Elbert

Department of Geography &
Oeschger Center for Climate Change Research

University of Bern

Acknowledgements

First of all, I would like to thank Prof. Dr. Martin Grosjean for the support and supervision of my Thesis. He was always available to give detailed answers to my questions, and provided meaningful suggestions in difficult situations. Special thanks also go to my advisor Julie Elbert, who was always around to assist me in the laboratory, and contributed to convenient working conditions throughout the entire last year. Foremost, this Thesis was facilitated by the technical environment provided within the Lake sediment and Paleolimnology research group at Uni Bern. Many thanks go to Dr. Daniela Fischer, who provided great help with the lab facilities and was able to give qualified answers to any of my methodological questions.

I am very thankful to all personnel who contributed indirectly to this work by their great efforts – Marian Fujak (Eawag Dübendorf) for lead-210 dating, Tomasz Goslar and his team (Poznan Radiocarbon Laboratory) for AMS radiocarbon dating, Prof. Vincent Serneels (Dept. of Geosciences, University of Fribourg) as well as Prof. Ivan Mercolli and his team (University of Bern) for their help with the sample preparation and realization of the XRF analysis, Prof. Dr. Gerald Haug and his team for the XRF scan and for help with the grain size measurements, and again Martin Grosjean and Julie Elbert for their work in the field.

I am also very grateful for the numerous suggestions and advices by the team of the Lake sediment and Paleolimnology group (University of Bern). In particular, I want to thank my colleague, friend and room mate Fabian Mauchle for the never-ending exchange of ideas and experience. Last but not least, I am also very happy for the sound atmosphere within the office, which my other room mates Rie Nemoto and Samuel Hagnauer have clearly contributed to, as well as for the nice coffee and lunch breaks with the group, that were an indispensable add-on for the success of this Thesis.

Abstract

Despite substantial advancements in recent years, large parts of Southern South America still have the characteristics of a "terra incognita" in terms of reliable high resolution quantitative climate reconstructions. When looking at smaller scales, there are also considerable gaps of knowledge concerning detailed knowledge on land use changes. This study aims at filling these gaps with a paleoenvironmental reconstruction from lake sediments of Lago Cástor (45.3°S, 71.5°W), spanning the last 4000 years at decadal to sub-centennial resolution. Lead-210 and AMS radiocarbon dates were used for age model construction. Chronostratigraphic markers were applied to constrain and extend the model. Special emphasis was placed on volcanic tephra layers of known deposition age. Chemical sediment composition was determined by qualitative X-Ray Fluorescence (XRF) core scanning and semi-quantitative XRF analysis of potential tephra deposits. A set of three geochemical proxies (carbon-to-nitrogen ratio, biogenic silica flux, and grain size distribution) was analysed with respect to paleoenvironmental conditions of the last 500 – 1500 years. In-situ reflectance spectroscopy was applied to calculate additional paleoenvironmental proxies. The results were compared with climate data (temperature, precipitation, and circulation indices), as well as with historical records of regional land use change. Principal component analysis (PCA) and ordinary correlation analysis were applied to structure and analyse the data. One of the tephra deposits was identified as eruptive material from the second major Holocene eruption of the Hudson volcano (H2, 3600 yr BP), facilitating an extension of the age model. The C/N records showed a distinctive trough over the last decades, strongly suggesting a link to pronounced land use change in the catchment. Those results were largely supported by the XRF-derived proxies and by mean grain size. The findings were consistent with documentary sources. Biogenic silica flux and grain size followed temperature and precipitation trends with only minor deviations, demonstrating local evidence for the widespread AD 1976 climate shift. As those proxy records appear to be valid predictors for paleoclimate conditions in the studied lake, it may be of huge interest to extend them further back in time.

Contents

List of Figures

Nomenclature

Roman Symbols

a.s.l.	above sea level
AAO	Antarctic Oscillation
AAPO	Antarctic Pacific Oscillation
AD	anno Domini (Latin, after Christ)
Al, Ca, ...	chemical element notations according to the periodic table of the elements
AMS	Accelerator Mass Spectrometry
B.C.	Before Christ
BAS	British Antarctic Survey
BP	Before Present (= before AD 1950). If not denoted with a leading *cal.*, the corresponding years are uncalibrated radiocarbon years BP.
BSi	biogenic silica
ca.	circa
cal.	calibrated
CDM	cumulated dry matter
cf.	confer (Latin, compare)
CIE_l*a*b*	lab colour space
CONAF	Corporación Nacional Forestal
cps	counts per second
CRU	Climatic Research Unit, University of East Anglia
CRU TS3.0	monthly gridded temperature & precipitation data, Climatic Research Unit, University of East Anglia
CRUTEM3	data set on land air temperature, Climatic Research Unit

DJF	December, January, February
e.g.	exempli gratia (Latin, for example)
ENSO	El Niño-Southern Oscillation
ESRL	NOAA Earth System Research Laboratory
hPa	hectopascal
i.e.	id est (Latin, that is)
ibid.	ibidem (Latin, at the same place)
JISAO	Joint Institute for the Study of the Atmosphere and Ocean
JJA	June, July, August
LGM	Last Glacial Maximum
LIA	Little Ice Age
LOFZ	Liquiñe-Ofqui Fault Zone
LSi	Lithogenic Silica
MAM	March, April, May
MAR	mass accumulation rate
MEI	Multivariate ENSO index
NA	not available
NH	Northern Hemisphere
no.	number
NOAA	National Oceanic and Atmospheric Administration
P	precipitation
p.a.	per annum (Latin, per year)
PC	principal component
PCA	principal component analysis
PDO	Pacific Decadal Oscillation
PSD	Physical Science Division at NOAA
PSD	particle size distribution
RGB	red-green-blue colour space
rpm	rounds per minute
SAM	Southern Hemisphere Annular Mode
SCP	spheroidal carbonaceous particle
SH	Southern Hemisphere
SLP	sea level pressure
SOI	Southern Oscillation Index

SON	September, October, November
SST	sea surface temperature
SVZ	Southern Andean Volcanic Zone
T	temperature
XRF	X-Ray Fluorescence
yr	year

1. Introduction

1.1 Motivation and Research Question

Lake sediments are an excellent archive to study long-term fluctuations of environmental conditions (e.g. von Gunten et al. 2009a). In contrast to pollen and tree ring series, this archive has the potential to preserve long-term climate signals (e.g. Moberg et al. 2005). In addition to that, the sediments may directly preserve environmental indicators such as tephra deposits (e.g. Bertrand et al. 2008b). In this Thesis, the term paleoenvironmental conditions is used in terms of the history of climatic conditions, past anthropogenic alterations of the natural landscape, as well as the history of volcanic impacts.

Paleoenvironmental research in Southern South America is very valuable, as this region still lacks of a coherent network of paleoenvironmental data (Neukom et al. 2010b, von Gunten et al. 2009a). This fact is regarded as an incisive bottleneck in paleoclimate research, as Southern South America is a key area to study climate variability (Aravena & Luckman 2009). The spatial distribution of proxy records in this region reveals a distinct lack of paleoenvironmental studies apart from those based on tree rings (see figure 1.1). The urgent need for alternative paleoenvironmental research combined with their sheer absence in parts of South America is a strong motivation for this study. By extending the network of existing paleoclimate records, this Thesis has the potential to increase knowledge on climate variability in the study region, indirectly contributing to the ongoing research on global Climate Change (Solomon 2007). Besides that, the Thesis will shed light on the timing and extent of regional non-climatic environmental change.

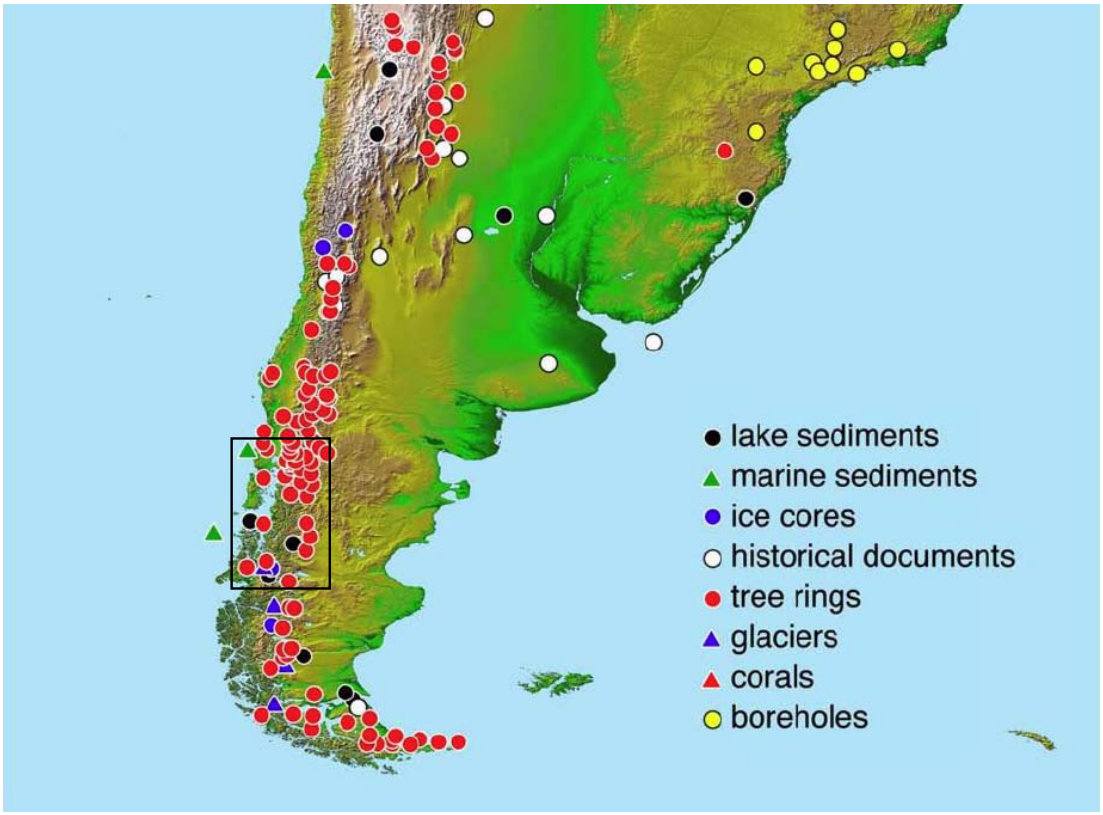

Figure 1.1: Spatial distribution of proxy records across Southern South America, based on data contributed to the LOTRED-SA initiative. The proxy records displayed in the Figure represent the work of many investigators during the past 3-4 decades. Background image from NASA/JPL/NIMA. The black square indicates the approximate location of the wider study area. Graphic adapted from Villalba et al. 2009.

This Master Thesis is supervised by Professor Dr. Martin Grosjean, head of the Oeschger Centre for Climate Change Research (OCCR) and head of the Lake Sediment and Paleolimnology group at the Institute of Geography, University of Bern. The Thesis is assisted by Julie Elbert, who is member of the same research groups. She works for the SNSF division II project "Scanning in-situ reflectance spectroscopy as a novel tool for high-resolution climate reconstructions from lake sediments, southern Chile" (project no. NF 200020_121869). The project builds on the solid foundation of previous and current achievements by the research group in paleoclimate research in Chile. Its research follows two major thrusts in methodology and data. The aim of the data component is to produce a number of

temperature and / or precipitation reconstructions from lake sediments with the aim (i) to better assess the local to regional expression of climate variability during the past 1000 years, (ii) to contribute to the international regional multi-proxy climate reconstruction of South America in IGBP-PAGES LOTRED-SA, and (iii) to assess the sensitivity of the local to regional climate system to forced and unforced perturbations at a variety of temporal scales. This work will contribute to meet these goals.

This study will examine the past 4000 years at a decadal to sub-centennial resolution. The spatial extent is roughly limited to the wider study area, which was defined as the region between (70°W, 40°S) and (75°W, 50°S). This area contains basically the Chilean part of North Patagonia, including a section of the Pacific coast and westernmost Argentina (see Figure 2.2 on page 13). To sum up the aims of this study, two research questions are formulated.

1. How did the environmental conditions in the catchment of Lago Cástor evolve throughout the Late Holocene?

2. How do the results of this study compare with studies and datasets from within the wider study area?

In order to answer these questions, it was necessary to develop a proper age model by the use of lead-210 dating, radiocarbon dating and tephrochronology, which allowed the attribution of a probabilistic age for a given total sediment depth. On the other hand, a set of geochemical indicators was used to obtain proxy-based information of environmental conditions. Having that information, trends and variability of the environmental parameters over time was assessed. The results were then compared with a number of recent publications and datasets, which are listed in the next paragraphs.

1.2 State of Knowledge

This section gives a brief review on the results of the most recent major paleoenvironmental studies in the wider study area that at least span a fraction of the time period analysed in this study (see constrictive geographical and temporal definitions above). This overview focusses on the principal thrusts and aims of this study, namely the volcanic history, paleoclimate, and history of land use change within the wider study area. Studies which focus on methodological aspects that are of interest for this study are mentioned in the corresponding sections of chapter 3. The studies presented here were used for the discussion of the results in section 5.3.

1.2.1 Volcanic History

Figure 2.2 (p. 13) shows the locations of all volcanoes within the central part of the wider study area. Volcanoes outside this region are not relevant for this study, as their eruption plumes did never move as far South as the latitude of the study site (e.g. Naranjo & Stern 1998). According to the relative location of these volcanoes to the study site, the likelihood to find tephra deposits originating from these volcanic centres is substantial. Two tephra deposits with probable occurrence in the study area are described in the following paragraphs.

The Hudson Volcano (numbered as volcano 1 in Figure 2.2) belongs to one of the most prominent and most active stratovolcanoes of the Southern Andean Volcanic Zone (SVZ; Naranjo & Stern 2004). At the same time, it is the southernmost volcano of the SVZ (Naranjo & Stern 1998). It has recently been active, with three minor eruptions in the last 40 years (Gutiérrez et al. 2005). Contrary to those low-magnitude eruptions, the tephra deposits from two large Holocene eruptions dating to approximately 6700 yr BP ("H1") and 3600 yr BP ("H2") may be preserved in terrestrial or lacustrine sediments (Naranjo & Stern 1998). Those deposits cover extensive areas within the wider study area (ibid.). According to Naranjo & Stern 1998, the 3600 BP tephra can potentially be traced at the study site, having a thickness in between 5 and 10 cm and an average grain size of less than 2 cm (the precise value of this parameter is unknown).

Furthermore, Naranjo & Stern 1998 characterized this tephra as yellowish-white ash, bracketed between > 3495 and < 3670 yr BP.

Other volcanic events with potential relevance for the study area may be eruptions of the stratovolcanoes to the northwest of the study site, namely Macá, Cay, Mentolat, Melimoyu, and Yanteles (from south to north; locations are presented in Figure 2.2). Eruption material of those volcanoes may potentially have settled in the lake sediments of Lago Cástor, as the dominant dispersion of tephra produced by explosive eruptions is to the southeast, reflecting high-altitude wind directions (Naranjo & Stern 2004). But except for Macá, none of those volcanoes show evidence of Late Holocene eruptions with impact on the study area (Naranjo & Stern 2004). An explosive eruption of the this volcano occurred at around 1540 yr BP, distributing greyish basaltic-andesitic material towards the east, thus towards the study site (Naranjo & Stern 2004).

Apart from the publications mentioned above, further tephrochronological studies (Kilian et al. 2003, Stern et al. 2007, Oyarzun et al. 2007, and Markgraf et al. 2003) were used as references for the tephra comparison in section 5.1. All the studies present chemical compositions and macroscopic descriptions of tephra deposits from the volcanoes mentioned above, and provide a deposition age for several of them.

1.2.2 Paleoclimate

Recent and past South American climate is largely characterized by its unique location and land-ocean distribution on the Southern Hemisphere, triggering an amplification of large-scale climate oscillators and modes (see 2.4). This dependency was detected already for the early to mid Holocene, showing large latitudinal shifts in the Hadley cell circulation (Lamy et al. 2001), accompanied by cool and wet conditions around 3000 cal. yr BP in North Patagonia (Abarzua et al. 2004). Since then, modern Holocene (i.e. stable) conditions were generally present in the wider study area and beyond (e.g. Jenny et al. 2003). Still, numerous climatic fluctuations within this period were detected (Markgraf et al. 2003). As paleoclimate proxy records of this Thesis cover the time frame of the last 2000 years, climatic variations within this time span shall be discussed in

greater detail. Figure 1.2 gives an overview of relevant climatic variations as summarized from selected sources of literature that are briefly presented in the next paragraph. Note that some of the sources are reviews of several climate reconstructions with validity for the given region.

Haberzettl et al. 2005 and Boninsegna et al. 2009 reviewed a number of paleoclimatic studies, presenting variations in temperature and precipitation. Neukom et al. 2010a and Neukom et al. 2010b reconstructed precipitation and temperature of Southern South America from various high-quality climate archives. Distinct positive and negative deviations with respect to mean temperature and precipitation at the location of the study site were included into Figure 1.2. Late Holocene conditions of southern Chile have been extensively studied in recent years. Morales et al. 2009 summarized late Holocene cycles of wet and dry conditions and the approximate timing of the Medieval Climate Anomaly (MCA) and the Little Ice Age (LIA) in southeast Patagonia as shown in Figure 1.3. In Figure 1.2, the MCA corresponds to the dry and warm anomaly roughly AD 1100 – AD 1250, whereas the cold period from AD 1340 till AD 1650 (bold line in Figure 1.2) is concurrent with LIA glacial events registered in the Northern Hemisphere (Boninsegna et al. 2009).

Focussing on the climate evolution during the last century in the northern part of the wider study area, Bown & Rivera 2007 saw a decrease in precipitation from AD 1970 till today, while detecting marginal cooling near sea level but distinctive warming of the free atmosphere from AD 1958 till AD 2000. This pattern is highly related to recent cooling trends of the southeastern Pacific. However, this was not recorded in radiosonde data from Puerto Montt (41°S), which show marginal cooling over the whole of the troposphere (Falvey & Garreaud 2009). The low-level cooling trend coincided with the slightly negative, but non-significant temperature trend of -0.4°C of Puerto Aysén between AD 1960 and AD 1992 (Rosenbluth et al. 1997). A sharp increase in temperature simultaneous to a drop in precipitation was recorded in synchronicity with the AD 1976 climatic shift (Bown & Rivera 2007). This shift was contributed to an abrupt increase in sea surface temperatures (SSTs) in the span of about 1 year (Giese et al. 2002). It showed pronounced impacts on parts of North Patagonia (Aravena & Luckman 2009).

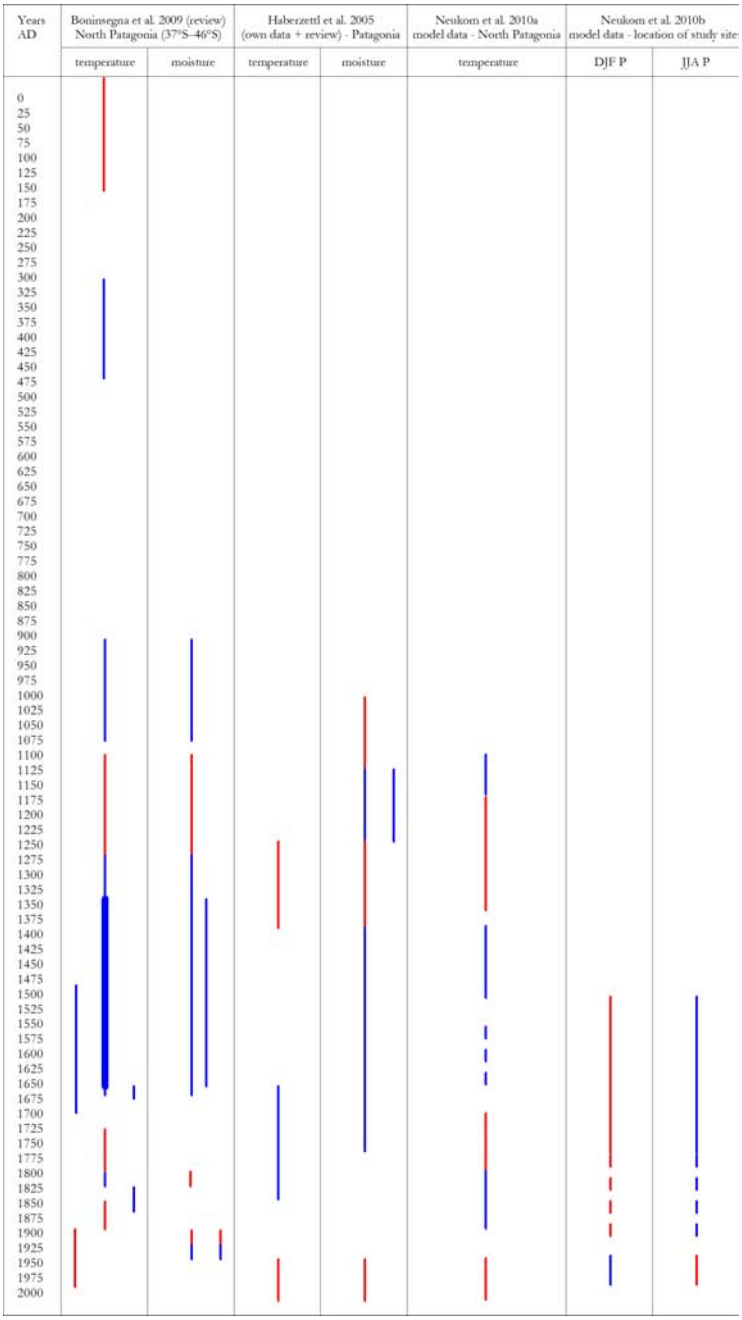

Figure 1.2: Summary of climatic conditions over the past 2000 years obtained from various paleoclimate studies. The underlying data are not claimed to be exhaustive. Results are valid for the regions given in the corresponding columns. Colour coding: blue = cold / wet, red = warm / dry (relative to the average temperature or moisture / precipitation). Broad bars represent core periods of a given climatic condition.

Despite these short-term fluctuations, the overall Holocene pattern of climatic belts in Chile remained essentially similar to modern conditions, implying that the precipitation distribution in southern Chile has basically remained the same (Clapperton 1994). The modern climate, including general climatic settings and atmospheric conditions, as well as major oscillations and modes with relevance for Southern South America, is presented in section 2.4. The observation datasets of temperature and precipitation for use in this study are presented in section 3.12.

Figure 1.3 illustrates and summarizes the impacts of some of the above-mentioned shifts in hydrological conditions on the cultural history of Patagonia, also showing major changes in the moisture regime back to 4000 cal. yr BP. The history of land use change in the wider study area is described in the next section.

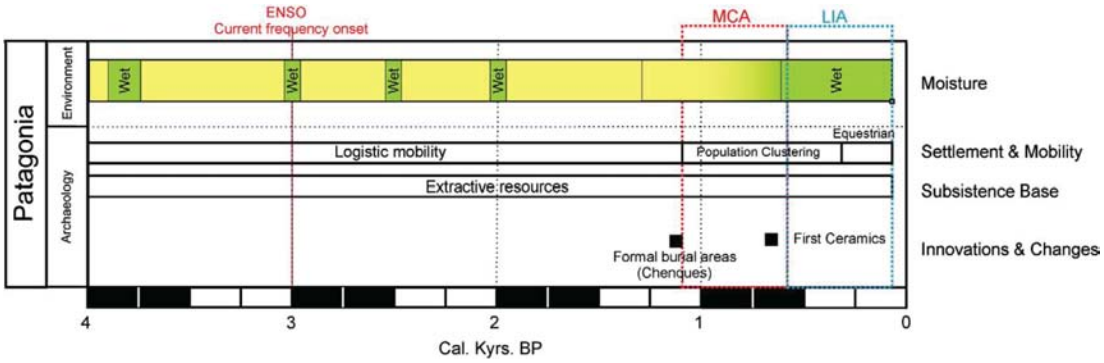

Figure 1.3: Archaeological and environmental indices of the late Holocene in Patagonia. The approximate time of the MCA and the LIA as well as the onset of the El Niño-Southern Oscillation (ENSO) are indicated in colour. Figure adapted from Morales et al. 2009.

1.2.3 Anthropogenic Land Use Change

Over only a fraction of the investigation period, the study site underwent substantial changes in land use. Prior to emerging presence of non-indigenous peoples, the pristine landscape at the study site was dominated by the main representative of the native North Patagonian forest type (Nothofagus Pumilio) and to a minor extent by Nothofagus Antarctica (Abarzua et al. 2004, Neves et al. 2008). Besides natural low-amplitude variability due to climatically induced fire activity during the Early and late Holocene, North Patagonian natural vegetation cover was increasingly affected by human interventions (Kitzberger & Veblen 2003). A modern vegetation signal was initially detected at around 700 cal. yr BP in many places in Patagonia, which was most likely introduced by human disturbance of the pre-Hispanic indigenes (ibid.). These native people were hunters and gatherers (ibid.). Until the year of independence in AD 1810, colonization of the area south of 38°S by European settlers was only marginal (Neves et al. 2008). In the present Coyhaique region, the first settlers arrived by the end of the 19th century, closely followed by the foundation of the municipality of Coyhaique in AD 1929 (Municipalidad de Coihaique, - 2010). Despite the colonization and its immense impact on the pristine landscape (see next paragraph), the environment of Lago Cástor and surrounding areas remained mainly unperturbed by human settlements until today (see photograph in Figure 2.1 on page 12). The only known published analysis of lake sediment records from Lago Cástor concludes that this lake was most likely not influenced by industrial activity (Urrutia et al. 2002). Enhanced pollutant concentrations of presumably natural origin were only discovered for Zinc (ibid.).

In the Aysén basin, a large-scale decline of native vegetation to half of the unperturbed population is focused on the period AD 1936 – 1956, stimulated by governmental initiatives (ibid., Quintanilla 2008). The land was cleared by pioneers and increasingly by companies primarily to establish pastures for cattle and sheep and to export timber (Veblen et al. 1992, Armesto et al. 2010). This ultimately lead to a sharp increase in erosive processes accompanied by soil loss and an increased probability of land slides (Quintanilla 2008). According to Neves et al. 2008, the study site was strongly affected by forest clearing (probably excluding the steep hill slopes), and was hence potentially also affected by increased erosion.

Despite governmental efforts, the majority of cattle farms went bankrupt due to an overestimation of the capacity of the soil to sustain productive pasture lands (Neves et al. 2008). By the late 20^{th} century, a vast reforestation programme was initiated by the Chilean government and the Corporación Nacional Forestal (CONAF) to solve the emerging environmental issues (Quintanilla 2008). Plantations are to almost 90 % pine monocultures, as the reforestation aimed at compensating for the slow natural regrowth of the native species (ibid.). In the Aysén basin, reforestation programmes were initiated in AD 1984 (ibid.).

The sum of land use impacts lead to characteristic patterns in vegetation cover that dominate in the catchment of Lago Cástor today (see Figure 2.1; Neves et al. 2008). It is therefore anticipated likely, that the dramatic shifts in vegetation and land use are recorded in the lake sediment records of Lago Cástor.

2. Lago Cástor

This chapter provides an overview of Lago Cástor and its environment. The topic of this chapter ranges from a brief description of the geographic and geologic settings down to the characteristics of the studied lake. To facilitate the discussion of the results, the present climatic conditions of the wider study area are described in greater detail. Figure 2.1 shows a picture of Lago Cástor to get a first impression of the lake.

2.1 Geography

Lago Cástor is located in the XI administrative region of Chile (Aísen region) in the Coyhaique province, at about 45.3°S, 71.5°W. The lake catchment belongs to the Aysén basin, which is part of North Patagonia (cf. Figure 2.2). It is adjacent to the Chilean-Argentinian border. The lake level is at an elevation of 725 m a.s.l., and the maximum depth of the lake reaches 52 m below water surface (Urrutia et al. 2002). By using the spatial statistics tools in ArcGIS®, the lake area was estimated to 4.26 km^2, and the calculated catchment area to a total of 24.5 km^2. These estimates are in rough accordance with the numbers given in Urrutia et al. 2002.

Figure 2.1: Picture of Lago Cástor and parts of its catchment. Dominant tree species are cultivated pines. Vegetation cover features large treeless patches, partly with visible signs of erosion. Picture taken during the field trip in January 2009 by Julie Elbert. Location of the photographer is at the southwestern edge of the lake, angle of view is east-northeast.

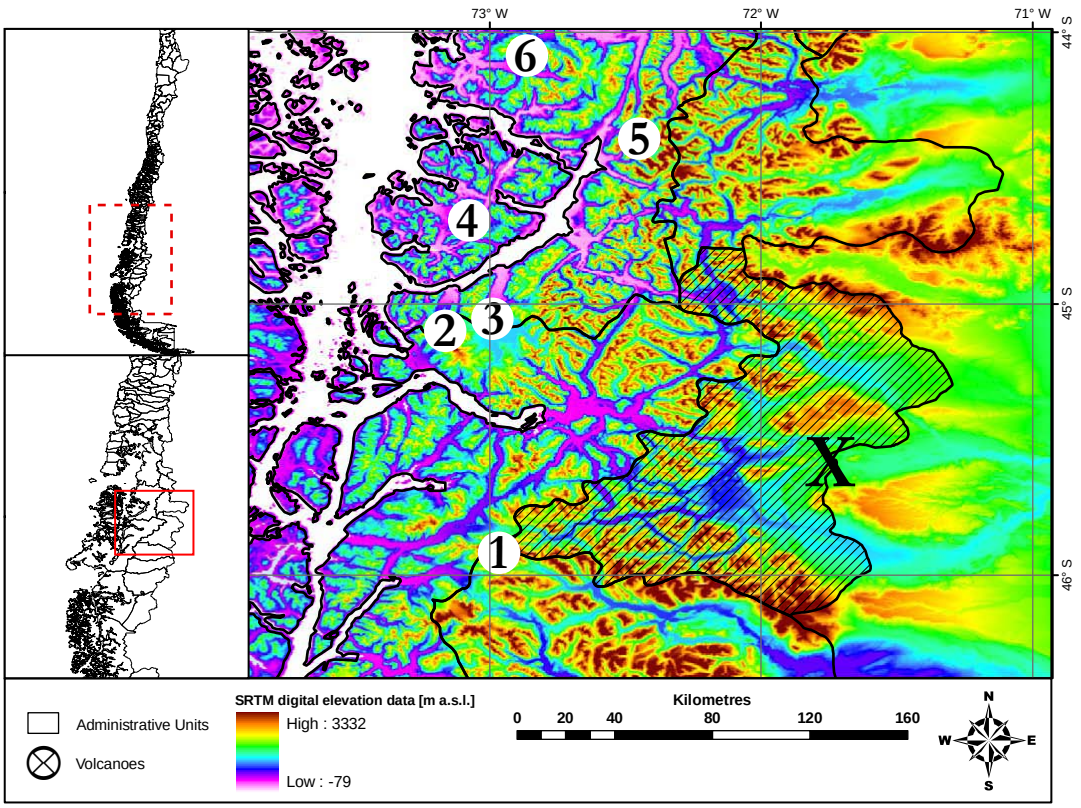

Figure 2.2: Location map of the study site. Maps on the left show the outline of Chile and its administrative provinces, the red rectangles frame the outline of the maps in higher zoom level. The Coyhaique province is highlighted with diagonal shading. The X marks the location of the study site. Also shown are volcanoes in the windward direction of Lago Cástor between latitudes 44°S and 46°S (from south to north: (1) Hudson, (2) Macá, (3) Cay, (4) Mentolat, (5) Melimoyu and (6) Yanteles)

2.2 Geology

Lago Cástor is located northeast of the Chile Triple Junction, a point at which the South American Plate, the Nazca Plate, and the Antarctic Plate converge. It is situated in the back-arc domain of the 1100 km long Liquiñe-Ofqui Fault Zone (LOFZ), a strike-slip fault system which is part of the larger Southern Volcanic Zone (SVZ; Parada et al. 2001). Isochronous to the activation of the LOFZ, the subduction-related uplift of the Andes was initiated in the Miocene (23.03 to 5.33 Ma BP) (Pankhurst & Hervé 2007). Typically, the materials originating from volcanic activity in the SVZ are linked to subduction processes (Gutiérrez et al. 2005). The subduction zone along the western edge of the South American Plate is accompanied by a volcanic arc, of which several central volcanoes have largely influenced the geology and soils of the Aysén basin (see 1.2.1; e.g. Stern et al. 2007). Today, the study site is characterised by exposed geologic features of Lower to Upper Cretaceous volcanic rocks and patches of Holocene sedimentary deposits (Servicio Nacional de Geologia y Mineria 2004). Figure 2.3 shows the Lago Cástor catchment with the distribution of its corresponding geologic units.

Published records on the seismic history of the study area are hardly available. According to the CERESIS database record (Giesecke et al. 2009), the study site experienced some minor earthquakes during the last centuries, none of them exceeding magnitude 5.0 on the Richter scale. With regard to the fact that the sediment column lacks any obvious seismic horizons (cf. 4.2), it is most likely that these earthquakes do not have a signature in the sediments of Lago Cástor.

2.3 Glaciology, Geomorphology, and Soils

As many as 40 glaciations occurred in Patagonia from the Late Cenozoic till the Last Glacial Maximum (LGM; Thomson 2002). The maximum ice extent at the LGM is shown in Figure 2.4. The intense carving activities of the corresponding Patagonian glaciers were the main contributors to intense denudation processes that ultimately lead to incision rates exceeding the amplitude of any isostatic rebound (ibid.). Nowadays, these processes find their expression in numerous

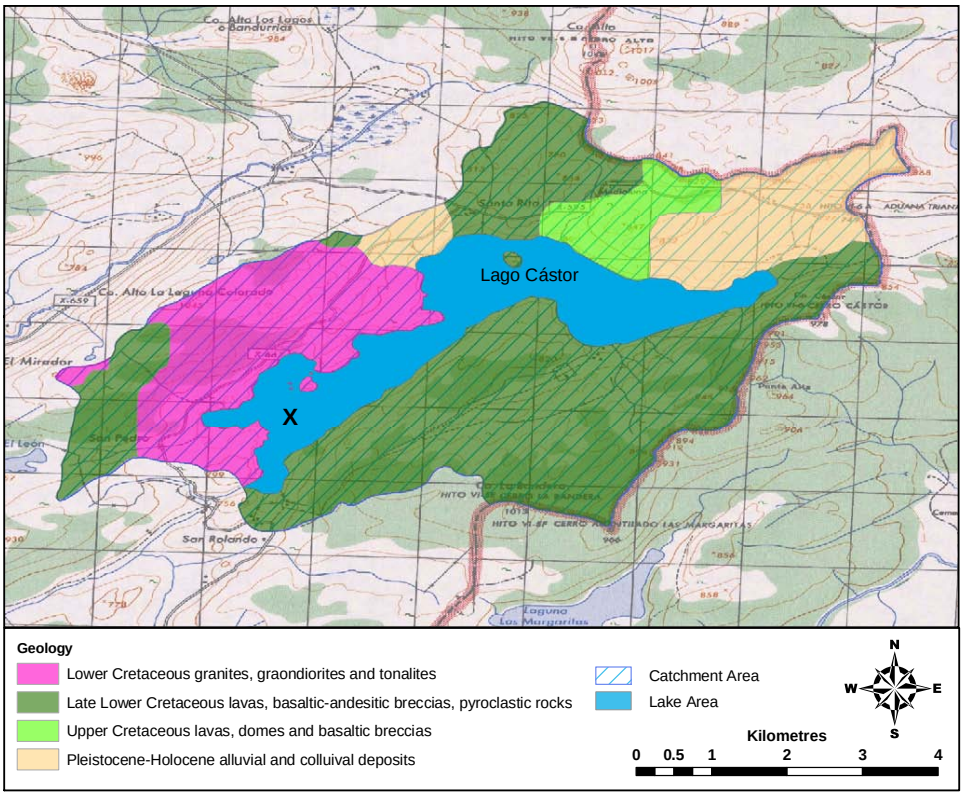

Figure 2.3: Map of Lago Cástor and its geologic units (geologic data from Servicio Nacional de Geologia y Mineria 2004).

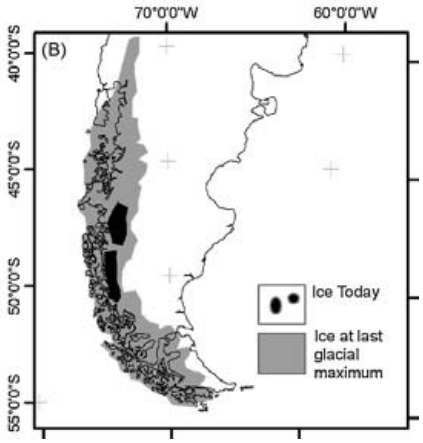

Figure 2.4: Maximum extension of continental ice during the LGM at about 18,000 cal. yr BP. Figure adapted from Armesto et al. 2010.

large glacial lakes in the mainland and in deeply incised fjords at the Pacific coast (ibid.). Besides the glacial activities, Montgomery et al. 2001 suggested that large scale climate patterns were a primary driver of South Andean topography (see section 2.4). This shows its expression in the anomalous drainage systems at that latitude (cf. section 2.5).

The last time the study site was completely glaciated dates back to the LGM at the Pleistocene-Holocene transition (e.g. Markgraf et al. 2007). Since then, numerous glacier fluctuations have occurred until the final neoglacial advance during the LIA, which is bracketed in time by the years AD 1600 to AD 1900 (Glasser et al. 2004). Since that time and until recently, the rate of average glacier mass loss has accelerated, but bedrock response at the latitude of Lago Cástor has remained only marginal (Masiokas et al. 2009, Ivins & James 2004). Today, the most striking glacial features in the wider study area are the North and South Patagonian Icefields south of latitude 45°S, besides numerous smaller glaciers in the region (Clapperton 1994).

Due to the Pleistocene glaciation, only young soils can have developed in the study area. After deglaciation, the older sediments were partially eroded, transported northeastwards to Northeastern Patagonia and settled as loess or loessoid deposits (Iriondo 1997). According to the SOTERLAC 1:5 million Soil and Terrain Database and as expected from the small size and rather homogeneous geology of the catchment, humic umbrisol is the only soil type in the catchment area (Dijkshoorn et al. 2005). It is likely that this soil type developed in accordance to the Andosols further north of the study site, which evolved during successive volcanic eruptions throughout the Late Glacial and Holocene (Bertrand et al. 2008a). The dominant grain size of the soils in the catchment was determined as loamy sand to loamy silt (Peralta et al. 1979). As a consequence of the uniformity of the soil, the soil type in the catchment of Lago Cástor is assumed to have no impact on the lake sediments. Yet, an influence of varying grain size and tephrogenic alterations is very likely existent.

2.4 Climate

Classifying south Chilean climate with the help of the revised Köppen-Geiger climate classification is not straightforward. According to this classification, the study site is located within the zone Cfc, but is very close to fragmented zones of Csc, Csb, and ET (see table 2.1, Kottek et al. 2006). Peel et al. 2007 reduces the complexity for this region, and clearly classifies the study area as Cfc. The issues with the classification are caused by the complex geomorphology of southern Chile and climatic implications therefrom. Both temperature and precipitation patterns show a high spatial variability. The mean annual temperature of North Patagonia is dominantly influenced by latitude, elevation and proximity to the ocean (Boninsegna et al. 2009). The mean monthly temperature and precipitation at a nearby climate station in Coyhaique is shown in Figure 2.5. As the elevation of the study site is slightly higher (725 m a.s.l.), its temperatures are probably lower than shown than the ones shown in the diagram. In contrast, the distribution of precipitation is presumably similar to the one shown in Figure 2.5, as suggested by the isohyets shown in Figure 2.6. Also shown in this Figure are the locations of weather stations in the Aysén basin. The records of two of those stations are discussed in section 3.12.

Table 2.1: Climate zones at or near the study site according to the revised Köppen-Geiger climate classification (Kottek et al. 2006)

Code	Climate Zone	Precipitation	Temperature
Cfc	Warm temperate	Fully humid	Cool summer and cold winter
Csc	Warm temperate	Dry summer	Cool summer and cold winter
Csb	Warm temperate	Dry summer	Warm summer
ET	Tundra climate		

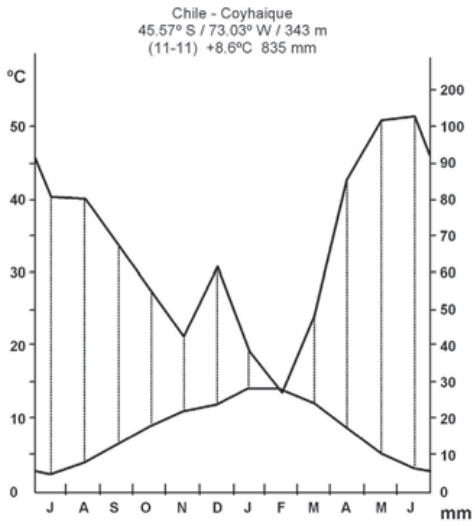

Figure 2.5: Climate diagram of Coyhaique. Station location and mean annual temperature and rainfall are shown in the Figure description (Quintanilla 2008).

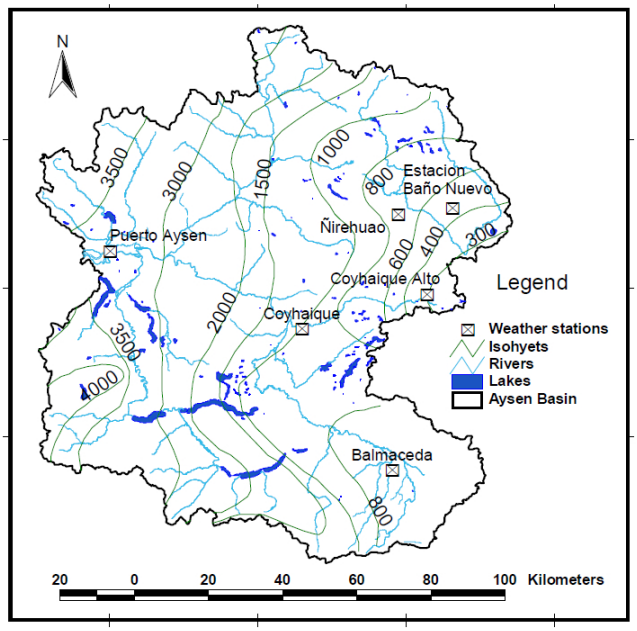

Figure 2.6: Weather stations and isohyets (mm/yr) in the Aysén basin (Departmento de Hidráulica e Ambiente, - 2006). A very noticeable feature is the strong precipitation gradient along the main Andes mountain chain.

Precipitation along a profile parallel to the latitude of the study site shows an increase from ca. 1500 mm p.a. at the Chilean coast over 3500 mm p.a. at the main Andean divide to only ca. 300 mm p.a. in the xeric Patagonian steppe (Boninsegna et al. 2009). These numbers are underlined by the significant drop in monthly rainfall values between Aysén near the Pacific coast and Balmaceda at longitude of the study site (Aravena & Luckman 2009). This pattern is very apparent under consideration of the prevailing Westerlies south of 40°S (Garreaud et al. 2009). The impact of the westerly storm tracks is amplified due to their annual average position just a few degrees south of the study site (Garreaud & Falvey 2009). The interannual latitudinal shift of the jet stream depends primarily on the location and strength of the Southeast Pacific anticyclone in the north and the circum-Antarctic low pressure belt in the south (Gilli et al. 2005). As a consequence of that, the area affected by midlatitude precipitation permanently shifts between a maximum extent of 30°S in austral winter and a minimum extent of 40°S in austral summer (Garreaud et al. 2009). This partly correlates with the average seasonal discharge of North Patagonian rivers, which is generally highest from June till December (Compagnucci & Araneo 2007). Precipitation patterns are shown in combination with average pressure fields and the corresponding wind vectors in Figure 2.7. The pressure fields shown in this map tend to be very stable over the course of a calendar year (Garreaud & Aceituno 2007).

Most of the variance in South American climate can be explained by a few supraregional to hemispherical modes (Quadrelli & Wallace 2004). Modes like the El Niño-Southern Oscillation (ENSO), the Pacific Decadal Oscillation (PDO), or the Southern Annular Mode (SAM) are known to influence modern Chilean climate over interannual to interdecadal timescales (Gillett et al. 2006, Moy et al. 2009). Precipitation in regions south of 40°S is strongly influenced by high-latitude Antarctic circulation patterns best expressed by the SAM index (Thompson & Solomon 2002), whereas only a weak negative correlation exists for the dependency on ENSO (Aravena & Luckman 2009). The SAM also correlates with sea level pressure (SLP) fields and temperature (Gillett et al. 2006). No correlation was detected between precipitation patterns and the PDO or the Antarctic Oscillation (AAO), but significant correlation was found between precipitation and the Antarctic Pacific Oscillation (AAPO) index (Aravena & Luckman 2009). A choice of indices is used in this study and presented in section 3.12.

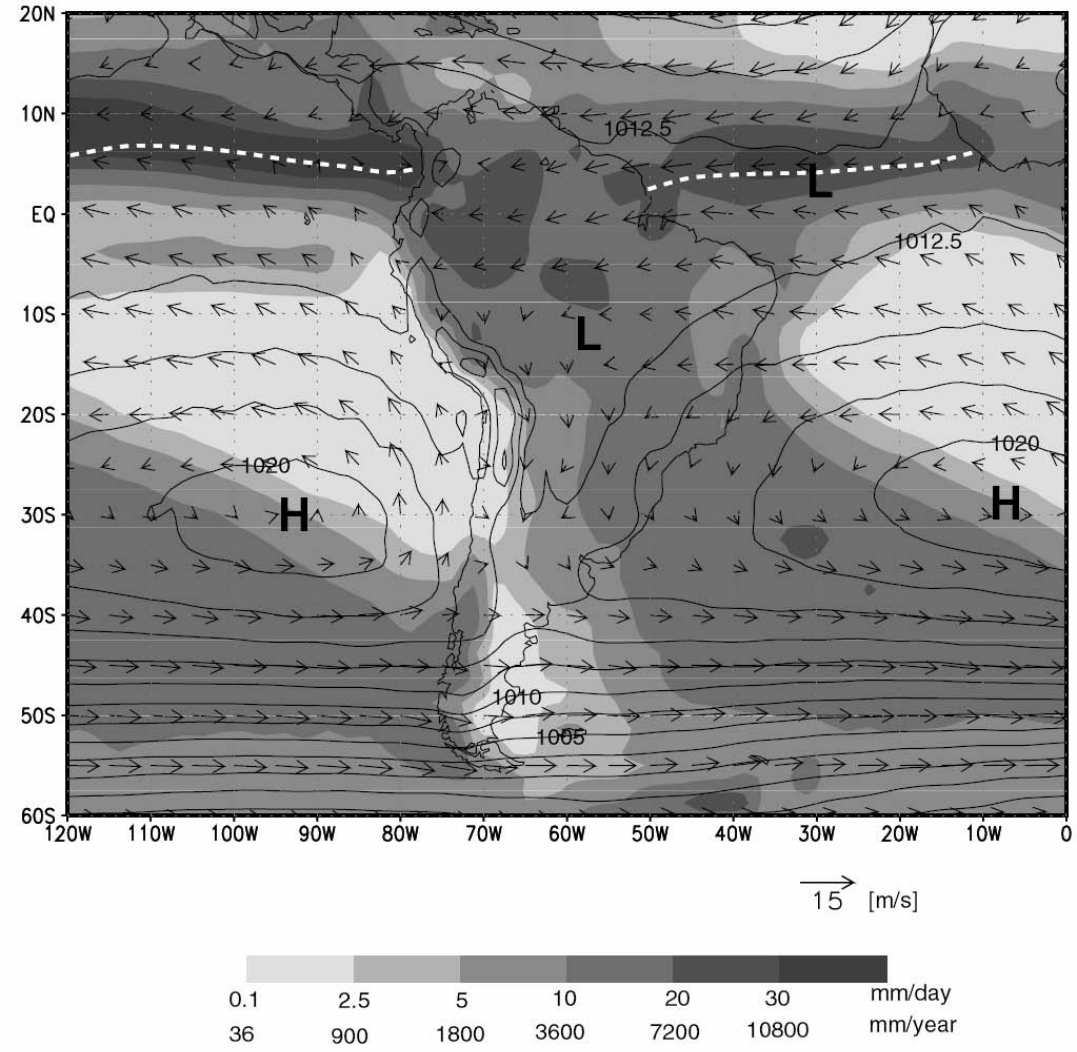

Figure 2.7: Annual mean rainfall (shading scale at bottom), sea level pressure (contoured every 2.5 hPa), and low-level winds (arrow scale at bottom). The dashed white line indicates the mean position of the ITCZ. Letters H and L indicate the approximate centre of the subtropical anticyclones and continental lows, respectively (Garreaud & Aceituno 2007).

2.5 Hydrology and Lake Classification

As mentioned in section 2.3, Lago Cástor was formed by glacial processes during the last glaciation. Since at least the onset of the Holocene, tributaries east of the main Andean watershed divide (represented by the eastern border of the Lago Cástor catchment) drain into the Atlantic Ocean, while tributaries west of the divide (including the Lago Cástor catchment) drain westwards into the Pacific Ocean (see map 2.6). Water from the Lago Cástor catchment runs through the rivers Rio Pollux, Rio Simpson, and Rio Aysén into the Aysén Fjord. It has numerous small inflow streams, but no standing waters upstream. With a ratio of about 17.4 %, the area of the lake relative to the size of its catchment is rather large.

In agreement to the mostly similar element concentrations at 2 m (representing the epilimnion) and 18 m water depth (representing the hypolimnion; data shown in table 4.1, page 53), the lake water undergoes vertical mixing in both transition seasons. This is in accordance with the temperate climate regime dominating the region (section 2.4). As phosphate concentrations were far below 10 $mg\,l^{-1}$, the lake clearly shows oligotrophic characteristics. The epilimnion is almost depleted of nitrate when compared to the hypolimnion, suggesting high bioactivity in the topmost meters of the lake during austral summer (cf. table 4.1). To sum up its general characteristics, Lago Cástor can be classified as glacigenous, exorheic, dimictic and oligotrophic lake.

3. Methods

This chapter briefly describes the methods that have been applied in dating, data collection, and analysis. For each method except the core pretreatment and description, a reproducible report on the laboratory procedures is preceded by a brief explanation of the method's fundamentals, its benefits for paleoenvironmental research, and its intended purpose within this Thesis. The geochemical methods were carried out in laboratories at the University of Bern or at external institutes. After the methodological descriptions, section 3.12 describes the climate parameters used in this study. This chapter closes with a section on the statistical approach and data treatment applied to analyse the series of measurements.

Before going into detail, a quick overview of the applied methods is given. Figure 3.1 provides this overview by showing the core sections and the resolution each of the methods has been applied at.

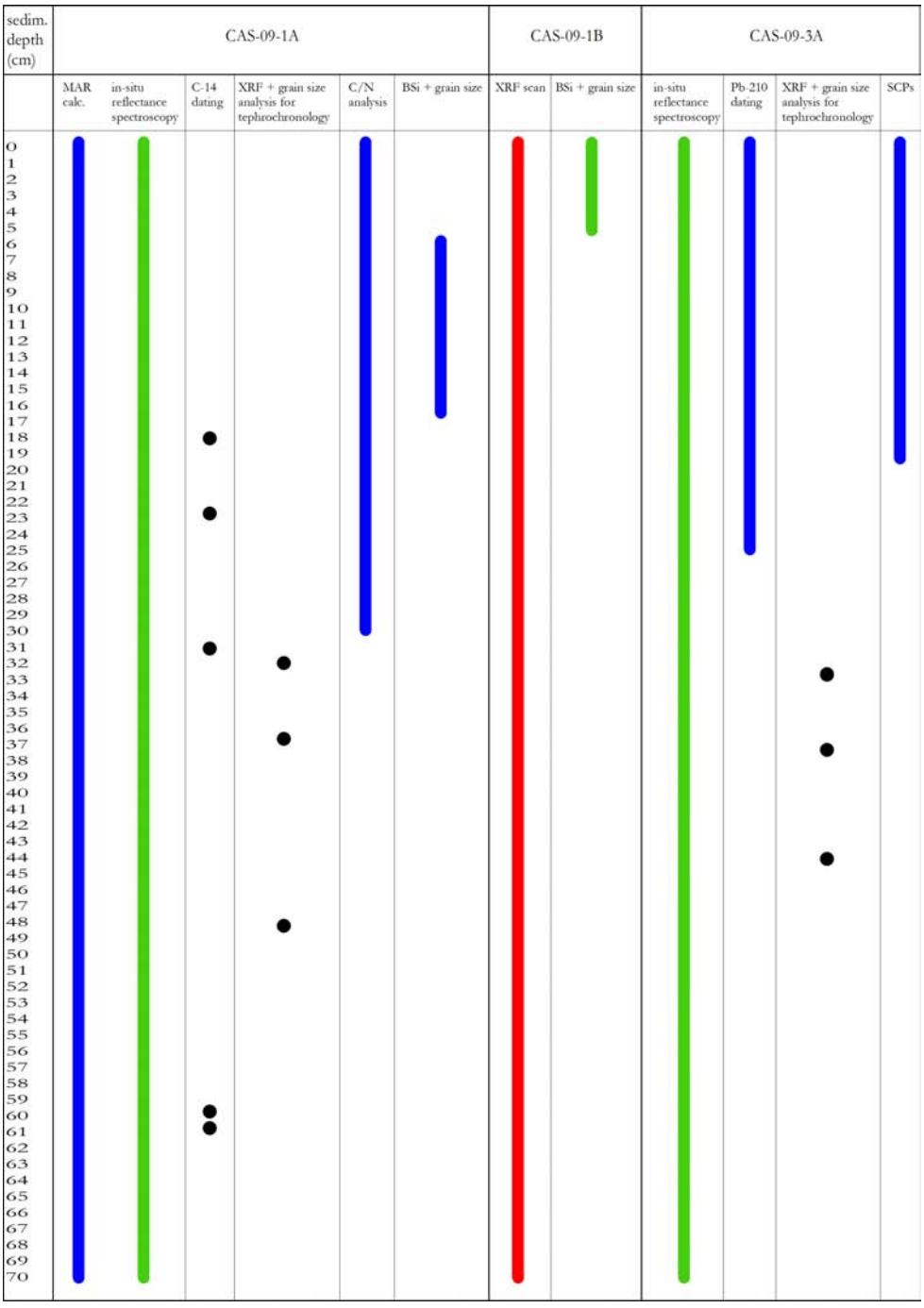

Figure 3.1: Overview of all destructive and nondestructive laboratory measurements with their corresponding core segments. Colours indicate the downcore sampling or scanning resolution of each corresponding method: 0.5 cm – blue, 0.2 cm – green, 0.05 cm – red, varying resolution of around 0.5 cm – black. Note that not all samples for lead-210 dating were used to construct the age-depth model (cf. Table A.2).

3.1 Coring and Sediment Pretreatment

A number of sediment cores were drilled on the field campaign lasting from January till February 2009. A team of scientists from both the University of Concepción and Bern carried out the field campaign. An Uwitec piston corer and an inflatable boat were used for drilling the sediment cores. Three cores were taken at roughly the same location in the southwestern sector of Lago Cástor, which belongs to the sediment accumulation zone of the lake. The precise location was determined by a portable GPS receiver. Table 3.1 summarizes the data relevant for the coring. Two out of three cores from Lago Cástor were sent to Bern, whereas the third core was brought to the University of Concepción for comparative analysis. The cores were put into metal boxes and shipped by air freight. The unopened cores were then immediately put into the storage room at a temperature of 5°C to prevent water loss and degradation. From transport until the end of analysis, they remained in a horizontal position to prevent sediment redeposition or compression within the core.

Table 3.1: Overview chart of the coring.

	CAS-09-1	CAS-09-3
Date of coring	2009-01-19	2009-01-19
Core length	74 cm	50 cm
Lake depth at coring location	21.5 m	21.6 m
Latitude	$S45° 36' 588''$	$S45° 36' 589''$
Longitude	$W71° 47' 964''$	$W71° 47'964''$

In early June 2009, both cores were opened with a specially designed core cutting device. By that, two equal-volume half-cores were obtained per core tube and labelled with the code "CAS-09-1A/B" and "CAS-09-3A/B", respectively. The cut face of each half core was carefully cleaned of loose sediment with a palette-knife, moving it precisely perpendicular to the main core axis. After each usage, the cores were sealed with tubular plastic film and a suction apparatus and then returned to the cold storage room.

3.2 Sediment Description

After opening and cleaning, the fresh core was photographed with a digital reflex camera in order to get a reference picture of the fresh sediment core. To scan the full core at the same resolution, the camera was mounted to a device that keeps it in equal distance to the sediment surface. The core and a scale were then moved stepwise from 0 cm down to the lower end of the core. Pictures were taken in standard mode without flash light, using a remote control to activate the release. In addition, two high-quality RGB (red-green-blue) and CIE_l*a*b* (lab colour space) pictures of CAS-09-1B were taken with a Jai CV L105 3 CCD colour line scan camera while measuring the element composition with the AVAATECH X-ray Fluorescence Core Scanner at the Institute of Geology at ETH Zürich (see section 3.7.2). Besides the image itself, a series of RGB and LAB values were measured at a downcore resolution of 70 μm.

The next step was to visually analyse the core in great detail and to note down any peculiarities. The self-made core pictures were combined to a single picture with the help of the panorama maker plug-in in Adobe Photoshop®. The picture from the line scan camera was imported into Adobe Illustrator®. Among other purposes, this picture was used for examining core segments of equal visual properties, with the primary aim to detect and delimit potential tephra layers (see section 3.5.1).

3.3 Water Content and Mass Accumulation Rate

Water content in lake sediment cores is controlled by sediment properties such as grain size distribution and clay content (e.g. Niwa et al. 2010). The mass accumulation rate (MAR) obviously depends on the amount of sediment input per unit of time. This parameter is essential to calculate various fluxes to the sediment column, as it combines the mass parameters with a time component for a given depth. The cumulative dry mass (CDM) is closely related to the MAR.

According to its general characteristics, water content within sediments can be used as an indicator for grain size and packing density. The MAR depends on sedimentation speed, packing density of grains, or the weight of the deposits, facilitating the determination of lithogenic facies within the sediment. Both MAR and CDM were used for calculation of the sediment age in the ^{210}Pb age model presented in section 3.5.3, and for calculation of fluxes (e.g. biogenic silica) to the sediment column.

Water content [%] was calculated for the 5 mm samples of CAS-09-1A by substracting the weight of previously freeze-dried samples from the weight of the wet samples and transforming the results to proportional values. It was ensured that the wet sediment was only exposed to air for a short time to minimize loss of water by evaporation. The annual mass accumulation rate (MAR_k $[g\,cm^{-2}\,yr^{-1}]$) for a sample k was calculated by applying Equation 3.1 for the dry weight (dw_k $[g]$) at downcore resolution i $[cm]$, assuming that the cut face of the half core has the shape of a regular semi circle with the measured radius $r = 2.97\,cm$. Similarly, the cumulative dry mass (CDM $[g\,cm^{-2}]$) of a sample k was calculated by summing up the mass accumulation of all samples j that have been deposited at a time earlier than the time of deposition of sample k, while disregarding the temporal component (Equation 3.2).

$$\mathrm{MAR}_k = \frac{\mathrm{dw}_k}{(\pi \cdot r^2 \cdot i_k)/2 \cdot a} \tag{3.1}$$

$$\mathrm{CDM}_k = \sum_{j=1}^{k} \frac{\mathrm{dw}_j}{(\pi \cdot r^2 \cdot i_j)/2} \tag{3.2}$$

The records had to be corrected for the lack (or reduced amount) of sediment at depth where the core has previously been sampled for carbon-14 dating and tephrochronology (see Figure 3.1). Sampling the half core CAS-09-1B instead of CAS-09-1A was not a solution to this problem, as this half core was intended to be used for future geochemical analyses. The only practicable workaround was to linearly interpolate the MAR at depth of the affected samples. This procedure introduces an error far smaller than calculating the MAR from the reduced sample mass.

3.4 General Sediment Preparation

For the measurement of grain size, biogenic silica (BSi), and counting spheroidal carbonaceous particles (SCPs), the freeze-dried sediment was dissolved of organic matter (OM). This was achieved by repeatedly adding 32 % hydrogen peroxide (H_2O_2), heating the solute to about 80 °C in a water bath, and letting the samples settle for at least one night. After the reaction had completely stopped, the samples were washed by repeatedly adding distilled water, centrifuging, and decanting the supernatant, until they were completely cleaned of H_2O_2. For the grain size and BSi preparation, the tubes were coverd with perforated Parafilm® M, and stored in a freezer. Once completely frozen, the sediment was freeze-dried and stored in a dry place.

While sampling the cores CAS-09-1 and CAS-09-3 for application of the destructive geochemical and dating methods (cf. Figure 4.1), a selection of four samples from variable depth and different facies was tested for presence of carbonates. This information is particularly relevant for interpreting radiocarbon data (Appleby 2001). A few ml of hydrogen chloride (HCl) were added to the dry samples. No calcium carbonate was present as no reaction occurred.

3.5 Sediment Dating

3.5.1 Stratigraphic Markers

Chronostratigraphic markers that are applicable for dating are (ideally thin) sediment core segments of known age. Even if the precise age of a marker horizon is unknown, a characterization of the corresponding sedimentary layers can aid locating similar strata between different sediment cores, provided a certain degree of similarity is detected (e.g. Turney & Lowe 2001). In the case of pre-existing time information, these relationships can help supply un-dated cores with a preliminary estimation of an age-depth relation.

In this study, three distinct types of stratigraphic markers were applied. Each of the following subsections describes a distinct type of stratigraphic marker.

3.5.1.1 Caesium-137

In Southern South America, a peak in the caesium-137 concentration was caused by the testing of nuclear weapons during the Cold War (Longmore et al. 1983). Over time, the bomb-produced Cs-137 was deposited into terrestrial and aquatic sediments, while this process was being amplified by precipitation (ibid.). In Southern South America, it reached its peak in between AD 1963 and AD 1965 (ibid.).

Dating of artificial radionuclides such as ^{137}Cs is the most widely used independent dating technique (Appleby 2001). In the Southern Hemisphere, it was widely used in paleoenvironmental studies for constraining lead-210 dated sediments (e.g. Urrutia et al. 2007, Abbott & Wolfe 2003, Barra et al. 2004). In a recent paper examining lead-210 age models from a Chilean site at latitude 34° S, the peak was dated to AD 1964 (von Gunten et al. 2009a). Consequently, this date was used to constrain the lead-210 model used in the present study.

Finding the ^{137}Cs peak is a straightforward process, if the peak has a distinct shape. In the case of a relatively broad peak or multiple peaks of similar extent, the constraint may be tested with multiple models, for example by holding the age (AD 1964) constant and moving this age along the depth of the potential occurrence of the "true" peak. When simultaneously adapting the ^{210}Pb ages above and below the assumed peak, the ^{210}Pb-based age model can be assessed in terms of the shape of the resulting age-depth relationship. For dates older than AD 1964, this very same age is then treated as if it was on top of the sediment core. Still under the assumption that the caesium peak is indistinct, it is then assumed to be located at a depth for which the resulting age-depth curve is smoothest. The actual approach used in this study with regard to the data is presented in the discussion of the age model in section 3.5.3.

3.5.1.2 Tephrochronology

The use of tephra deposits for dating, namely tephrochronology, is based on the fact that tephra deposits from volcanic eruptions settle on the land surface or lake beds at a distinct point in time. Provided that each tephra layer can be unambiguously determined and the age of the eruption is known, a tephra layer

can be used as a reference date in several archives, even if its age has not been determined separately.

Tephrochronology is widely applied in the literature. It is praised as a highly valuable tool for dating sedimentary sequences in both terrestrial and aquatic environments (Turney & Lowe 2001, Thorarinsson 1949). Tephra deposits can either be used as marker horizons of known age, or to constrain dated sediments in proximity to those layers (e.g. Stern 2007). However, the use of tephrochronology is limited spatially by the distribution of the tephra deposits through variability of atmospheric currents. Depending on the density of both the tephra and the lake sediment, it is also possible that a tephra layer is deposited twice or fine-grained tephra separates from its coarse grained matrix, leading to a misinterpretation of the lower layer as a primary deposit (Beierle et al. 2002). Hence, the correct stratigraphic position of a tephra deposit can not be determined with as much certainty as its composition (ibid.).

Tephrochronology was applied to cross-date the two sediment cores CAS-09-1 and CAS-09-3 and to search for matching tephra deposits of known age in the literature to extend or improve the age model. This approach was feasible, as the lake is located within an area affected by mid- to late Holocene volcanic eruptions from various volcanoes of the SVZ (see section 1.2.1). As the geochemical analysis revealed (cf. section 3.7.2), some of the sedimentary layers indeed had properties that classify them as tephra deposits.

In order to match the deposits to a known eruption, the element composition of each tephra sample was compared to a list of previously published reference compositions (cf. section 1.2.1). Following Markgraf et al. 2003, the concentrations of the elements Rb, Sr, Zr and Y from chosen tephra samples were summed to 100 % and compared with the published composition. On the basis of Gutiérrez et al. 2005, a number of characteristic element ratios were computed for the purpose of tephra identification. Here, the comparison was achieved by plotting the elements and by visually checking which of the marked clusters (and hence to which volcanic center) the tephra material can be attributed to. This was facilitated by overlaying the data points with the corresponding plots from Gutiérrez et al. 2005.

3.5.1.3 Spheroidal Carbonaceous Particles

SCPs are produced from industrial burning of fossil fuels (both coal and oil), and have no natural sources (Rose 2001). They are part of the products of the combustion process that was not burned and consequently consist of mainly elemental carbon (ibid.). The typical characteristics for both coal and oil produced SCPs is their black colour, near-spherical shape and richness in contours, while SCPs generated by oil combustion are generally more porous (ibid.)

Besides being an indicator for anthropogenic pollution by high temperature fossil fuel combustion, there are two ways of applying SCPs as stratigraphic markers (e.g. Wik & Renberg 1996). The time of initial concentration of SCPs in lake sediment profiles mirrors the onset of local-to-regional industrial and urban history (Rose 2001). But this relation can also be inverted to gain a dated reference depth within the core profile, provided the onset of regional industrial activity is precisely known and that strong bioturbation and turbidites above the dated sediment layer can be ruled out. In South America, this relation has only been applied by a few studies (e.g. von Gunten et al. 2009c). Equivalently, additional age information can be attained by distinct peaks in SCP concentrations of known age (Rose 2001). Peaks are common and well known for the European continent, where they largely coincide with the time of the industrial revolution (Rose 2001). In contrast, SCP peaks in the wider study area are unknown or not published. In this study, the initial concentration of SCPs counts was applied with the purpose of verifying the lead-210 age model.

SCPs were counted in accordance with Renberg & Wik 1985. As a primary step, roughly 50 mg of dry sediment was sampled from CAS-09-3A and dissolved of OM (cf. 3.4). Then, 20 ml of 10 % hydrochloric acid (HCl) were added in order to reduce iron oxides. After that, the solute was cleaned by repeatedly filling up the beaker with distilled water, letting it rest for one night and decanting it to 40 ml. For each sample, the weight of one 200 ml conical flask was determined first without and then with the solute. For each sample, one clean petri dish was put under the fume cupboard and partly filled up with a homogeneous and representative aliquot of the solute. After drying, the petri dishes and a sheet of gridded paper as counting aid were put under a Leica® light microscope, using variable magnification factors. For identification of SCPs, the particles were assumed to

have the standard characteristics (see above), while a differentiation between coal and oil produced SCPs was not feasible due to the technical limitations of the light microscope. A selection of petri dishes was counted repeatedly by other lab personnel to minimise erroneous SCP identification.

3.5.2 Carbon-14 Dating

Oxidised cosmogenically produced ^{14}C is constantly taken up by organic tissue of terrestrial and aquatic organisms, keeping it in isotopic equilibrium to its life medium (Björck & Wohlfarth 2001). Once the organism dies, the decay of the isotope is initiated (ibid.). The radioactive element decays with a half life of 5568 years, until the measurement errors become too large for a reasonable age determination at about 40,000 yr BP (ibid.). Radiocarbon dating is also affected by slight variations in the amount of cosmogenically produced ^{14}C in the atmosphere due to additional production of old CO_2 from terrestrial sources, and additional production of ^{14}C by nuclear weapon tests, among others (ibid.). As the sum of all errors is too high for the last few hundred years, the method must be complemented for this time period by the use of ^{210}Pb and ^{137}Cs (see sections above and below). In order to compensate for the errors that occur throughout the time span used for radiocarbon dating, the ^{14}C ages have to be calibrated. For the Southern Hemisphere, SHCal04 is the standard calibration curve (McCormac et al. 2004).

In addition to the uncertainties given above, substantial deviations between a radiocarbon age and its corresponding true age may arise from reservoir effects that are present in the catchment (Björck & Wohlfarth 2001). This effect is due to sources of old carbon like caused by, for example, presence of carbonate bedrock, groundwater enriched in old CO_2, or infiltration of carbon from older glacial deposits (Björck & Wohlfarth 2001). To test whether this effect plays a role in lake sediments, it is common to sample terrestrial macrofossils and bulk sediment from the same depth (Geyh et al. 1999). In case the standard deviations of both ages overlap, a reservoir effect can most likely be ruled out (ibid.). Apart from this effect, major errors in the carbon-14 dated sediment sequences may also arise from lake sediment redeposition (Björck & Wohlfarth 2001). In most cases, both sources of error can be either avoided or eliminated.

Today, radiocarbon dating is widely used in paleoclimatological and paleoenvironmental studies worldwide, among numerous studies from different fields of research (Björck & Wohlfarth 2001). In Southern South America, this dating technique was applied in numerous studies published within the last years (e.g. Bennett et al. 2000, von Gunten et al. 2009b, Haberzettl et al. 2005). For this study, it was of fundamental importance to build an age model spanning the whole length of the core in order to be able to relate each of the geochemical proxies at a given depth to an age. As no varved sequences exist, these objectives could only be met by radionuclide dating.

The half core CAS-09-1A was carefully analysed in order to determine the most suitable locations at which to sample the core. The criterion was to cover the full time span contained within the core, while not taking samples from sediment that was deposited after AD 1900 and not taking samples containing volcanogenic material. Sampling was done at a resolution of 0.5 cm downcore, omitting the sediment close to the tube boundaries to avoid additional uncertainties that may arise from carbon contained within the plastic casing of the core tube. Each sample was weighed, freeze-dried and put into a plastic box. In a first attempt, three samples were sent to the Poznan Radiocarbon Laboratory. Although carbonate bedrock is most likely absent in the catchment (see section 2.2), the other potential causes for a radiocarbon reservoir effect were tested by twofold sampling from the same depth. Sample CAS-09-1A-bulk (60.5 cm) contained bulk sediment and sample CAS-09-1A-macro (60.5 cm) contained terrestrial plant macrofossils (cf. Table 4.2 in the appendix). Based on initial results, two additional samples (CAS-09-1A-bulk (18 cm) and CAS-09-1A-bulk (23.35 cm)) from the upper core segment were sent to the same laboratory. Each sample was dated by accelerator mass spectrometry (AMS).

Once the raw dating results were sent back to the laboratory at the University of Bern, the calibrated carbon-14 ages were determined to compensate for most of the deviations in the radiocarbon input to the sediments from a constant supply (see introductory paragraph). The Oxford radiocarbon calibration program, OxCal, was used to build an unconfined model with the aim to calibrate each raw radiocarbon age (Ramsey 2001). The model is discussed in 5.2.1.

3.5.3 Lead-210 Dating

The lead-210 dating method is based on the decay of naturally produced ^{210}Pb from terrestrial uranium-238 over a number of daughter isotopes to radium-226 (Appleby 2001). A fraction of the next daughter isotope of this radioactive series (radon-222) escapes into the air, decays over a couple of short-lived isotopes to lead-210, and is then removed from the atmosphere by precipitation or dry deposition (Hakanson 2001). Lead-210 falling directly into lakes settles to the lake bed with below-annual delay (Appleby 2001). Although a positive relation to precipitation was proven, the lead-210 flux is assumed to be constant over time, given the place is fixed (ibid.). Furthermore, the method requires that mixing of the lake sediment is negligible (ibid.).

In addition to lead-210 derived from the atmospheric flux (unsupported fraction), lead-210 is also produced in-situ from the parent radionuclide 226-Ra (supported fraction; Appleby 2001). The supported fraction is usually in equilibrium with its mother isotope, whereas the excess ^{210}Pb can be determined by simply subtracting it from the supported fraction (ibid.). As the unsupported fraction decays in accordance to the radioactive decay law (Equation 3.3), the deposition age can be calculated, provided the initial ^{210}Pb activity can be estimated for each sediment layer, and the unsupported fraction is not zero (ibid.). In Equation 3.3, C(0) denotes the unsupported activity at the lake sediment surface, $\lambda = 0.03114 yr^{-1}$ the ^{210}Pb decay constant, MAR the mass accumulation rate in $g \cdot cm^{-2} yr^{-1}$, F the mean annual rate of supply of fallout ^{210}Pb and CDM the cumulative dry mass is in units of $g \cdot cm^{-2}$, which depends on the total sediment depth.

$$C(\text{CDM}) = C(0) \cdot e^{\frac{-\lambda \cdot \text{CDM}}{\text{MAR}}}, \text{ with } C(0) = \frac{F}{\text{MAR}} \tag{3.3}$$

As two types of well-established numerical models were compared in this study, they shall be briefly outlined here. The constant initial concentration (CIC) model assumes a constant initial ^{210}Pb concentration of the sediment, disregarding accumulation rates (Appleby 2001). As a consequence, the supply of ^{210}Pb to the sediment varies in direct proportion to the sedimentation rate (ibid.). Hence, Equation 3.3 simplifies to Equation 3.4.

$$C(\text{CDM}) = C(0) \cdot e^{-\lambda \cdot t} \tag{3.4}$$

In contrast to the CIC model, the constant rate of supply (CRS) model assumes a constant rate of deposition of unsupported ^{210}Pb (ibid.). Furthermore, it assumes a quick sedimentation of fallout ^{210}Pb and excludes sediment redeposition (ibid.). Changes in the sedimentation rate through time lead to changes in the initial unsupported ^{210}Pb concentration (ibid.). The model is either unconstrained or constrained by peaks of e.g. ^{137}Cs. A detailed description of this model is given by Appleby & Oldfield 1978.

Lead-210 dating is inevitable in order to complement for the lack of reliable radiocarbon dates for the last 100 to 150 years (Björck & Wohlfarth 2001, von Gunten et al. 2009b). This method is irreplaceable in cases of non-varved or only partially varved lake sediment cores. It is used in a variety of research fields. In paleoenvironmental studies, it was widely applied to answer questions regarding environmental processes throughout the last 150 years, such as assessing deforestation versus afforestation or changes in lake water quality and characteristics associated with anthropogenic pollutants or eutrophication (Appleby 2001). As these were also the goals of this study, lead-210 dating is of fundamental need.

A total of 50 samples at 0.5 cm resolution were sampled from 0 cm to 25 cm. Due to a minor coordination error at the very start of the thesis, the core CAS-09-3 was sampled instead of core CAS-09-1, while the latter one was being used for the majority of the other analyses (see Figure 3.1). This error was detected only after the dating results were submitted to the laboratory in late December 2009. As the location of both coring sites only differed by a few meters, and bioturbation and sampling did most likely introduce an error of higher amplitude, the results were still used for the age-depth model. This was done by fitting the results (ages) of the final lead-210 based age model to the core CAS-09-1 by use of stratigraphic correlation (see next section 3.6). Note that the carbon-14 dated core segment of CAS-09-1A was not affected by this transformation.

The samples were processed at the department of surface waters at Eawag Aquatic Research, Dübendorf. Gamma-decay counts of ^{210}Pb (46.5 keV), ^{226}Ra (352 and 609 keV), and ^{137}Cs (662 keV) were collected for more than 20 hours using Canberra low background, well-type GeLi-detectors (measurements in accordance to von Gunten et al. 2009b). A total of 15 samples from the upper 10.75 cm were measured and returned to the lab. Later on, two additional samples from greater

depth were sent in (cf. Table A.2). The results comprised radium-226, K-40, and lead-210 activity, each with a corresponding 2σ error estimate. The numerical age models (CIC, unconstrained CRS, constrained CRS) were fed with this data except for K-40. The parametrization of the models is discussed in section 5.2.2.

3.6 Stratigraphic Correlation

Stratigraphic correlation is used to compare and match stratigraphic records (Thompson & Clark 1989). This can either be achieved by numerical methods, or by a manual approach (ibid.). The manual process seeks to locate and interlink the most dominant similar variance between two equal variables plotted over the depth of the corresponding core. The correspondence of the records is generally expressed in the form of distinct peaks or troughs that occur in both series. The manual approach was applied in this study, as the age-depth combination of the lead-210 model originating from CAS-09-3A had to be fitted to the depth of CAS-09-1A.

A suitable parameter was chosen which shows a high inter-core correlation. As the data from the in-situ reflectance spectroscopy was acquired from both cores, the fit of each of its ratios was analysed. The highest fit was found for the parameter $\frac{R_{700}}{R_{675}}$. In the next step, both data vectors were plotted on a single graph, and peaks or troughs of obvious similarity were linked. Then, the ages from CAS-09-3A were assigned to the corresponding depth of CAS-09-1A. The maximum error introduced by this method was estimated to $\pm 0.25\,\mathrm{cm}$. This error was accepted due to the assumption that the uncertainty introduced by sampling and bioturbation outweighs the error.

The stratigraphic correlation was extended by a tephra intercomparison of both cores CAS-09-1 and CAS-09-3. This comparison was based on the techniques as presented in detail in section 5.1.

3.7 X-Ray Fluorescence

3.7.1 XRF Core Scan

X-Ray Fluorescence (XRF) core scanning allows for rapid collection of high-resolution continuous downcore records of various chemical elements (Rothwell & Rack 2006). The method is based on the element-specific emittance of fluorescence energy and wavelength spectra (Weltje & Tjallingii 2008). Due to variability in sediment composition, texture, porosity, and water content, the measured element concentrations in units of counts per second (cps) have no quantitative representation (Rothwell & Rack 2006). Hence, the results are only presented in a qualitative way in the form of count rates (Richter et al. 2006). Cleaning and smoothing of the split core sediment surface is still necessary in order to maximize count quality (Zolitschka et al. 2002).

Elemental variations determined by XRF scanning techniques are used to infer changes of environmental conditions, like e.g. diagenetic processes and pollutant inputs, and can assist in sediment correlation and process studies (Rothwell & Rack 2006). The qualitative element concentrations can be used to calculate qualitative element ratios that potentially show a good correlation with environmental parameters (e.g. Koinig et al. 2003). Certain elements or element ratios may be utilized as proxies for environmental conditions that are either generally valid or constrained to specific conditions (ibid.; cf. Table 3.2).

CAS-09-1B was analysed at the department of Climate Geology at the ETH Zürich, using the AVAATECH X-Ray Fluorescence Core Scanner "LisbETH". In order to minimise count uncertainties, the surface of the half-core was cleaned and smoothed to an even surface, and then sealed with a thin plastic film. Light elements were measured at a tube voltage of 10 kV, intermediate elements at 30 kV, and heavy elements at 50 kV. Table A.1 in the appendix lists all elements acquired by the scan.

Table 3.2 shows a list of single elements and element ratios that act as proxies for various environmental conditions. Proxies marked with a "C" are limited to the specific environmental conditions present in the study of Koinig et al. 2003. These proxies were calculated, but interpreted with caution. Furthermore, the element

counts were tested for quality by assuming a minimum count rate of 150 cps below which the magnitude of white noise in the data series became dominant over the low-frequency variability.

Table 3.2: Proxies of elements and derived element ratios determined by XRF scanning. General validity of each proxy is indicated by letter "V". "C" indicates proxies that are limited to specific environmental conditions (Koinig et al. 2003).

Element	Proxy value or general statement	Validity	Reference
Mn/Fe	indicator for paleoredox conditions	V	Wersin et al. 1991
Fe	high iron content may cause analytical errors of the Mn, Ti, K and Ca counts	V	Koinig et al. 2003
Mn	degree of correlation between Mn and Fe or Mn and the silicate fraction primarily related to the redox potential	C	Koinig et al. 2003
Ca, Sr	level of physicochemical carbonate or silicate weathering, pH level or a combination of those	C	Koinig et al. 2003
Sr, Rb	supporting parameter for grain size data and mineralogy	C	Koinig et al. 2003
As, Zn	contaminants potentially caused by human activities	V	Koinig et al. 2003
Rb, Zr	elements of near-constant concentration with depth (highly resistant)	V	Koinig et al. 2003
Rb, Zr, K, Ti	indicators of physical weathering rates if silicates are abundant in the watershed	C	Koinig et al. 2003
Al/Fe, Ca/Fe, Al/Ti, Ca/Ti	indicators for pedogenic sediment input	C	Koinig et al. 2003
Br	indicator for organic matter concentration	C	Gerritse & George 1988
Ca/Al	supporting parameter for tephra identification	C	Vogt et al. 1987

3.7.2 XRF of Single Samples

In contrast to scanning XRF techniques, conventional XRF measurements are acquired from single samples. As for the XRF scan, the samples have to be dry and homogeneous and must have a flat and smooth surface (Rothwell & Rack 2006). In order to meet these preconditions, samples are either processed to glass or powder pills. The analysis of these pills reveals semiquantitative results of major elements and trace elements. The number of elements obtained from glass pills is higher than the number of elements obtained from powder pills. Semiquantitative measurements are mandatory for the identification of tephra deposits, as they provide information on the quantitative composition of the analysed mineral.

Semiquantitative or quantitative XRF analyses are widely applied in paleoenvironmental research to characterize or identify minerals from various geologic sources (e.g. Gutiérrez et al. 2005). One major application worldwide, and particularly in Southern South America, is the identification of tephra deposits (e.g. Stern et al. 2007, Orihashi et al. 2004). These studies also determine or present the approximate year of deposition of those tephra layers (ibid.). In order to make these results comparable to this study, the diagnosis of the XRF results followed the principles of the published studies (cf. section 3.5.1.2). This allowed for the characterization and / or identification of tephra deposits within both sediment cores.

Before sampling, the potential tephra layers of the half-cores CAS-09-1A and CAS-09-3A were identified with the help of a visual analysis of the core, by using the qualitative element concentrations from the XRF core scan, and by analysing the results of the in-situ reflectance spectroscopy. The criteria that were applied for the classification of a sediment facies as a tephra deposit were a purely black sediment colour and a rather coarse grain size (except for CAS-09-1A-T4 (67.5–69.4 cm), see section 4.2). Secondary classifiers were distinctive changes of the XRF scan element counts or ratios thereof, as well as distinctive alterations of the proxy records derived from in-situ reflectance spectroscopy over depth. Grain size was measured from non-crushed grains of the same sampling locations to improve the power of this classification. The laboratory steps were identical to those presented in section 3.11).

Once the potential tephra layers were chosen, the half-cores were sampled at the appropriate positions to gain approximately 2 g of homogeneous grains. The samples were freeze-dried and then crushed with a mortar to gain homogeneous silt-sized grains. Samples were put into a drying chamber at 60°C over night to ensure the complete loss of pore water. In parallel, porcelain bowls with a sufficient amount of $Li_2 B_4 O_7$ (Merck Spectromelt®) and lithium fluoride (LiF) were dried in a separate drying chamber at 110°C to ensure homogeneity and complete dryness particularly of the LiF which is hygroscopic. Inside of porcelain crucibles, the samples were put into a muffle furnace at 1050°C. After 1.5 hours, the samples were put into an exsiccator, weighed and immediately put back into the exsiccator to prevent absorption of moisture. From the weight difference, loss on ignition was calculated for each sample, which is required for measuring the elemental concentrations. Sample CAS-09-1A-T4-xrf-G (68.0–69.0 cm) was partially molten to an agglomerate, and could hence not be processed any further. For the remaining samples, the next steps were completed within two working days to prevent errors caused by absorption of moisture of the dried samples. For each sample, a mortar bowl was first filled with precisely 0.350 g of LiF, then 0.700 g of the sample was added, filled up with 6.650g of Spectromelt®, carefully mixed with a mortar and put into a sealed plastic box. To get an error estimate, a second set of glass pills was prepared equivalently to the first set. Table A.3 in the appendix lists the LOI and supplementary data relevant for the tephra samples obtained in the preparatory steps mentioned above.

The boxes containing the mixtures were taken to the Institute of Geology at University of Bern to found the pills. The mixture was filled into gold-platinum crucibles and put into a small smelting furnace. While the compounds were melting, the crucibles were slewn for a few times. Once the composite was completely molten, it was quickly poured into a pre-heated gold-platinum mould. After cooling, the pill was removed from the mould, labelled and put onto a tray for the transportation to the department of Geosciences at the University of Fribourg. The semi-quantitative measurements of the pills were carried out with the Uniquant® program.

The powder pill (sample CAS-09-1A-T4-xrf-P (67.5–69.4 cm)) was produced from additional material of the tephra layer that was used to create the pill CAS-09-1A-T4-xrf-G (68.0–69.0 cm). After drying the sample for two days at 50°C and crushing it to the silt fraction, a total of 0.9 g of Hoechstwax (APC solutions SA®) was added to 4 g of the sample material, mixed with a mortar, and finally pressed to a pill for 1-3 minutes under a pressure of 10-15 tons. The results were again analysed with the Uniquant software at the department of Geosciences, University of Fribourg.

3.8 Scanning In-situ Reflectance Spectroscopy

In-situ reflectance spectroscopy contributes to describing paleoenvironmental conditions (e.g. Wolfe et al. 2006). The GretagMacbeth Spectrolino® measures reflectance in a spectral range from 380 to 730 nm in steps of 10 nm (Rein & Sirocko 2002). The device allows to measure with a field of view of 2.5 mm and at a 2-mm downcore resolution (Schnyder 2007). The reflectance of specific wavelengths is used to calculate empirical proxies based on relative absorption band depths ($RABD_{x,y}$) and reflectance ratios (R_x/R_y) as calculated according to Rein & Sirocko 2002, Rein & Sirocko 2003 (erratum), and Wolfe et al. 2006.

The application of reflectance spectroscopy as an approach to assess paleoenvironmental conditions has recently shown growing research interest (e.g. Rein & Sirocko 2002, Das et al. 2005). A study by Trachsel et al. 2010 (in press) examines the use of various reflectance bands and ratios as proxies for quantitative high-resolution climate reconstructions. In the Southern Hemisphere, in-situ reflectance spectroscopy has only been applied by a small number studies. von Gunten et al. 2009c used the reflectance data as a proxy to measure total early diagenetic chloropigments (chlorins) in lake sediments from Laguna Aculeo, central Chile. As this means that proxies derived from in-situ reflectance spectroscopy are valid for South America, this nondestructive method was also applied in the Thesis.

The split cores CAS-09-1A and CAS-09-3A were mounted onto a rack to fix their position and determine the position of the Spectrolino device. Each core was covered with a thin plastic film and air bubbles were removed from below the film

with the help of a needle. The measurement sequences were initiated by repeated measurements of a white standard. Each half core was measured along a straight line near the middle of the core. The average of the white reference measurements was divided from each reflectance value. Three proxies were derived from the raw data.

The formula of the selected proxies are given by the proxy name in Table 3.3, except for the total chlorine proxy, which was calculated as $\text{RABD}_{660,670} = \frac{6 \cdot R_{590} + 7 \cdot R_{730}}{13} / R_{min(660,670)}$ (Rein & Sirocko 2003). The environmental conditions represented by each proxy are listed in column 2 of table 3.3.

Table 3.3: Proxies from in-situ reflectance spectroscopy used in this study.

Proxy name	Indicator for	Reference
$\text{RABD}_{660,670}$	total chlorine	Rein & Sirocko 2003 (erratum)
$\frac{R_{570}}{R_{630}}$	lithogenic content	Rein & Sirocko 2003 (erratum)
$\frac{R_{650}}{R_{675}}$	degree of diagenesis	Wolfe et al. 2006

3.9 Carbon/Nitrogen Ratio

In principle, biogenic matter is transported from its source (aquatic or terrestrial plants) to the lake sediment. Only a small fraction of the OM escapes the remineralization process and becomes buried in the sediments (Meyers 1994). Due to the absence of cellulose in algae, aquatic plants contain a much lower amount of atomic carbon compared to vascular (mostly terrestrial) plants (Meyers & Teranes 2001). Hence, under a constant nitrogen supply, the carbon-to-nitrogen (C/N) ratios of OM differ with respect to the origin of the OM (Meyers 1994). On average, the ratio is ≥ 20 for terrestrial plants, and between 4 and 10 for aglae (ibid.). However, the ratio may only be applied as a tracer of OM sources if the changes of C/N between living (sources) and decaying OM pools are small (Das et al. 2008). In addition, the ratio depends on the location of the coring site relative to its distance to the shore.

The C/N ratio is widely applied as an indicator for the sources of OM (Das et al. 2008). In particular, and based on the facts given above, the ratio is used to distinguish between aquatic and terrestrial sources of OM (Meyers 1994). For example, Das et al. 2008 applied the ratio as an indicator for tree cover and hence land use change, which was also aimed in this study. Positive peaks in the ratio may be representative of deforestation or intense cattle farming leading to increased erosion in the catchment (Meyers & Teranes 2001). However, the ratio can only be used for these environmental conditions, if the OM is quickly deposited into the lake (ibid.). This constraint implicates a link between the C/N ratio and variables amplifying the input of terrestrial carbon (e.g. heavy precipitation).

Apart from the ratio, the organic carbon flux can also be used as a proxy, as it mirrors changes in delivery rates of organic matter to lake sediments. The flux generally indicates changes in paleoproductivity, but the validity of this relationship may be hampered by post-burial diagenetic processes (Meyers & Teranes 2001). The nitrogen flux, on the other hand, is determined by aquatic productivity, which is primarily limited by the availability of organic carbon.

A total of 61 samples (5 mm resolution) from 0 to 30.5 cm from CAS-09-1A were analysed with the C/N analyser Vario MACRO CN (Elementar Analysensysteme GmbH). Roughly 40 to 70 mg of freeze-dried sediment was wrapped in special aluminium foil and compressed to a pill with the help of a cylindric hollow metal tube and a metal bar fitting precisely into the hole of the cylinder. Analogously, 6 standard pills of pure glutamic acid powder were assembled. The weight of each pill was noted down, excluding the wrapping. Before starting the measurement device, it was checked for gas leakage. After the warm-up phase, the measurement series was initiated with two blanks and two standard pills to ensure the proper calibration of the analyser. Sets of roughly 10 sample pills were put into the sample tray, each followed by one standard pill. A standard and a blank was measured at the end of the measurement series. After the successful measurements, the amount of carbon and nitrogen in ppm was multiplied with the MAR to gain fluxes of these elements to the sediment surface. Note that this calculation lead to a change in the flux unit to $ng\,cm^{-2}\,yr^{-1}$. The C/N ratio was calculated by the device software, dividing the relative amounts (percentages) of both elements.

3.10 Biogenic Silica Flux

Biogenic silica (BSi) concentration measures the amorphous Si content of sediments (Conley & Schelske 2001). The biogenic silica fraction of sediments represents the siliceous skeletal matter from the epilimnion, while subtracting silica that is dissolved while settling in the water column and on the lake floor (Cohen 2003). Owing to its simplicity and robustness, the wet chemical extraction method is most widely used in paleoenvironmental research (e.g. Conley 1998, Ohlendorf & Sturm 2008). Under the assumption that all aluminium originates from the dissolution of siliceous minerals in the samples, lithogenic silica (LSi) is taken into account by determining Al within the leachate and applying a suitable correction factor (Ohlendorf & Sturm 2008). It was shown that volcanic eruptions influence lake productivity by leading to an initial increase of the lake's silica content followed by an increase in diatom abundance (Barker et al. 2000, Urrutia et al. 2007). As the records of BSi in this study were obtained from a core segment well above the identified tephra horizons, this impact did not need to be considered.

BSi provides an index of diatom abundance and usually also of diatom productivity (Ragueneau et al. 1996). Based on these principles, BSi was successfully applied as a proxy for paleoclimatic and paleoenvironmental events that are caused by changes in temperature, precipitation, or a combination of both (e.g. Haug et al. 1999, Cortese et al. 2004, Swann 2009). The BSi analysis in this study precisely followed these aims.

The laboratory analysis was based on the wet chemical extraction method as described in Ohlendorf & Sturm 2008. A plastic bottle was filled with 863 ml deionised water (Milli-Q®) and 92.6 ml of 32 % NaOH to create 1 M NaOH. Each sediment-containing tube plus a set of empty tubes (blanks) was filled with 10 ml of this dilution, shaken and put into the ultrasonic bath to bring all the sediment into suspension. Samples were then put into the drying chamber for three hours at 90°C. After each hour, the samples were both shaken and put into into the ultrasonic bath. After that process, the tubes were centrifuged for 10 minutes at 7000 rpm, the supernatant now containing the dissolved silica. After Inductively Coupled Plasma Atomic Emission Spectroscopy (ICP-AES) measurements were

applied on the first set of 12 samples in a 1:10, 1:50, and a 1:100 dilution, the latter one yielded the results with the least errors and was chosen as the best solute for the remaining sets of samples. It was created by adding 12 ml of Milli-Q, 14 μl of nitric acid (HNO_3) and 140 μl of the sample solution into lockable tubes, and filling them up to a total of 14 ml with Milli-Q. The racks with the final tubes were then processed at the Paul Scherrer Institute (PSI), Villigen to measure total Si and Al by ICP-AES.

A mean Al:Si ratio of 1:3.5 as determined by a study from Lago Puyehue was used as the correction factor for the non-biogenic (mineral) silica fraction (Bertrand et al. 2008a). This was regarded as a reasonable factor for this study, as the sedimentation of Lago Puyehue is influenced by SVZ tephra deposits just as it applies to Lago Cástor (ibid.). The total amount of biogenic silica BSi_{cor} $[ppm]$ was obtained by multiplying the dilution factor $l = 100$ with the uncorrected BSi concentration BSi_{uncor} $[ppm]$, and by subtracting the product of the Al concentration $[ppm]$ and the non-BSi correction factor ($c = 3.5$; Equation 3.5).

$$BSi_{cor} = BSi_{uncor} \cdot l - (Al \cdot c) \tag{3.5}$$

The BSi flux was calculated by multiplying BSi_{cor} with the mass accumulation rate $[g\,cm^{-2}\,yr^{-1}]$ (cf. section 3.3). This calculation was applied in R.

3.11 Grain Size Analysis

Grain size distributions from lake sediment samples depend on numerous environmental processes (Beierle & Bond 2002). The distribution is influenced by the source material, the mechanisms responsible for the transport of the material, past physical and chemical conditions at the depositional site within the basin, and paleoclimatic and paleohydrological conditions within the surrounding watershed (Last 2001). There are multiple ways of determining grain size. The traditional method of sieving is nowadays mostly replaced by laser diffraction (ibid.). This technique is based on the absorption and refraction properties of the material and the medium (ibid.). There are numerous statistical parameters to summarize particle size distributions (ibid.).

A basic statistical analysis of the particle size distribution may reveal evidence of changing environmental conditions in the catchment (Folk 1964). The fields of application of this method can simply be derived by inverting the relation between cause and effect (last paragraph). In this study, grain size analysis was mainly applied to provide additional paleoenvironmental proxy parameters and to support the determination of the tephra layers of CAS-09-1 and CAS-09-3.

The granulometry analysis was carried out at the department of Climate Geology at ETH Zürich using the laser diffraction particle analyser Malvern Mastersizer 2000® from Malvern Instruments Ltd., which measures grains in diameters ranging from 0.02 μm to 2000 μm (Last 2001). As a result of the previous treatment of the samples with H_2O_2 and NaOH (see 3.4 and 3.10), the samples used to measure grain size were organic-free and BSi-free. The measurements were carried out in accordance with the instructions provided with the instrument. Samples were introduced into the medium (deionized water), brought into uniform suspension with a 2000 rpm stirrer, and crumbled with ultrasonic waves. Sample quantity was adjusted in order to obtain a laser beam obscuration between 10 % and 20 %. The results of all measurements were provided in an MS Excel® file and as a graphical report in pdf format. The PSD parameters mean, median, and skewness were chosen for analysis, as they were regarded to adequately reflect paleoenvironmental conditions (see section 4.10).

3.12 Climate Parameters

Reanalysis data of both temperature and precipitation was obtained from the KNMI climate explorer database (Van Oldenborgh et al. 2009) for the smallest available grid resolution of 2 x 2 degrees with the grid cell centred over the study site. It was given preference over station data, as no climate station is located in proximity to Lago Cástor and all available records from more distant stations only cover a shorter time span or show extensive gaps. To test the quality of the reanalysis records, both temperature and precipitation series were correlated with data from the climate stations of Coyhaique and Balmaceda for the periods where data from these stations was fully available. The corresponding Pearson correlation coefficients are given in Table 3.4.

Obviously, the reanalysis data set follows the precipitation signal of Balmaceda rather than Coyhaique (see 3.2). From AD 1961 to AD 1980, precipitation measured in Coyhaique was constantly higher than P at the Balmaceda station. As Lago Cástor is located in between the two climate stations, the gridded data is most likely the best estimator for annual precipitation at that location. It is expected that this is also true for any other precipitation-related parameter of this dataset. For temperature, the Pearson correlation coefficient suggested negative correlation for the period from AD 1963 – AD 1981 and virtually no significant correlation for the complete period.

Despite the poor correlation, the grid dataset was preferred over the incomplete temperature and precipitation datasets from the nearby climate stations. The gridded data is regarded to represent both parameters more realistically than a climate station from a greater distance than the analysed stations, even if a station like this might potentially have long and gap-free data records.

In addition to temperature (T) and precipitation (P), a set of (grid-independent) climate indices with relevance for the wider study area was added to the dataset. All climate data including information on their origin are listed in Table 3.5. The dataset was later compared with proxy records that are potentially influenced by those parameters.

Table 3.4: Pearson correlation coefficients for correlations of climate station data and reanalysis data. No temperature measurements are available from the Coyhaique station.

Data set 1	Data set 2	time span	Pearson coefficient
annual precipitation sum Coyhaique	Reanalysis 2 x 2 degrees (CRU TS3)	AD 1961 – AD 1980	–0.032
annual precipitation sum Balmaceda	Reanalysis 2 x 2 degrees (CRU TS3)	AD 1961 – AD 1980	+0.054
annual temperature Balmaceda	Reanalysis 2 x 2 degrees (CRUTEM3)	AD 1963 – AD 1981 & AD 1992 – AD 2008	–0.010
annual temperature Balmaceda	Reanalysis 2 x 2 degrees (CRUTEM3)	AD 1963 – AD 1981	–0.206
annual temperature Balmaceda	Reanalysis 2 x 2 degrees (CRUTEM3)	AD 1992 – AD 2008	+0.314

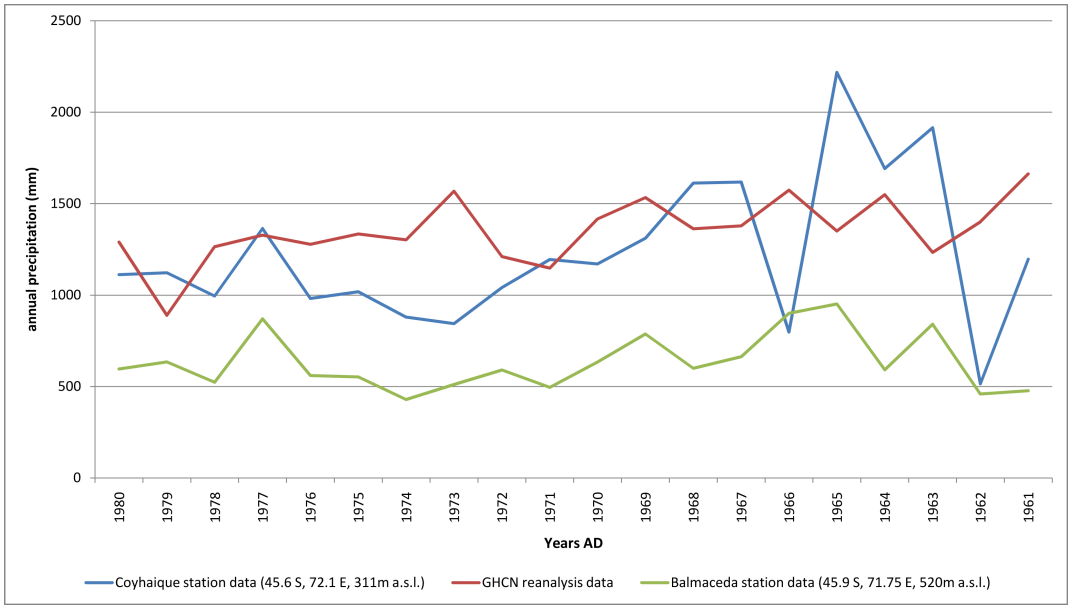

Figure 3.2: Correlation of precipitation datasets from the climate stations of Coyhaique and Balmaceda with precipitation based on a 2 x 2 degree grid cell centred over the study site from a reanalysis dataset obtained from the KNMI database (see table 3.5). The locations of the climate stations are given in the Figure legend.

Table 3.5: Climate variables and indices used in this study. See nomenclature for explanation of the abbreviations.

Variable	Resolution	Time span	Source
T	annual & seasonal	1948 – today	CRUTEM3
P	annual & seasonal	1949 – today	CRU TS3
MEI	annual	1950 – today	NOAA/ESRL/PSD
PDO	annual	1900 – today	N. Mantua, JISAO
SAM	annual	1957 – today	G.J. Marshall, BAS

Figure 3.3: Correlation of a temperature dataset from the climate station of Balmaceda with temperature based on a 2 x 2 degree grid cell centred over the study site from a reanalysis dataset obtained from the KNMI database (see table 3.5). The location of the climate station is given in the Figure legend. Note that the Balmaceda temperature dataset contains a gap of 10 years as indicated in both graphs.

3.13 Data Analysis

The statistics software R was used to pretreat and analyse the results. This command-based software is very flexible, as a high number of pre-programmed packages exist that are needed for the statistical evaluation of the various datasets. A set of specialized statistical R packages was used to handle specific methods and export graphics.

The various data series were synchronized to the same temporal resolution after the stratigraphic correlation was applied and after the final age-depth relationship was determined by the proper age model (see 3.6 and 4.5). Each set of parameters was resampled to a single matrix at annual resolution by using the built-in R-function `approx`. The resampling introduced prominent autocorrelation to all parameters, increasing with decreasing sampling or measurement resolution and getting most distinctive for the carbon-14 dated, low-resolution section of the core. The climate parameters that were available at annual resolution were appended to the data matrix (see list of climate parameters in section 3.12).

The next step was to filter the data with a triangular filter to compensate for uncertainties introduced by bioturbation and sampling (measurement). The filter-induced loss of resolution can be put on the same level with the loss of resolution introduced by the above-mentioned uncertainties. The filter weights each series of data points according to the shape of a triangle. Data in the centre of the subseries to be filtered has maximum weight, while data at the lower and upper ends have the lowest weights. The width of the interval to be weighed can be adjusted with a window parameter. For each variable, this parameter was adjusted according to the estimated sampling or measurement error (see Table 3.6). It also depends on the average number of years represented by the corresponding error interval, which requires temporal information from the final age model (cf. section 4.5). The chosen sampling uncertainty is a best guess. For the data at 0.5 cm resolution that partly spans a zone of low sedimentation rates, a window parameter of 5 was used. The autocorrelation introduced by the triangular filter was considered for the statistical analysis of the filtered data. Note that any statistical method and plot of the data that is presented hereafter is based on the filtered time series only.

Table 3.6: Calculation of the window parameter of the triangular filter. Note that the average number of years per sampling interval depends on the core segment that the corresponding parameter was acquired on. According to the age model, the average number of years per depth interval increased with total sediment depth.

sampling interval [cm]	estimated interval of the sampling or measurement error [cm]	average number of years per sampling interval [yr]	average number of years in the error interval = window parameter [yr]
0.05	±0.1	3	$3yr \cdot \frac{2 \cdot 0.1cm}{0.05cm} = 12$
0.2	±0.4	2	$2yr \cdot \frac{2 \cdot 0.4cm}{0.2cm} = 8$
0.5	±0.5	27	$27yr \cdot \frac{2 \cdot 0.5cm}{0.5cm} = 54$

For preparing the data basis of the statistical analyses, each parameter was rescaled to its original resolution by creating one matrix per resolution. By doing so, the autocorrelation introduced by merging all parameters to the annually resolved time scale was removed. The climate variables were treated in the same manner in order to keep them synchronized to the measurements. For visualization purposes, one extra matrix was created to store a combination of both resolutions of the grain size and BSi data. Due to the primary interpolation, the first and last value of each data series were lost. To still use these observations, the gaps were filled with the corresponding values from depth closest to the depth of the gap, while only introducing a minor error due to the missing interpolation to even ages in the original dataset.

In preparation for the assessment of correlation in the data, each of the equally-resolved groups of variables was tested for correlation by a Principal Component Analysis (PCA), first analysing the variables on their own and then in combination with a set of climate parameters. The aim of this pre-analysis was to distinguish groups of variables with similar variance and thereby similar properties.

After the preparatory steps, the distribution of each variable was tested for normality with the Shapiro-Wilk normality test (cf. Royston 1982). As the nonparametric Spearman rank correlation coefficient (Spearman's rho) does not make any assumption on the distribution of the population, it was chosen as an

alternative correlation measure for the Pearson product-moment correlation coefficient (which requires normality of the data; Kendall 1962, Spearman 1987). Both coefficients were applied on chosen sets of gapless data, including the climate parameters. The time frame of the correlation was mainly limited by the temporal coverage of the climate data set. The significance of the correlation was determined by applying a t-test (Zar 1972), and adjusting the critical values for significance of this test statistic at the 80 % level ("significant results") and at the 90 % level ("highly significant results") according to the degrees of freedom of each parameter. Correlation with significance below the confidence level of 80 % ($\alpha = 0.2$) was regarded as insignificant. The reduced degree of freedom was determined by subtracting the degree of autocorrelation from the total number of observations for each data series. The degree of autocorrelation was obtained from the number of significant lags of the autocorrelation plot based on the `acf` function in R. By that, any autocorrelation leading to an overestimation of the correlations was considered, including autocorrelation previously introduced by the triangular filter.

4. Results and Interpretation

4.1 Lake Biogeochemistry

At the time of coring, the lake water temperature from 2 m below water surface was 12.6 °C. Molluscs were detected in the whole water column, suggesting that they were also present in the topmost centimetres of the lake sediment. Table 4.1 lists the analytical results of the water samples and compares these with world freshwater averages and Patagonian lake water averages.

Table 4.1: Lake water chemistry. Values given in units of $mg\,l^{-1}$. World freshwater averages from Horne & Goldman 1994, Patagonian Andes lake water averages from Diaz et al. 2007.

Element	Cástor (2 m)	Cástor (18 m)	World average	Patagonian Andes average
F	0.051	0.0640	NA	NA
Cl	0.8629	0.8929	7.7	1.12
NO_3	0.0160	0.2059	NA	NA
PO_4	0.0081	NA	NA	NA
SO_4	2.3820	2.4226	11.2	2.06
NH_4	0.0078	0.0028	NA	NA
Na	3.7800	3.9540	6.3	1.99
K	0.3951	0.4135	2.3	0.52
Mg	3.0016	3.0205	4.1	1.26
Ca	6.9100	6.9136	15.0	5.00
Sr	0.0119	0.0078	NA	NA

As already mentioned in the introduction, element concentrations were within a close range for both water samples from Lago Cástor, underlining the dimictic characteristics of the lake. The element were generally less abundant than the world averages, but in good range with the Patagonian means. The above Patagonian average concentrations of sodium, calcium, and magnesium were likely caused by dominant groundwater supply.

4.2 Sediment Description

Figure 4.1 summarizes the core description of CAS-09-1 based on a visual analysis of the split core surface and on a selection of results from the geochemical methods. The estimated mean grain size distribution per depth is indicated according to USGS standard symbolization. A total of three distinct facies were identified.

As a general feature, none of the facies was laminated. Facies 1 was brownish in colour and was predominantly composed of silt-sized grains. According to the low reaction intensity with H_2O_2, it had a medium to low concentration in OM. Few macrofossils (mainly terrestrial plant debris and a mussel) were found at distinct locations, but for the most part of this facies, the sediment was devoid of them. According to these characteristics, facies 1 could be classified as primary lake deposit that was composed of lithogenic and biogenic matter sources from within the catchment. Facies 2 was blackish or white in colour and was dominated by sand-sized grains that partially conglomerate, or it was dominantly silt-sized (only the white layer). The OM concentration of this facies was generally low. Macrofossils were absent. Based on these characteristics, facies 2 was interpreted to be a primary tephra deposit that directly settled to the lake bed, containing only very little of the material from facies 1. Facies 3 was an intermediate type of facies 1 and 2. Its colour ranged from brownish to blackish and its grain size ranged from silt to sand size. The OM concentration of this facies was in between that of facies 1 and facies 2. Macrofossils were not found. Hence, facies 3 was composed of mixed tephrogenic material and primary lake sediment. It was formed by tephra settling through the lake sediment after its primary deposition.

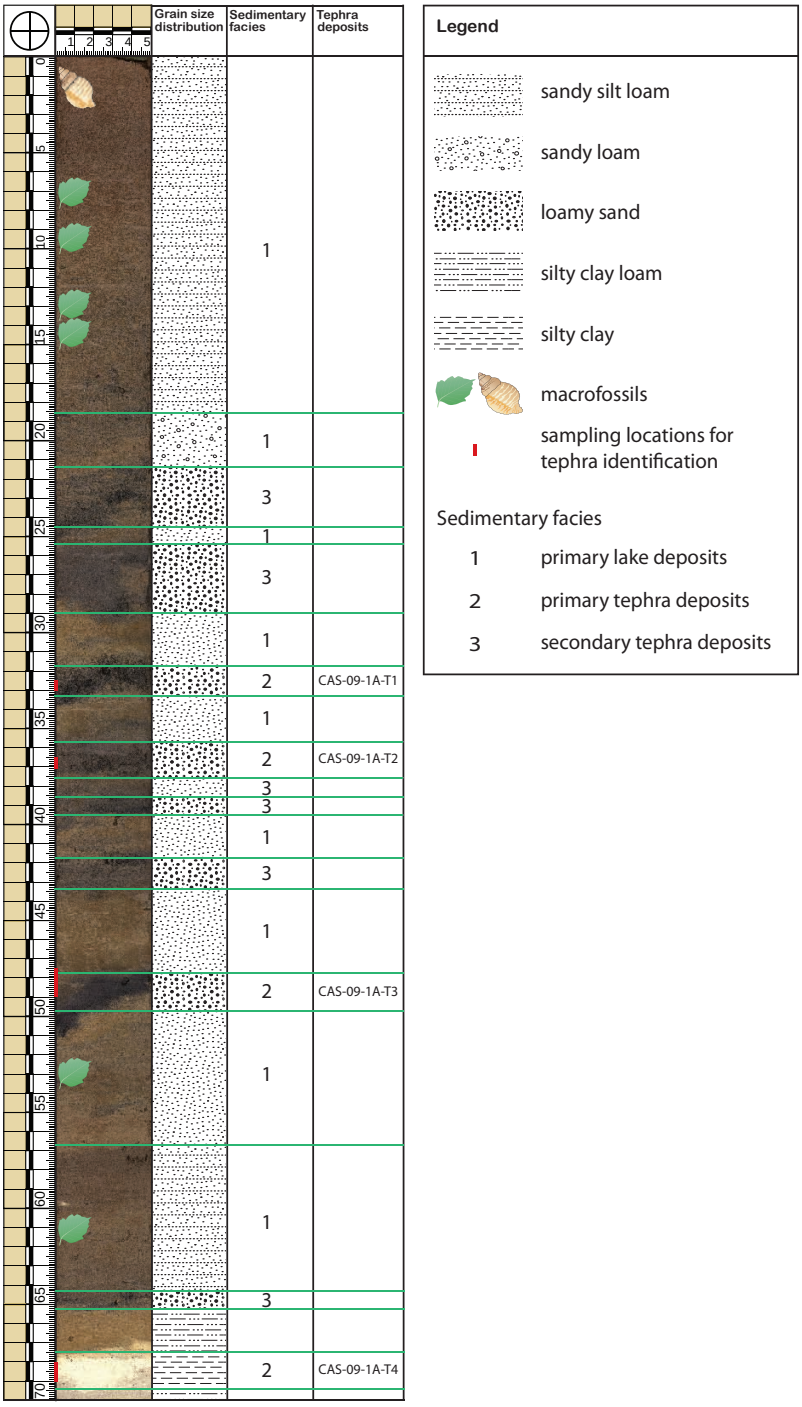

Figure 4.1: Picture and sedimentary facies of CAS-09-1A. Leaves indicate terrestrial macrofossils, shells indicate mussels exposed during sampling. All units in cm.

The presented facies classification was based on the sediment colour, sample treatment with H_2O_2, and a visual analysis of the estimated dominant grain size. The facies division was substantiated by the results of the XRF-based tephra analysis (sampling locations are marked with red stripes in Figure 4.1; see section 5.1). The identified facies were used in some of the following Figures in this chapter.

4.3 Water Content and Mass Accumulation Rate

Water content and MAR over depth are shown in Figure 4.2. Both measures were likely of good quality, accepting that the water content at the time of coring was slightly higher than at the time of sampling, and that water may have moved through the sediment after coring. The water content showed its highest variability at the facies boundaries. As clearly visible in Figure 4.2, MAR and water content were inversely correlated. This was expected, as the mass of a defined volume of sediment with high water content generally weighs more than the same volume of sediment with lower water content.

4.4 Spheroidal Carbonaceous Particles

Counting of four petri dishes at depth of the highest potential SCP concentrations (1 cm, 5 cm, 10 cm, 13 cm) revealed that no or at most only very few SCP-like particles have accumulated in the lake (not more than 4 black particles per sample). These particles did not meet the criteria for an unambiguous attribution as SCPs, and the test counts by other lab personnel did not lead to any consistent numbers of those particles.

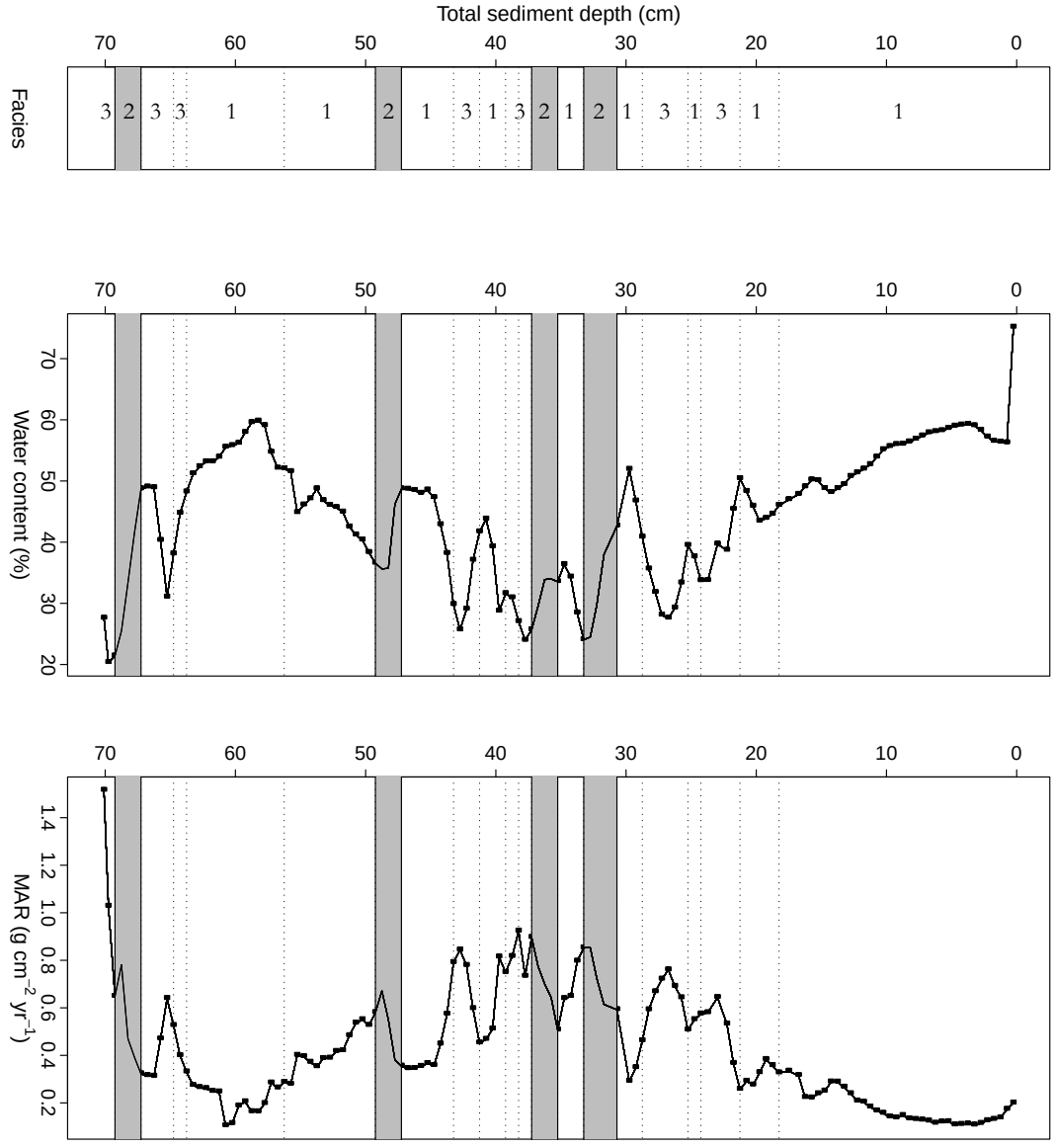

Figure 4.2: Water content and mass accumulation rate of CAS-09-1A determined from samples at continuous resolution of 0.5 cm.

4.5 Sediment Dating

The data relevant for radiocarbon dating are shown in Table 4.2. The OxCal output for all C-14 ages is shown in Figure 4.3 at the end of this section. Included in this Figure is the age of the tephra deposit CAS-09-1A-T4 (67.5–69.4 cm) of 3903 ± 171 cal. yr BP (cf. 5.1). The linear interpolation based on the C-14 dates was linearly extended to the new data point.

Table 4.2: Sample data of CAS-09-1A and results of radiocarbon dating from the Poznan Radiocarbon Laboratory. Facies numbers as defined in section 4.2.

ID (core name + material + depth)	lab id (Poznan Radiocarbon Laboratory)	facies [No.]	weight [g]	age [C-14 yr BP]	age [C-14 cal. yr BP]
CAS-09-1A-bulk (17.75–18.25 cm)	Poz-33733	1	2.5184	795 ± 30	708 ± 50
CAS-09-1A-bulk (23.1–23.6 cm)	Poz-33734	2	1.5994	1040 ± 30	946 ± 66
CAS-09-1A-bulk (30.5–31.5 cm)	Poz-31858	1	7.547	1910 ± 30	1853 ± 60
CAS-09-1A-bulk (60.0–61.0 cm)	Poz-31859	1	5.821	3125 ± 35	3359 ± 64
CAS-09-1A-macro (60.0–61.0 cm)	Poz-31860	1	3.279	3100 ± 35	3347 ± 61

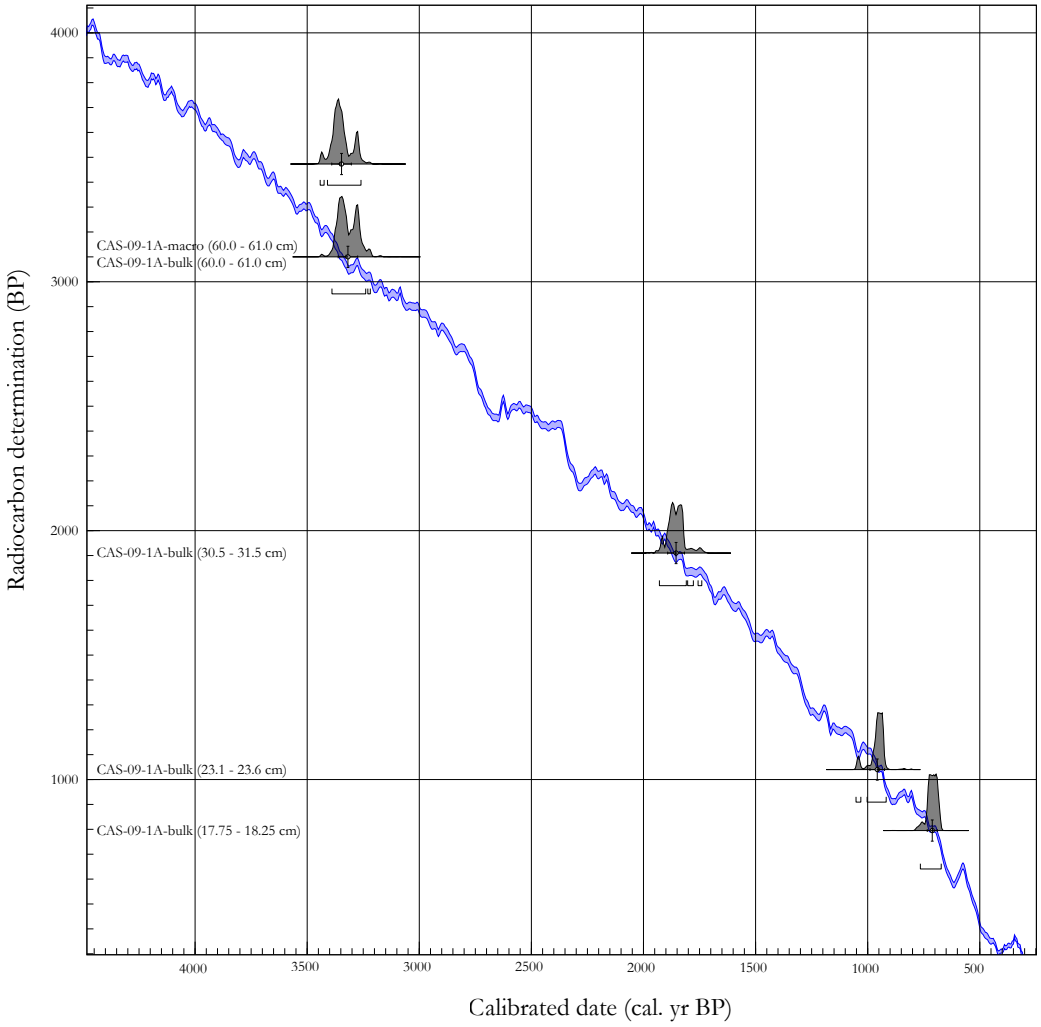

Figure 4.3: SHCal04 Southern Hemisphere atmospheric curve (McCormac et al. 2004) with radiocarbon dates from Table 4.2. Also shown are the probability density functions (exaggerated) and the corresponding confidence intervals for each radiocarbon date as described in section 3.5.2. Note that the probability density plot of CAS-09-1A-macro (60.0–61.0 cm) is vertically displaced to improve readability. Plotted with OxCal v4.1.5 (Ramsey 2001).

Table A.2 (appendix) lists all raw ^{210}Pb sample data obtained from Eawag Dübendorf. The lead-210 age models (CIC, $CRS_{unconstrained}$, and $CRS_{constrained}$) are shown in Figure 4.4. The CIC model was rejected due to numerous age inversions. Hence, the assumption of a constant initial concentration of ^{210}Pb made by the model was not valid for Lago Cástor. The unconstrained CRS model was rejected as well, because it did not match to the ^{137}Cs peak at its depth of 2.5 ± 1 cm. Figure 4.5 shows the constrained CRS model with included error estimates from the model after application of the stratigraphic correlation. The stratigraphic correlation is visualized in Figure 4.14 in section 4.6.2.

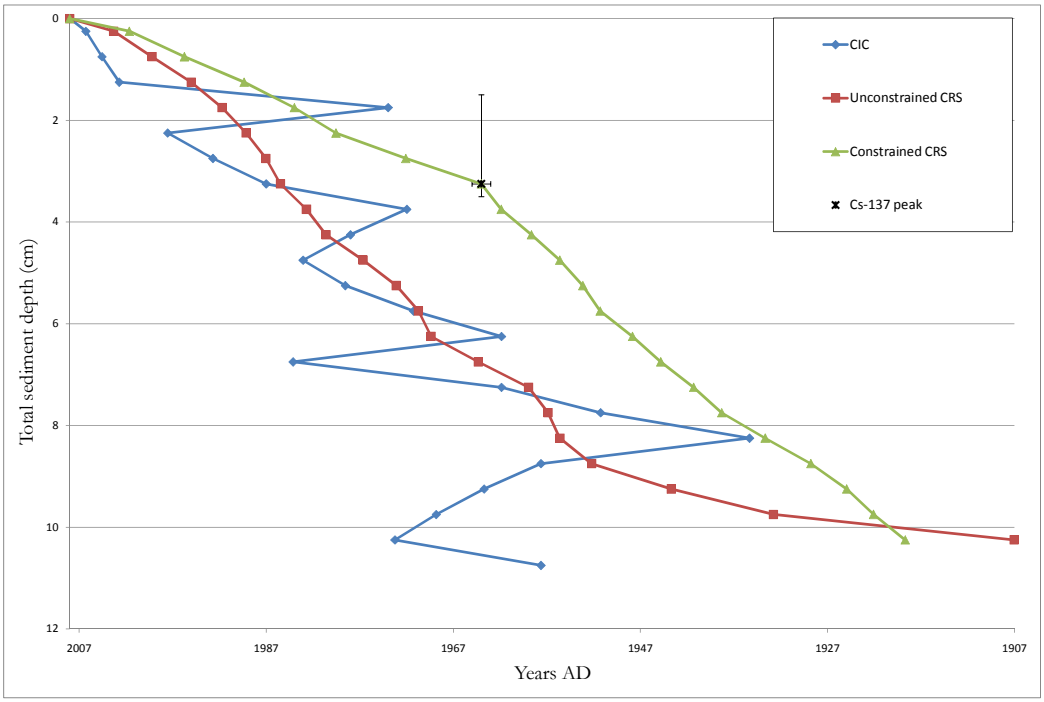

Figure 4.4: Comparison of lead-210 based age-depth models for the core CAS-09-3. Error bars of the ^{137}Cs peak correspond to the uncertainty of the peak of ± 1 year and to the uncertainty of the correct depth of the ^{137}Cs peak within the core. Note that due to mathematical constraints no data was calculated for the data points of both CRS models at 10.75 cm total sediment depth.

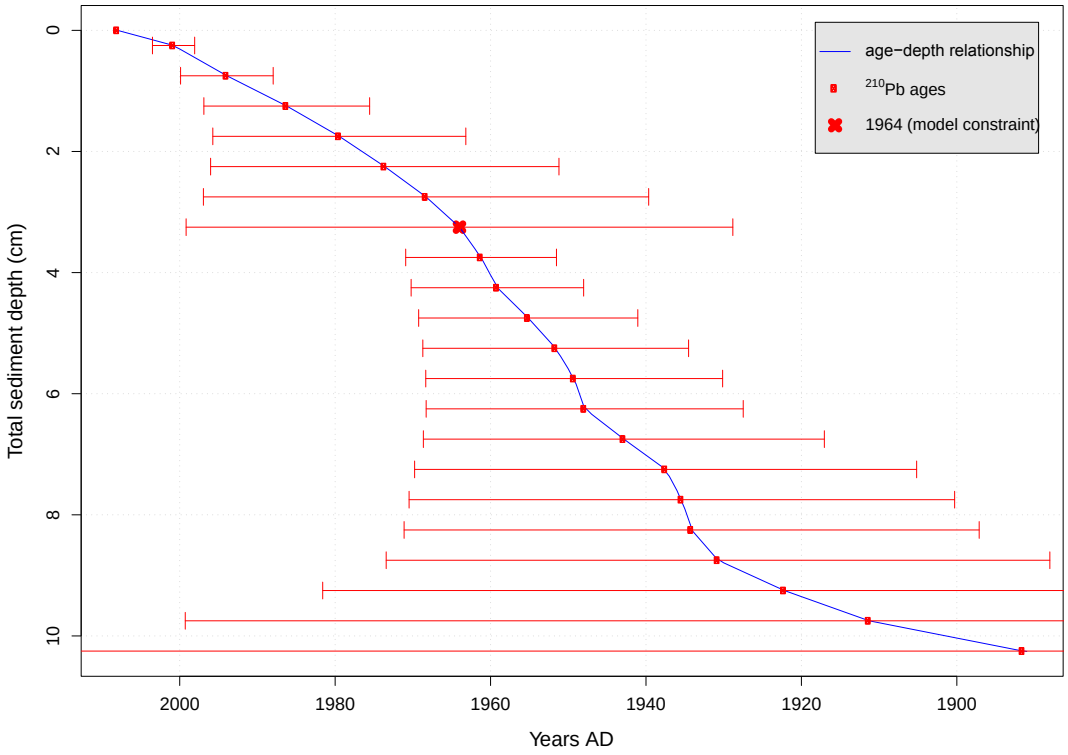

Figure 4.5: Final lead-210 CRS model ($CRS_{constrained}$). Red bars indicate the standard deviation from the mean age as determined by the model. The full extent of the error bars is shown in Figure 4.6 (next page).

Figure 4.6 shows the final age-depth model for both the lead-210 and the carbon-14 dated core segments. Note that the oldest age of the ^{210}Pb model was linearly interpolated to the youngest calibrated ^{14}C date. Taking account of the abrupt slope change of the model at depth of 10.75 cm in conjunction with the large uncertainty of the lowest lead dates, it was possible that the age at the lower end of the ^{210}Pb model (10.75 cm total sediment depth) was not correctly estimated. But as no clear evidence was found for that, the given age model was accepted.

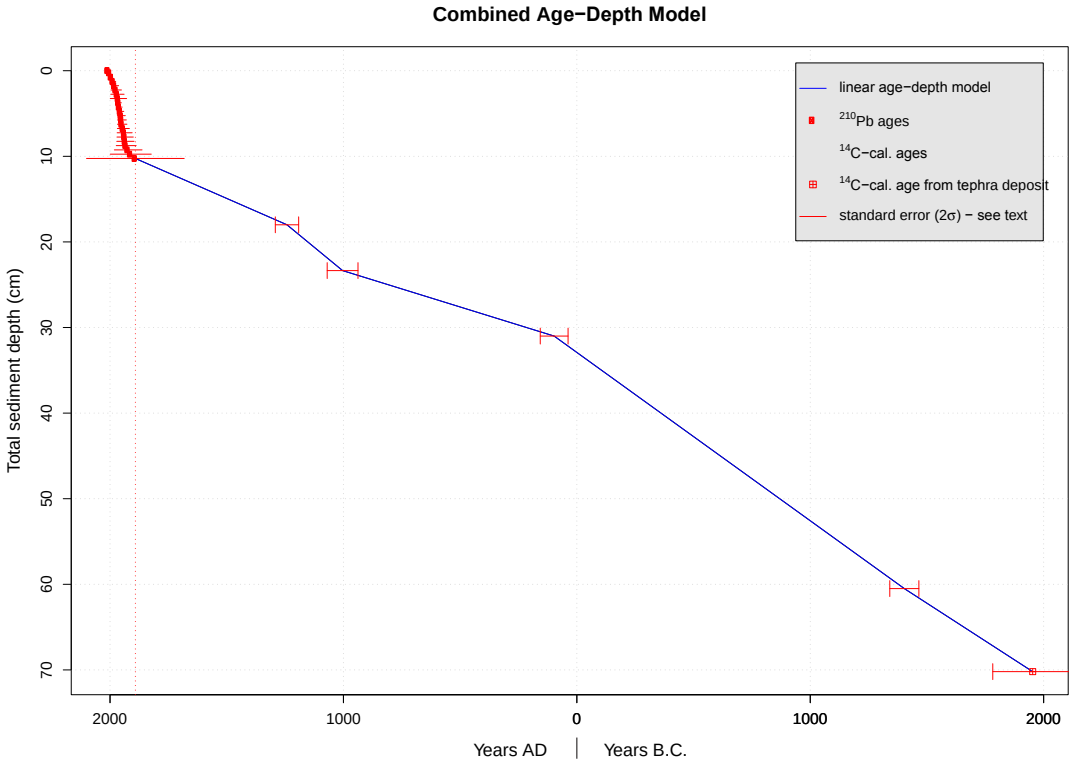

Figure 4.6: Combined age-depth model for the complete core CAS-09-1 including the age constraint of the tephra layer CAS-09-1A-T4 (67.5–69.4 cm). A remarkable slope change is located at the intersection of the lead-210 and the carbon-14 based age models (indicated by the red dashed line; see discussion in the text). The error bars correspond to the 2 *sigma* error that is an output of the CRS model (lead-210 dated core segment) or derived from the C-14 age model (carbon-14 dated core segment; see 3.5.2).

4.6 X-Ray Fluorescence

4.6.1 XRF Core Scan

The XRF-derived lithogenic proxies from Table 3.2 were plotted in Figures 4.7 to 4.12. Lithogenic facies were indicated by their number (see 4.2). All elements were shown except for uranium and arsenic that were not measured with the XRF scanner. However, the lack of in-situ produced radium-226 in the lake sediment suggested that uranium was absent in the catchment. As human impact on the lake over the last centuries was marginal except for forest burning and clearance, arsenic was most likely also absent.

The XRF scans were generally of sufficient quality in order to be used as paleoenvironmental proxies. None of the data series was below the critical limit of 150 cps. This was valid for the data shown in Figures 4.9 to 4.12, except for the most part of the counts of Zn, Br, and Rb, where the rate only exceeded the critical range in a narrow depth range. The ratios were exempt from the quality limitation, as they were entirely based on elements that met the quality criteria mentioned above. Besides those limitations, the count rate of Mn seemed to be strongly affected by high-frequency variability that was likely due to a high sensitivity of the measurement. In addition to that, the high iron counts may have influenced the count rates of other elements (see Table 3.2). Still, the XRF proxies were based on a solid data base and could be used as proxies. The following paragraphs describe the results with respect to tephra identification (cf. 4.5), and in terms of their usage as paleoenvironmental proxies of general or constrained validity as listed in Table 3.2.

Most of the element concentrations and element ratios showed distinct peaks or rapid changes with age at depth of the tephra layers. Most dominant for tephra deposit CAS-09-1A-T4 (67.5–69.4 cm) were the element (ratios) Al, Al/Fe, Si, K, and Zr. For the remaining tephra layers of CAS-09-1, the elements Si, Ca, Ti, and Fe showed the clearest deviations at depth of these deposits. The Ca/Al ratio provided no evidence of tephra in this lake. Peaks or rapid changes not attributed to the sampled tephra layers were mainly less pronounced. This was of course due to the fact that the XRF scan parameters were previously used as decision

support for the actual selection of the tephra layers. In contrast to the mainly abrupt changes most likely associated with facies boundaries, alterations of the XRF parameters with time generally had the characteristics of slow transitions. The strong influence of the tephra deposits may also have masked the true extent of low-amplitude trends and fluctuations. This made it increasingly difficult to use the proxies as paleoenvironmental indicators (cf. Table 3.2). The XRF-derived proxies are synthesized in the next paragraphs.

Redox conditions (as indicated by the Mn/Fe ratio) showed a rather chaotic behaviour from 2000 B.C. until a zone of low redox conditions at low variability was reached at around AD 500, followed by a slow and then rapid increase until today. For the period before AD 500, the proxy was supported by the correlation between Mn and Fe counts (Pearson correlation coefficient of 0.62; cf. Table 3.2), whereas conditions after AD 500 have arguably changed, as supported by the Mn-to-Fe Pearson correlation of only 0.11. As the correlation measure was partially high for Lago Cástor, the redox indicator was regarded as valid.

Similar to the Mn/Fe ratio, the level of Sr in the lake sediments (indicating silicate weathering) showed high variations until AD 500 followed by a more stable decline until today. The validity of this indicator has to be tested with the help of other proxies (see 4.11). Ca can not be used as an indicator for carbonate weathering, as carbonates were ruled out for at least the bulk of the sediment (see 5.2.1). The Zn counts were almost entirely below the critical limit, supporting the absence of mining activities (cf. section 1.2.3). Except for the tephra layer CAS-09-1A-T4 (67.5–69.4 cm), Rb and Zr both showed near-constant conditions, which was expected from their high resistance properties. K and Ti concentrations seemed to have been almost entirely dependant on facies only and were hence rejected. All indicators for pedogenic sediment input showed different shapes and no distinct peaks, suggesting that they did not encode signals of pedogenic sediment input from the catchment. However, the variability of Ca/Fe over time clearly dominated over the other ratios, showing a gradual shift from a high variability (2000 B.C. until AD 500) to rather stable conditions until today. The application of Br as a proxy for OM concentration remained an open question. It is addressed later in section 4.11.

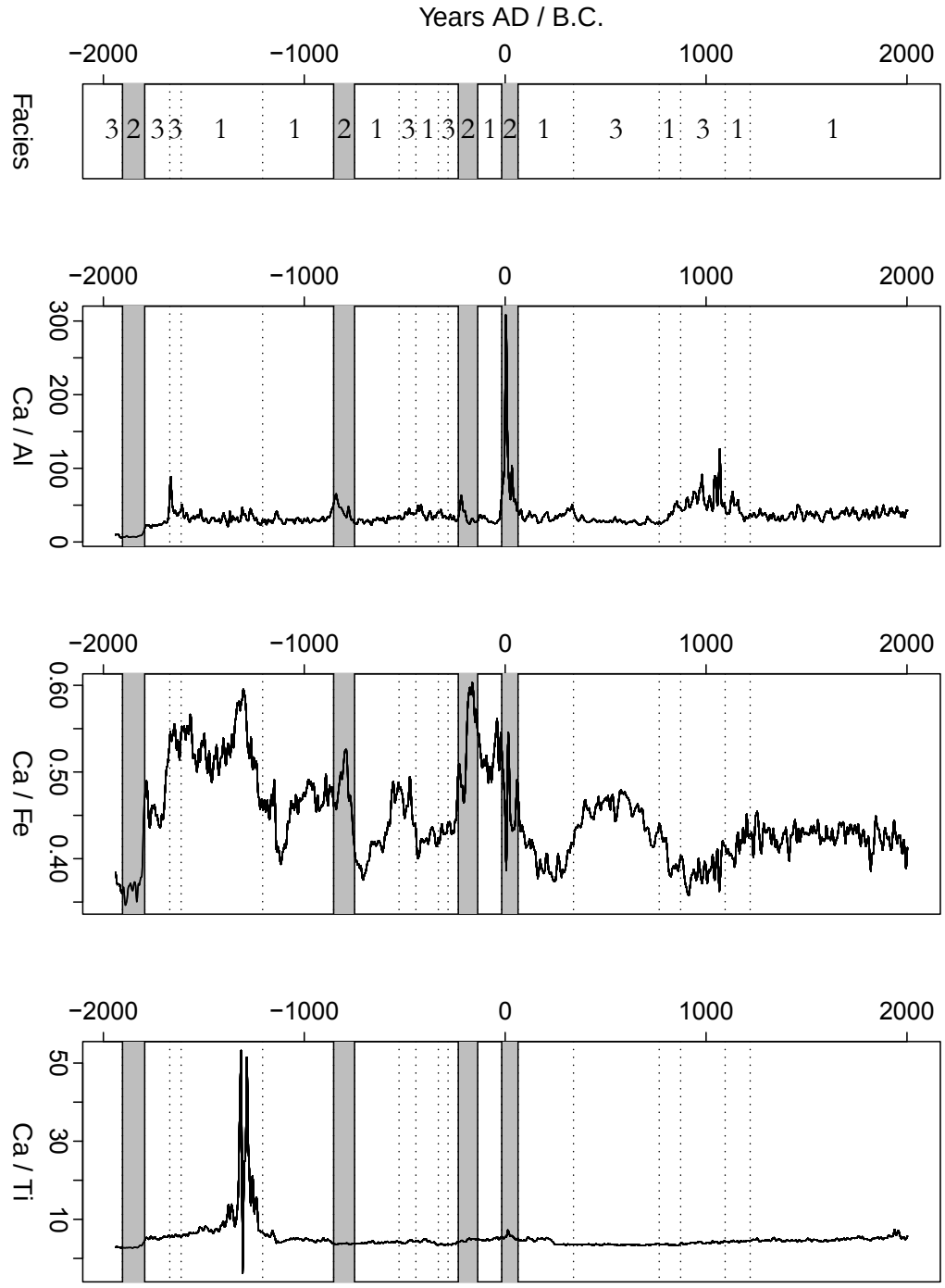

Figure 4.7: Element ratios calculated from qualitative XRF scan data. Years B.C. are negative (applies to all of the following 5 graphs).

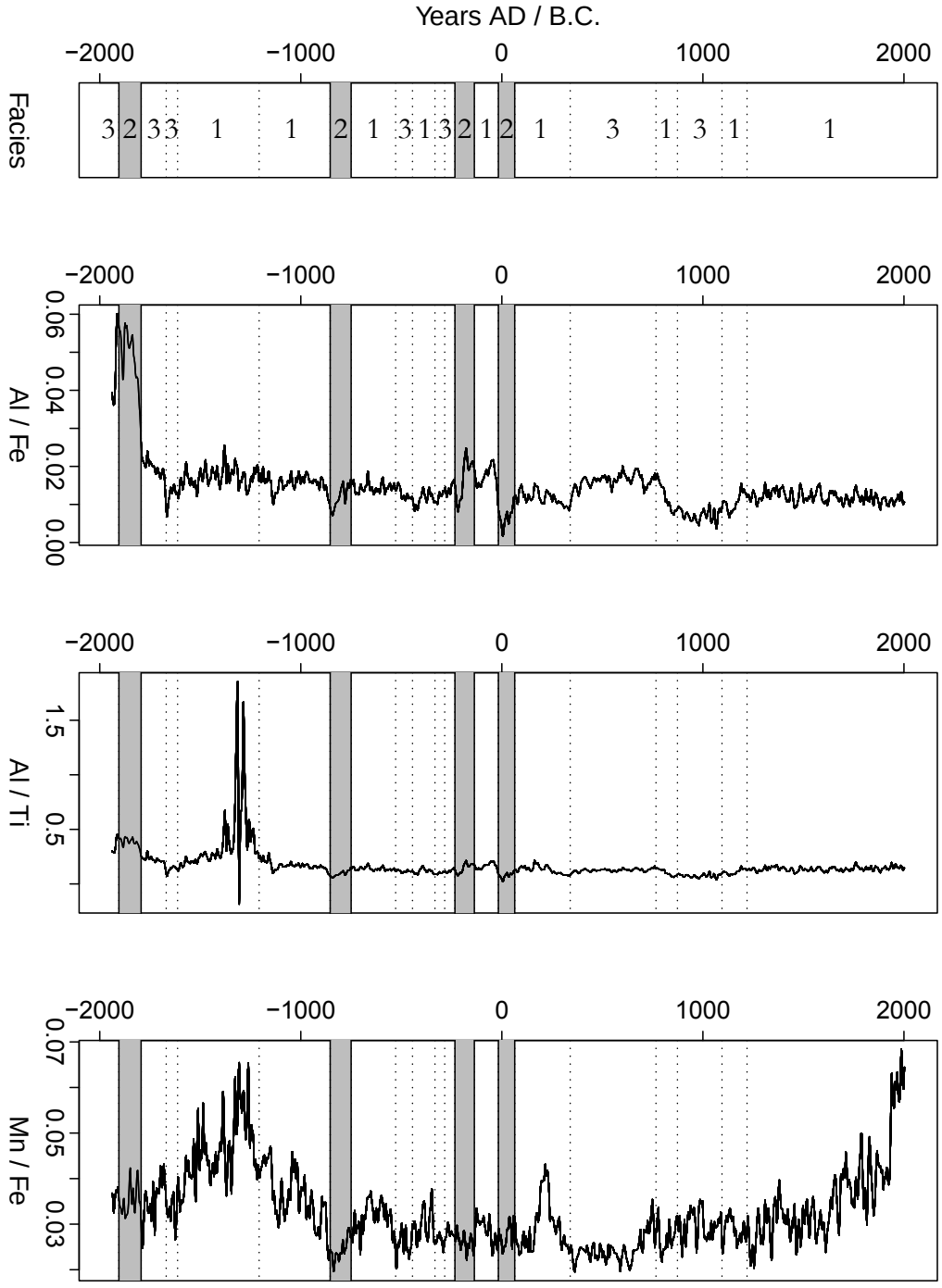

Figure 4.8: XRF proxies (2/6).

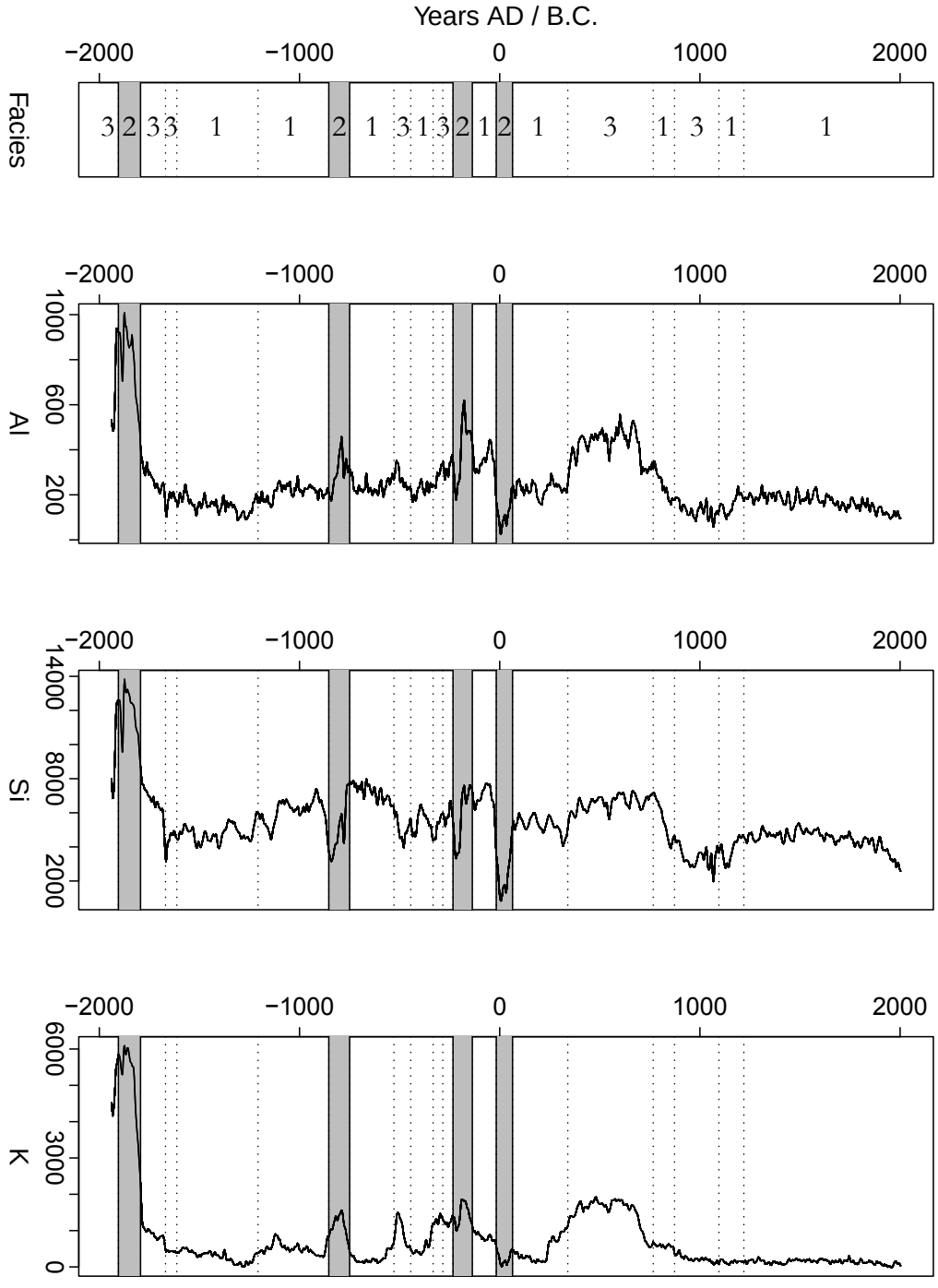

Figure 4.9: XRF proxies (3/6).

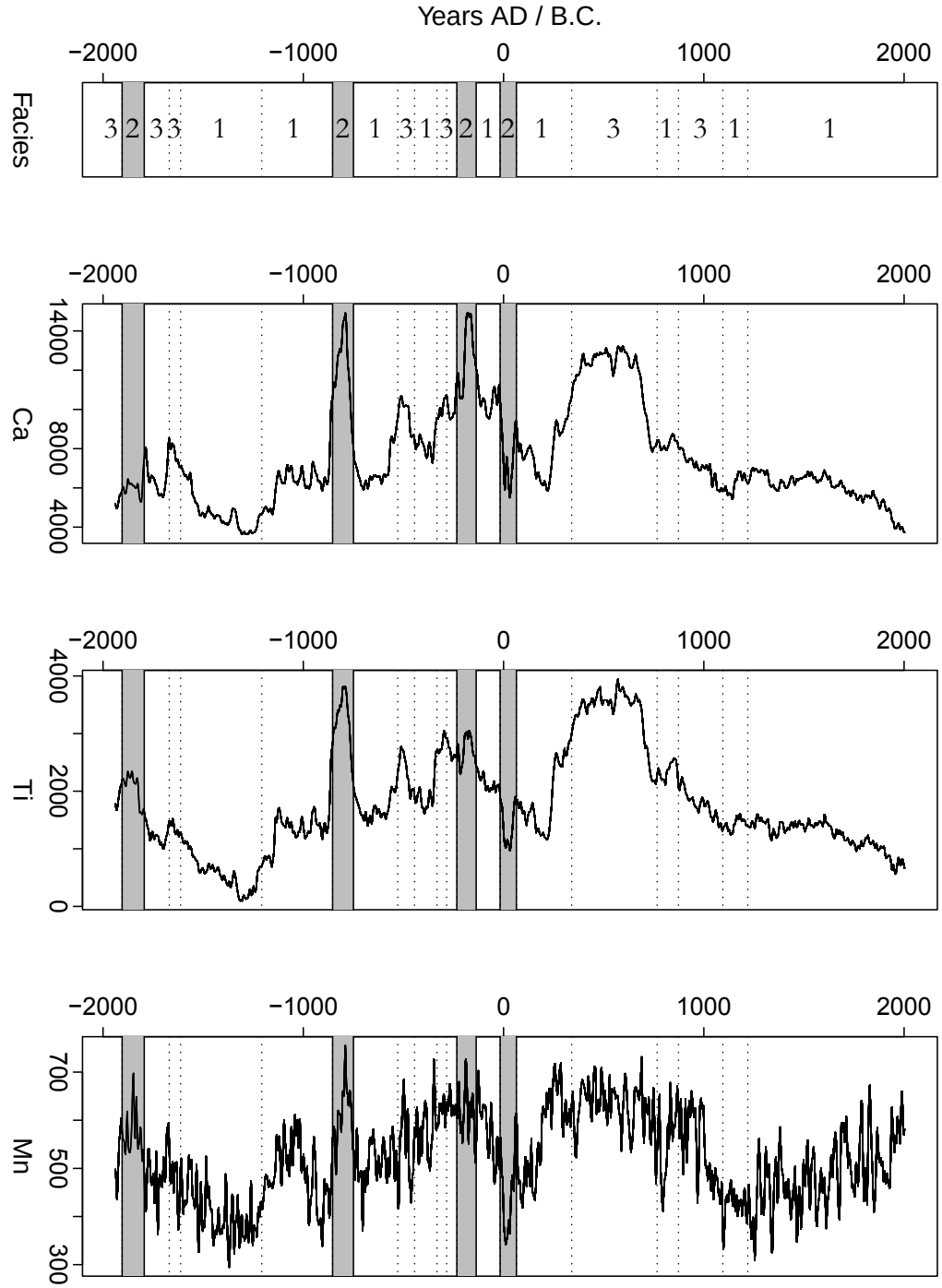

Figure 4.10: XRF proxies (4/6).

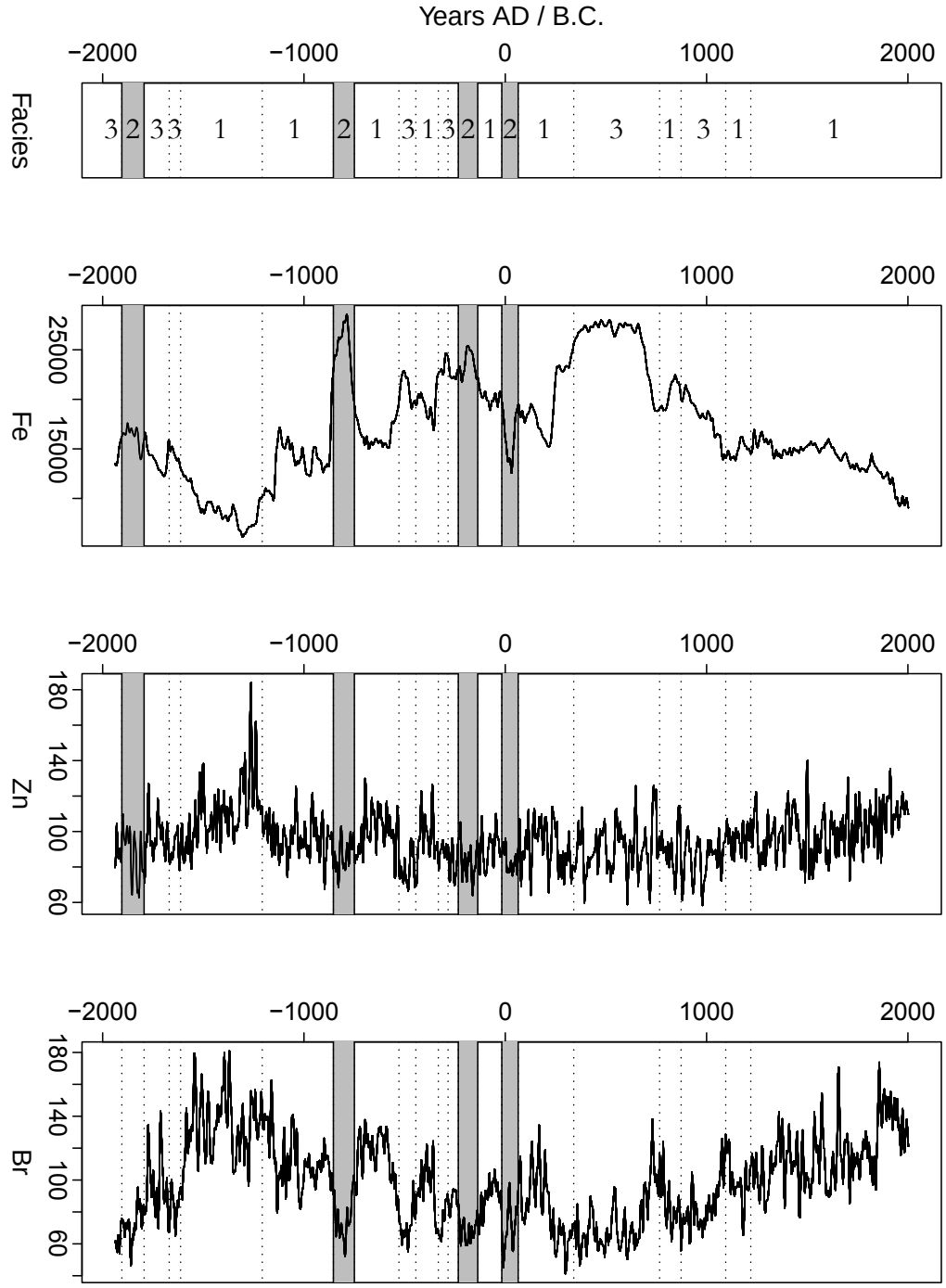

Figure 4.11: XRF proxies (5/6).

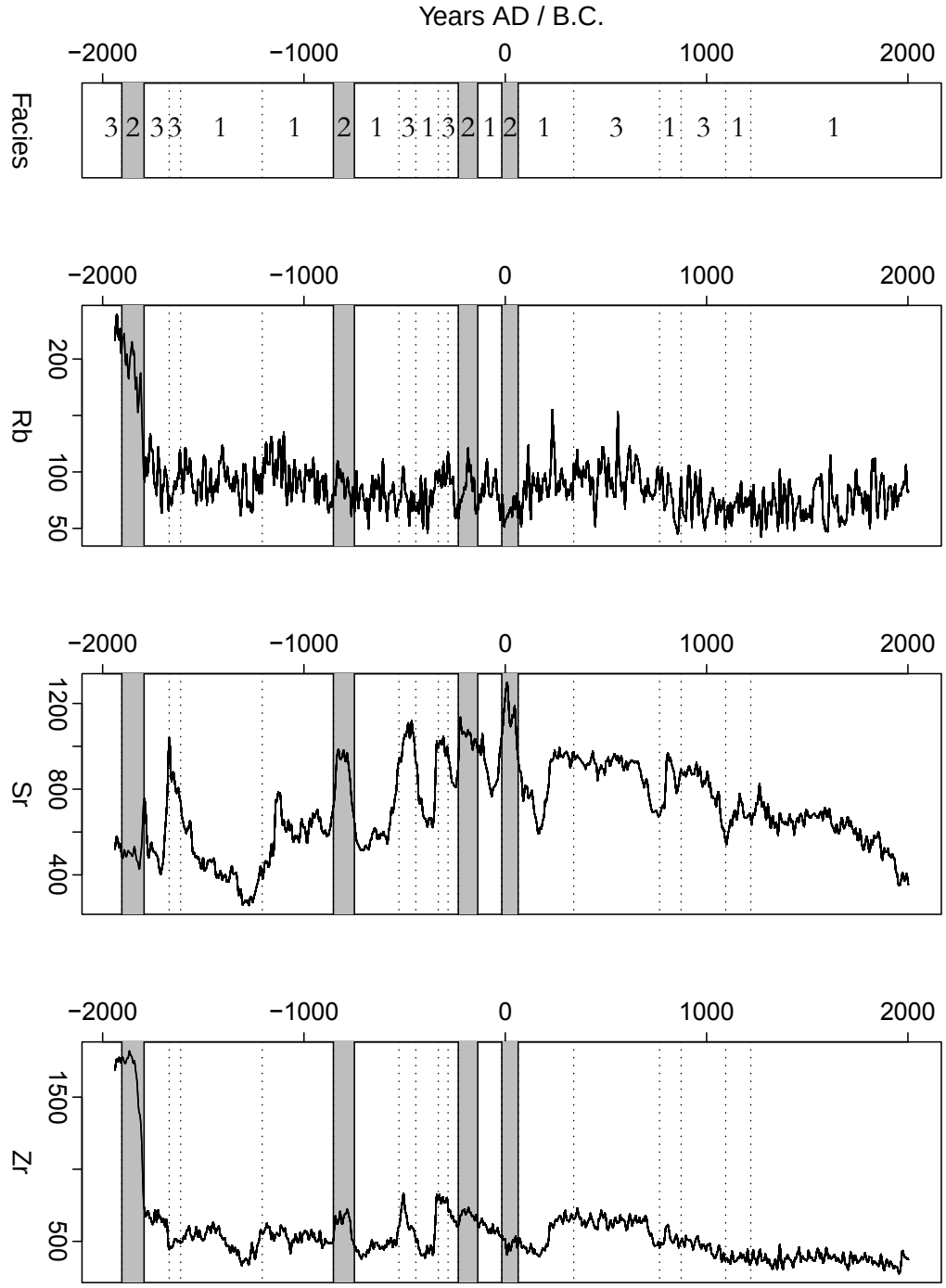

Figure 4.12: XRF proxies (6/6).

4.6.2 XRF of Single Samples

The sample-based XRF analysis from both the averages of each pair of glass pills (CAS-09-1A-T1-xrf (31.9–32.5 cm) – CAS-09-3A-T3-xrf* (43.2–44.0 cm)) and the results based on the powder pill (CAS-09-1A-T4-xrf-P (67.5–69.4 cm)) revealed element compositions as listed in Table A.5 (elements are given in oxidised form). The second lowest row labelled as "sum" contains the aggregated element proportions of each glass pill that should add up to 100 %. As this was true, the data quality was proven to be high. The row "LOI" gives the proportions of loss on ignition determined during sample pretreatment (see 3.7.2). In Table A.5, "NA" indicates concentrations below detection limit.

Figure 4.13 shows ratios of parameters that have been chosen from the elements listed in Table A.5 in consideration of the type of diagrams used in the literature (see discussion in 5.1). What stood out is the closeness of the two lowest samples from CAS-09-3 (CAS-09-3A-T2 (36.1–37.4 cm) and CAS-09-3A-T3 (43.0–44.1 cm)) to the uppermost sample of CAS0-09-1 (CAS-09-1A-T1 (31.7–33.3 cm)). This was partially supported by the grain size data of these samples (see Figure 4.19 on page 80). It was regarded very likely that these tephra deposits were from the same volcanic source or even from the same eruption (cf. 5.1). The samples from the two central deposits of CAS-09-1 (CAS-09-1A-T2 (35.7–37.6 cm) and CAS-09-1A-T3 (47.5–49.7 cm)) nearly showed a similar composition, but differed in some aspects, including a different grain size distribution. The sample from the lowest tephra deposit of CAS-09-1 showed a very different composition in mainly in SiO_2, but also in K_2O, Al_2O_3, CaO, Fe_2O_3, TiO_2, and P_2O_5, suggesting that it originated from other volcanic sources than the upper deposits. This was in accordance to the qualitative element concentrations and ratios given in Figures 4.7 to 4.12, and to the grain size data (Figure 4.19), which underlined the very different characteristics of this tephra layer in comparison to the others. The same was true for the composition of CAS-09-3A-T1 (32.5–33.0 cm), although its grain size distribution was highly similar to the one of CAS-09-1A-T1 (31.7–33.3 cm) (see Figure 4.19). Section 5.1 sets the tephra composition in context with compositions of known and dated tephra deposits as described in the literature. The tephra intercomparison lead to the extended stratigraphic correlation as shown in Figure 4.14.

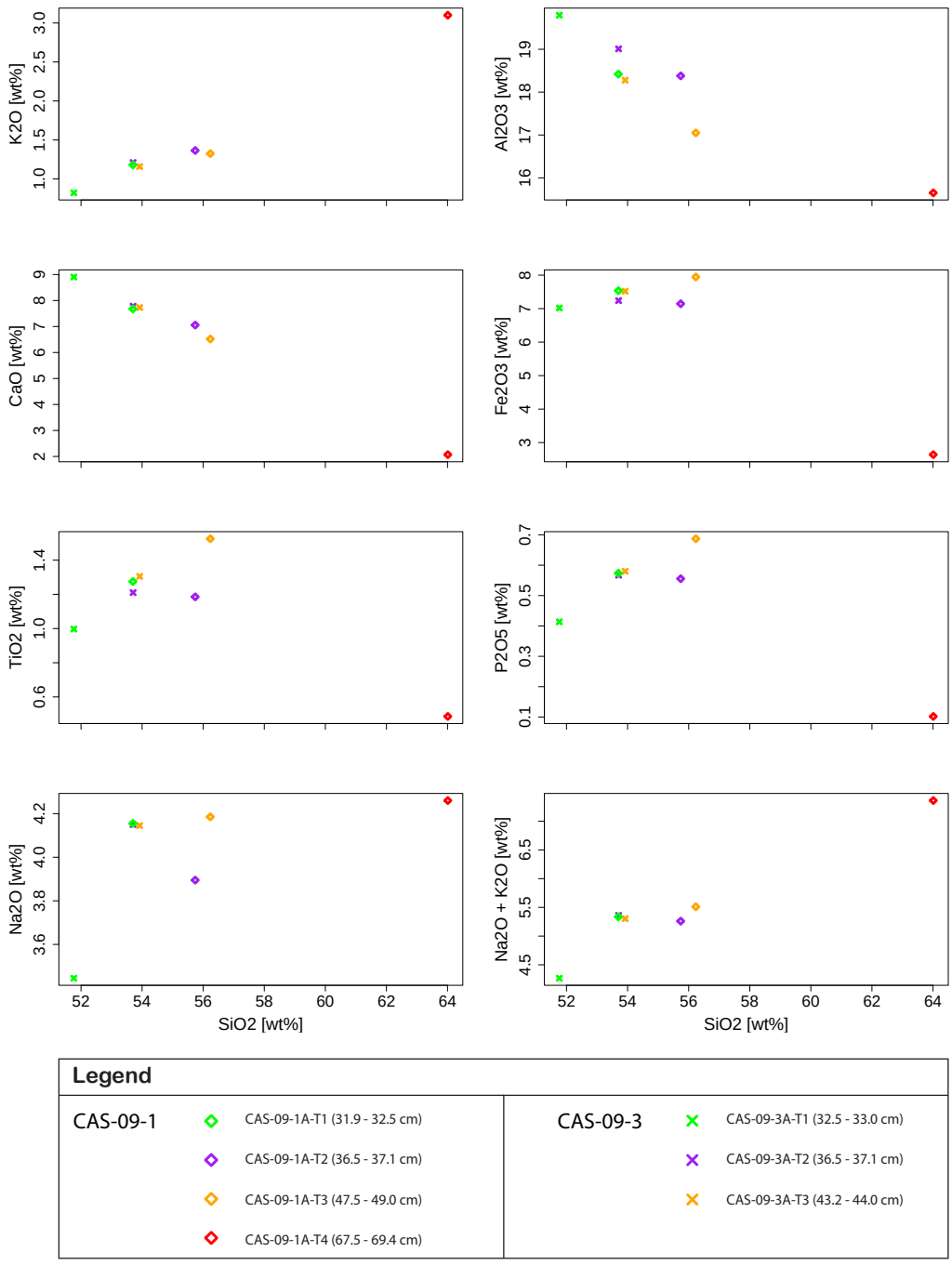

Figure 4.13: A selection of element ratios of the Lago Cástor tephra samples from core CAS-09-1 (squares) and CAS-09-3 (crosses). Colour coding as shown in the legend.

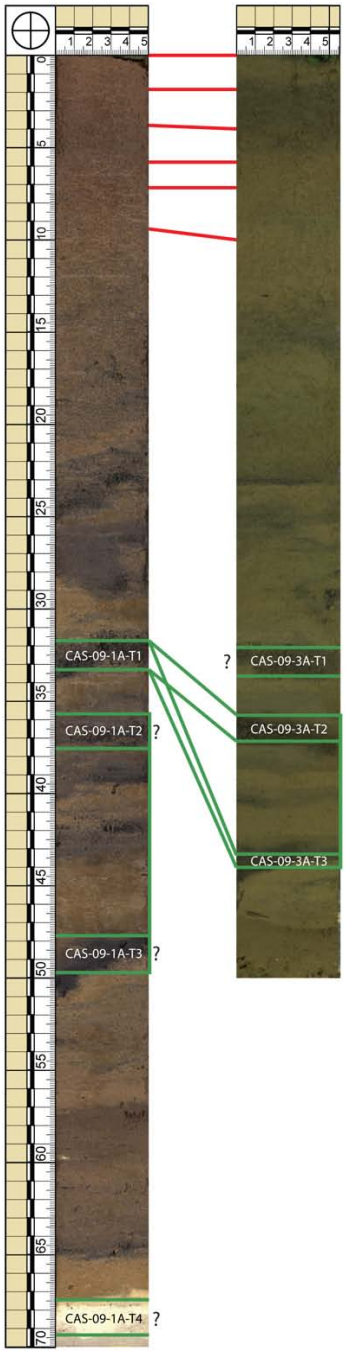

Figure 4.14: Stratigraphic correlation between the lake sediment cores CAS-09-1 and CAS-09-3 based on manual comparison of the in-situ reflectance spectroscopy parameter $\frac{R_{700}}{R_{675}}$ for the lead-210 dated core segment (red bars; see corresponding numbers in Table A.4), and on tephra intercomparison (green bars).

4.7 Scanning In-situ Reflectance Spectroscopy

The ratios (proxies) derived from the in-situ reflectance spectroscopy measurements (Table 3.3) are plotted over time in Figure 4.15. Total chlorine (upper graph) varied with facies boundaries, but also showed some peaks during the unperturbed periods. Nevertheless, clear trends could not be detected. Lithogenic content (middle graph) seemed to be influenced by tephra, but also showed variations at depth of unperturbed periods. As expected, this proxy showed above-average values at depth of the sampled tephra layers. Still, it did not provide an unambiguous indicator for those deposits, which may have been caused by redeposition of fine-grained bulk sediment. The variability of this parameter increased remarkably over the last centuries. The proxy for the degree of diagenesis (bottom graph) showed variations at depth of the facies boundaries and within the facies. Except for the last decades, an increasing trend was quite eminent. Surprisingly, this proxy gave only limited information for the identification of tephra deposits.

4.8 Carbon/Nitrogen Ratio

The measurement results of the C/N ratio were most likely unaffected by measurement errors, as the total amount of carbon and nitrogen were well above the detection limit for each sample. The results of all available measurements are illustrated in Figure 4.16. The broad peak around AD 500 partially coincided with the secondary tephra deposit located at that depth (cf. 4.1). The sharp peak around AD 1100 was likely due to a drastic event and not has probably not been caused by a systematic measurement error, as it was supported by more than one data point. From then until around AD 1900, the ratio remained on a high level of around 10. After that, a rapid decrease was recorded, which was mainly driven by an increase in nitrogen and a simultaneous slower increase in Carbon. The ratio never exceeded the critical limit for terrestrial OM origin of 20, but often dropped below the limit for dominance of aquatic OM sources of around 10. This could not be explained by the location of the coring site, which was in a central part of the lake, but not far from the shore (Figure 2.3 on p. 15).

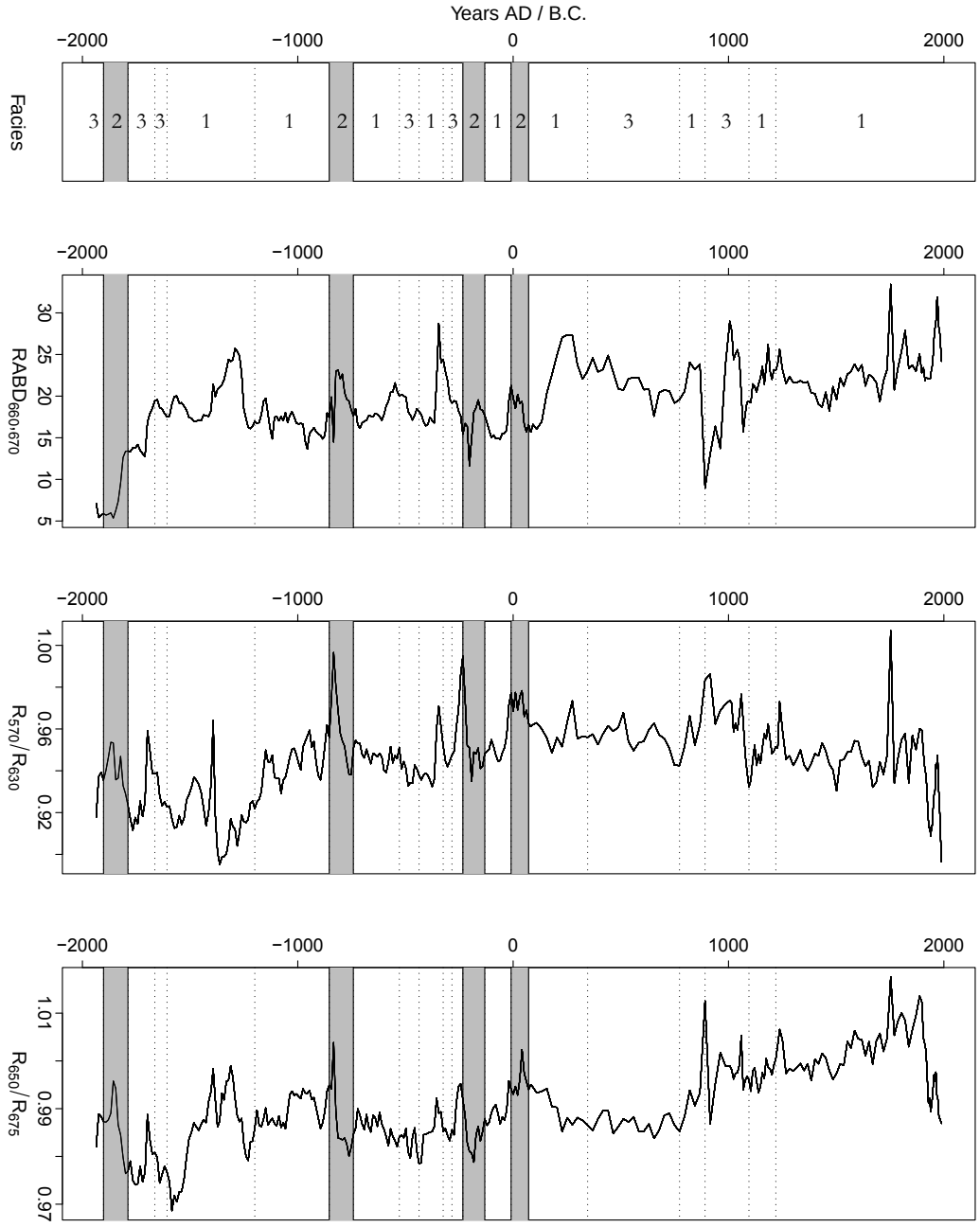

Figure 4.15: Proxies determined by scanning in-situ reflectance spectroscopy. The upper graph shows the proxy for total chlorine, the graph in the middle displays the proxy for lithogenic content, and the bottom Figure plots the indicator for the degree of diagenesis.

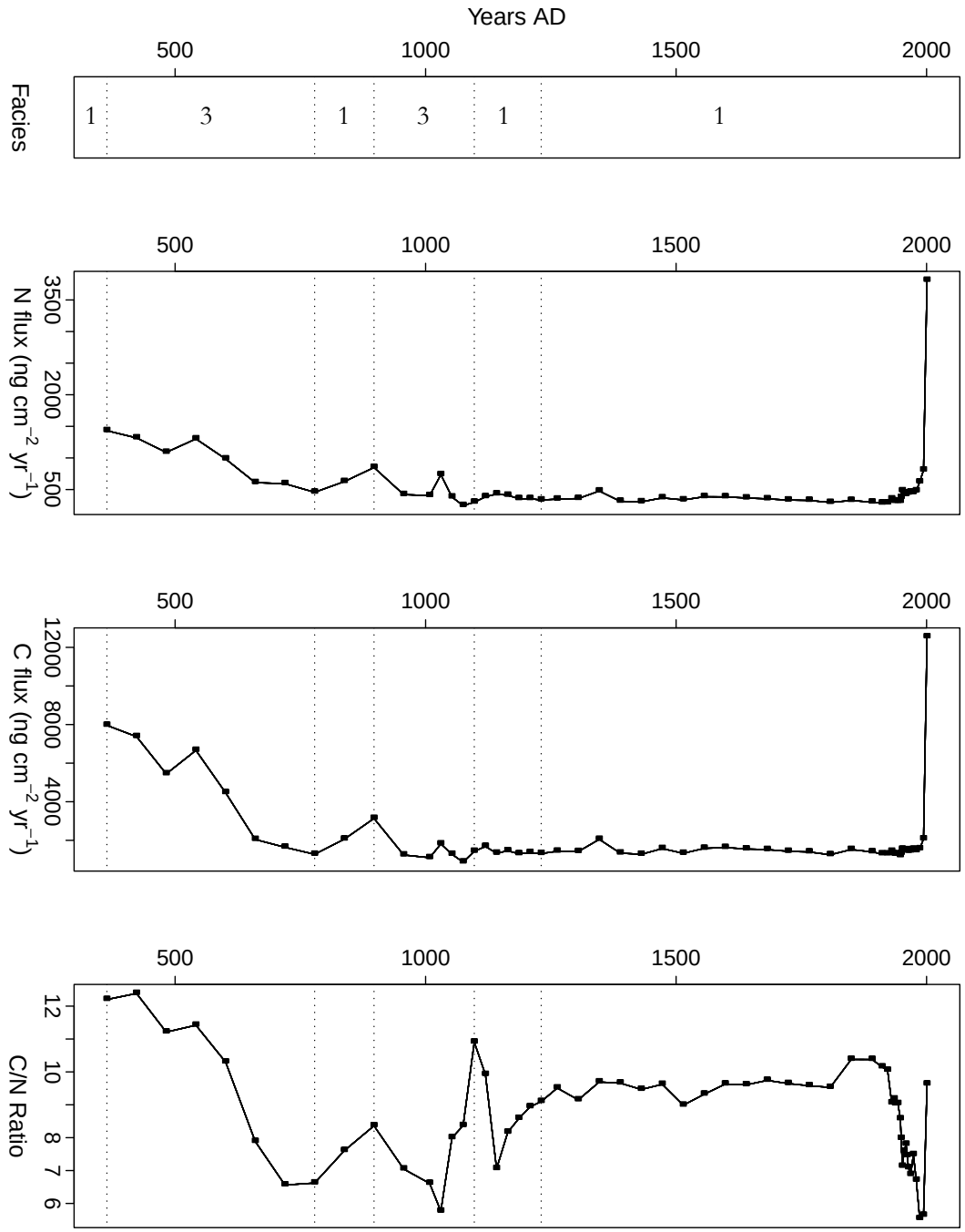

Figure 4.16: C/N ratio and fluxes of organic carbon and nitrogen.

This strongly suggests, that aquatic nitrogen from the lake has always dominated over sources of terrestrial carbon within its catchment over the investigated time span. The probable causes for the low values from ca. AD 1900 till AD 1995 were presented in the discussion (section 5.3.2).

The fluxes of carbon and nitrogen both showed a dramatic increase over the last years. The loss of nitrogen over time may have been due to an intense nitrogen fixation within the uppermost lake sediments, whereas the carbon loss was interpreted as a result of remineralization processes in the surficial sediments. It can not be refused that the increase of both fluxes may also have been a result of a simultaneous increase of both aquatic productivity and terrestrial carbon influx. Apart from this deviation, both fluxes remained on a very constant low level, and large-scale changes in the C/N ratio were increasingly determined by small-scale variations in carbon and nitrogen fluxes.

4.9 Biogenic Silica Flux

Except for an unquantified uncertainty in the biogenic silica data, no errors were introduced by the measurements of BSi. Figure 4.17 shows both the total amount of biogenic silica and the corresponding flux. The BSi flux was in accordance with the total amount of BSi per sample. Very apparently, the BSi concentrations and the BSi flux remained on a rather stable level from AD 1500 until the early 20^{th} century, where the variability rapidly increased. However, the true amplitude of the parameter may have been masked for the time before AD 1948 as a result of the the low sampling resolution and the low sedimentation rate. To show the development of the 0.2 cm resolved subseries in more detail, the lower graph in Figure 4.17 shows the development after AD 1948 only. Evidently, there was a decrease in the BSi flux from around AD 1950 till AD 1960. After a period of stagnation, the flux increased dramatically around AD 1972. Until today, the flux was characterized by above-average variability, but also by an ongoing increase. Note that as the time series of the middle and upper graph consist of different resolutions, they are not used for the statistical analysis directly. The flux is discussed with respect to its relation to climate parameters in the overall statistical assessment at the end of this chapter (section 4.11).

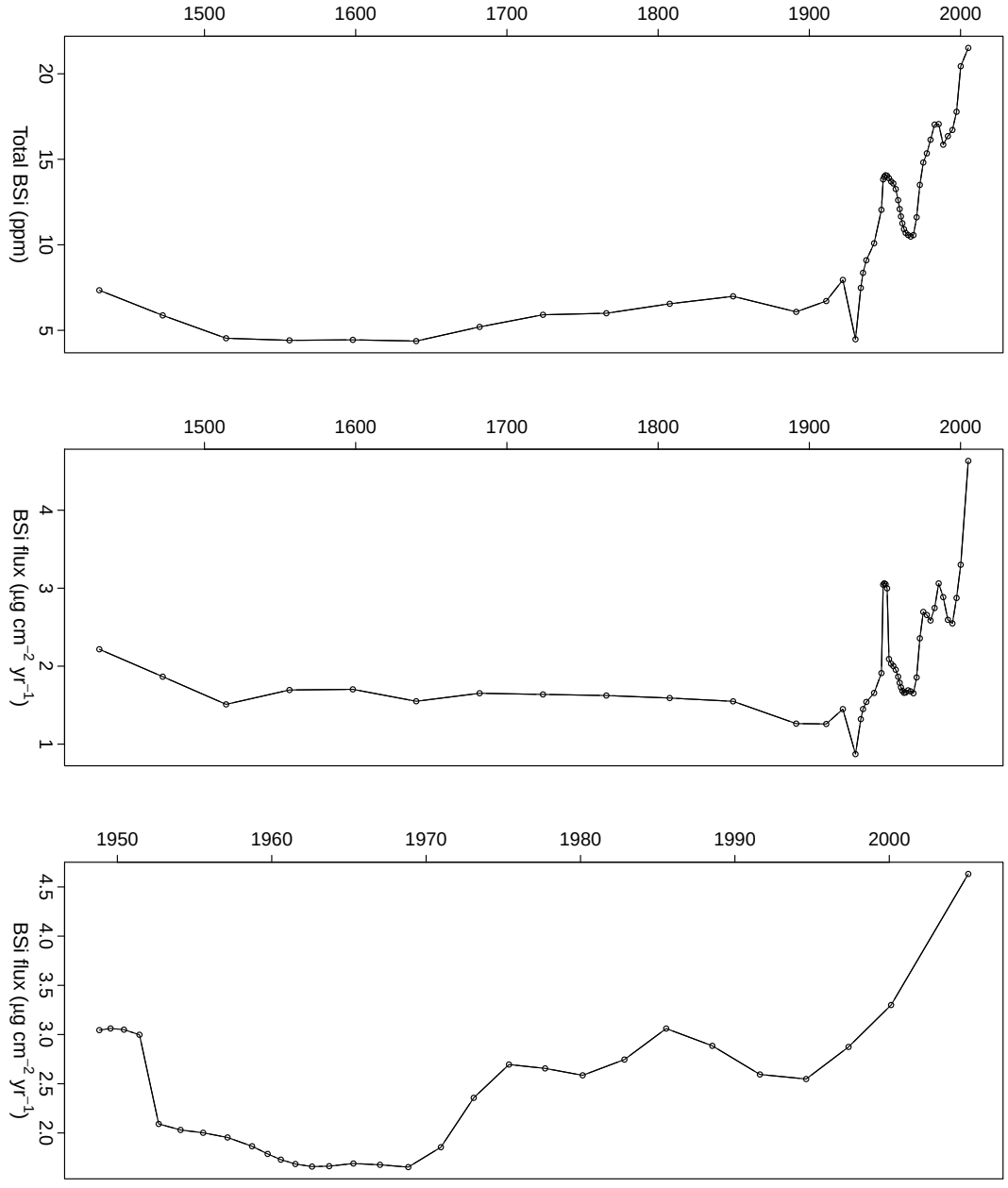

Figure 4.17: Total biogenic silica (top) and biogenic silica flux for the full record (middle) and for the period after AD 1948 (0.2 cm resolution only; bottom). Note the twofold sampling interval of the middle graph.

4.10 Grain Size Analysis

Except for two of the tephra samples, laser beam obscuration of the Malvern Mastersizer never reached the critical values of below 10 % when adding as much of the material as needed and as available. Still, a few measurements showed characteristic signals of air bubbles within the water medium that could not be avoided. The average grain size distribution for all samples is shown in Figure 4.18. The distribution could be approximated by a log-normal distribution (mind the scale of the x-axis), but showed some irregularities from this optimum. It suggested secondary maxima at around 9 μm and 240 μm. A bimodal distribution could indeed be seen for most of the samples in between 3 cm and 8 cm total sediment depth, as it had the primary local maximum at around 40 μm and the secondary maximum at around 8 μm. This was accounted for a probable occurrence of two-fold depositional processes that may have been due to e.g. differences in the sedimentation characteristics between the summer and winter seasons. What could not continuously be seen was the peak at 240 μm, as this was a product of the measurement error mentioned above. Furthermore, there was a marginal tendency to a stronger left tale of the distribution as indicated by the skewness parameter (see next paragraph) and by the negative offset of the median relative to the mean grain size (see Figure 4.18).

Figure 4.20 depicts three of the summary statistics from the grain size distribution for all measurements. The overall trend in mean grain size decreased dramatically from about AD 1550 till AD 1910. Despite of more pronounced fluctuations becoming visible in the high resolution segment, this trend seemed to continue till present. The simultaneous decrease of the median, on the other hand, was much lower until AD 1910, but then dropped rapidly to values much below the mean. This was partially explained by the instantaneous decrease of the negative skewness of the logarithmic distribution. The skew of the grain size distribution was negative for the entire set of samples. This indicated presence of small-grained particles independent of the grain size mean. The results of the grain size analysis are compared with climate parameters in the section below. The grain size distribution of the tephra samples (illustrated in Figure 4.19) is discussed in section 4.6.2.

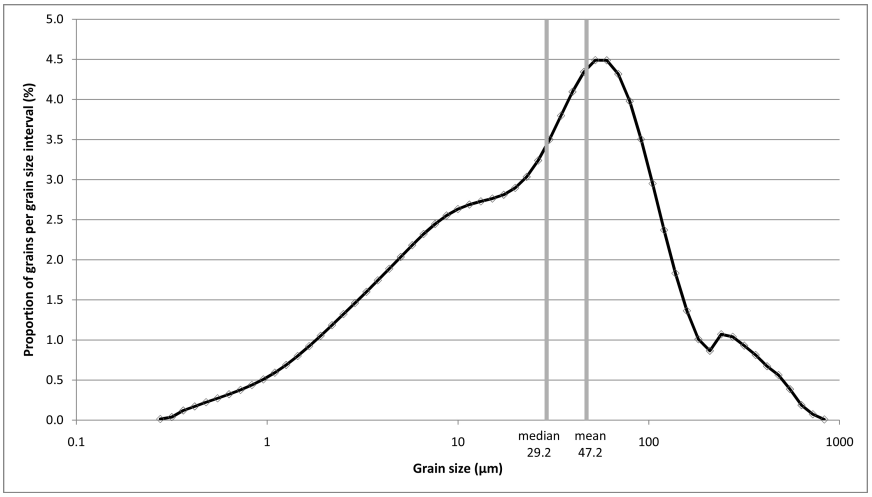

Figure 4.18: Average grain size distribution of all samples from CAS-09-1A and CAS-09-1B. Mean and mode of the distribution are indicated. The y-axis represents the proportions of grains that have a grain size diameter within an interval that increases exponentially with grain size.

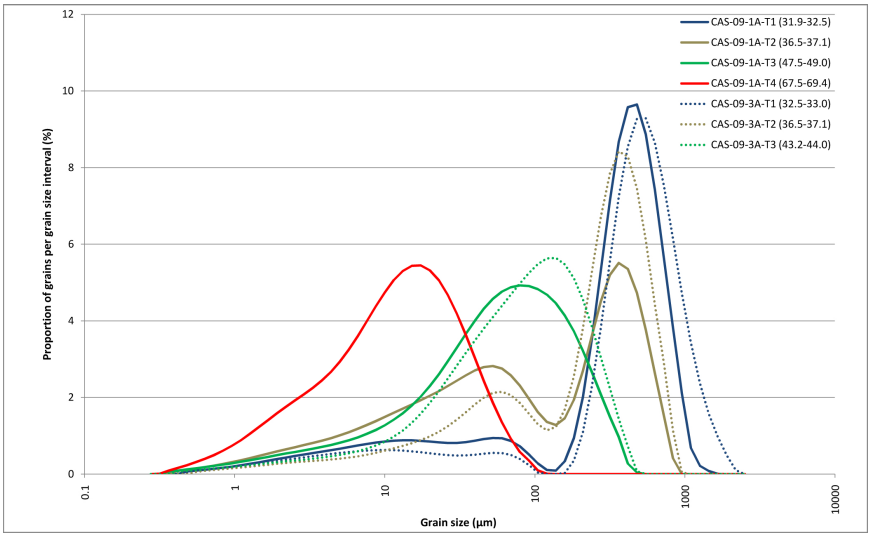

Figure 4.19: Grain size distribution of all tephra samples from CAS-09-1 and CAS-09-3. The y-axis represents the proportions of grains that have a grain size diameter within an interval that increases exponentially with grain size.

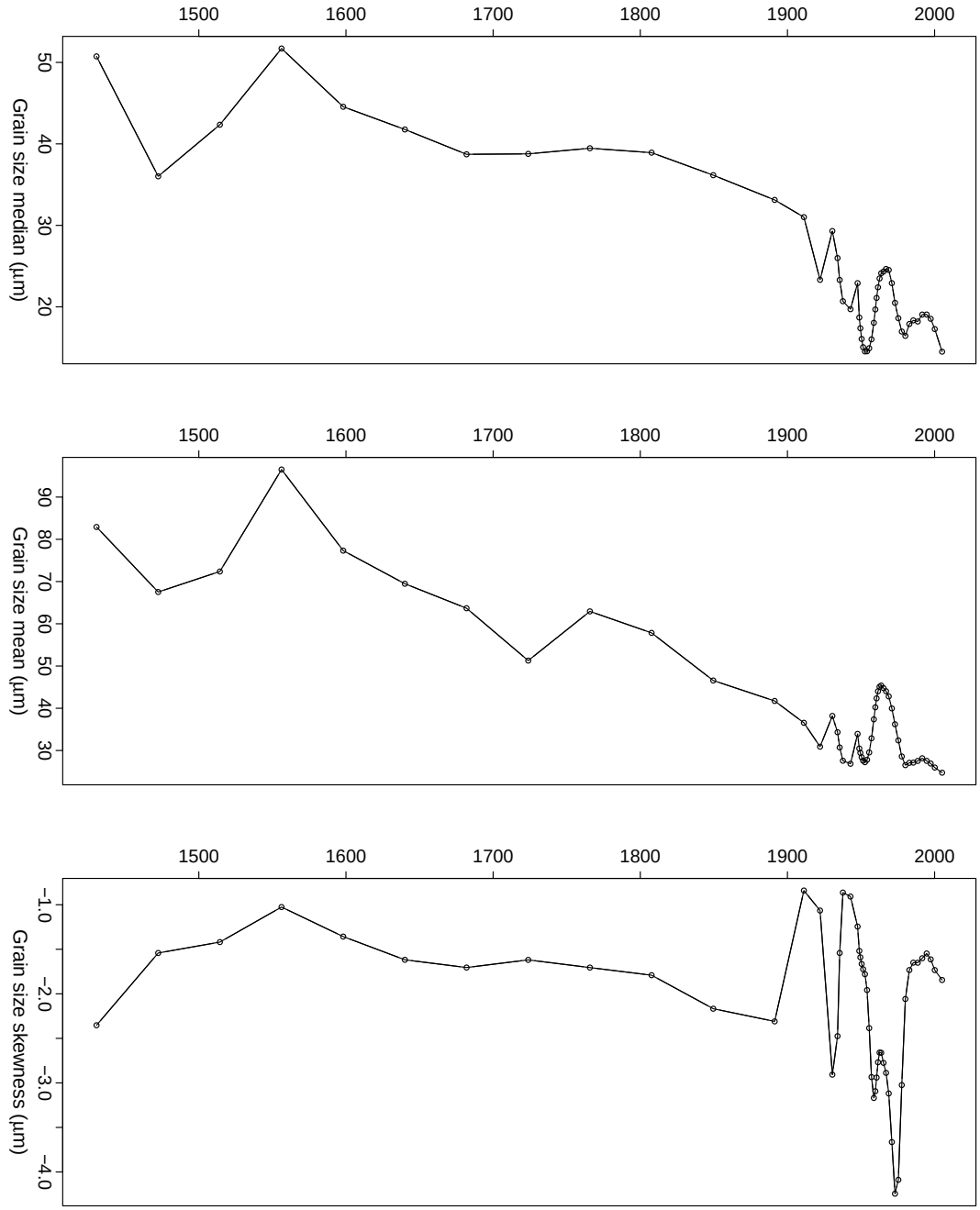

Figure 4.20: Choice of summary statistics of all grain size distributions plotted over time. Note the twofold sampling interval.

4.11 Environmental Conditions

This section summarizes and aggregates the results from all methods to reach to a final conclusion regarding the first research question given at the beginning of chapter 1. A special focus is on parameters that comprise valuable information on environmental or climatic conditions apart from the volcanic history that is discussed in the next chapter. Section 5.3 compares the results with the findings from studies introduced in section 1.2.

The answer to research question 1 could be provided in a level of accuracy that was slightly constrained by uncertainties arising from both the characteristics of the archive and the proxies as well as from errors introduced by each method. To account for the bigger part of uncertainty, the corresponding error estimates of each parameter were included into the presentation and discussion of the results. Each parameter was regarded as having horizontal error bars representing the uncertainty introduced from the age model (see 4.6), and vertical error bars representing the uncertainty introduced by the procedures accomplished to measure and calculate each proxy. The method-related error was generally smaller than the error based on the age model. For the destructive methods, additional uncertainty was introduced by sampling uncertainty. On the other hand, the adjustment of the adjusted t-test statistic for removal of autocorrelation from the time series compensated for most of these errors (see section 3.13). Yet, the errors have to be kept in mind for the concluding remarks.

Before the correlation between single parameters was assessed, a PCA was applied on each dataset in uniform resolution. In all cases except for the 0.05 cm resolved XRF data, the variables had to be regrouped into separate matrices of smaller dimensions in order to allow the computation of principal components (which requires a higher or equal number of observations than parameters). Except for the XRF dataset, the analysis lead to the identification of only one component representing almost the entire variability. As the second principal component of the primary analysis was based on all non-XRF variables as well as on the XRF ratios, those variables were removed and the PCA was repeated with a dataset of the element concentrations (counts) alone. Now the second component of the PCA of the XRF data showed a proportion of explained variance of 9.4 %

(first component: 87.2 %). The biplot in Figure 4.21 illustrates this result by showing a subset of 17 variables that have the highest loadings and are hence closest to the PC axes. The first PC (horizontal axis) was mainly explained by elements such as iron, molybdenum, calcium, or zinc, whereas the second component (vertical axis) was mainly explained by the elements rubidium, silicon, zirconium, potassium, aluminium, and barium. This information was used as an indicator for the detection of interrelations between the elements that were caused by various environmental processes.

The Shapiro-Wilk test for normality revealed a high number of not-normally distributed parameters which required the application of nonparametric statistics for an assessment of their correlation. For this reason, the Spearman rank correlation coefficient was calculated instead of the Pearson correlation coefficient. A number of significant correlations were detected. Next to those correlations between parameters whose close relation was obvious or not of interest (e.g. mean grain size versus median grain size), a smaller number of correlations were detected that assisted in finding an answer to both research questions.

Table A.6 (page 126 in the appendix) lists correlation coefficients between climate parameters from Table 3.5 and a selection of measurement variables with a potential dependency on the climate variables. The t-test statistic is shown in the right column. Significant correlation coefficients at the 80 % and at the 90 % level are highlighted as described in the Table heading. Significance was determined according to section 3.13.

The measured proxies showed a number of significant correlations with climate parameters. In accordance to the limited resolution of the measured data, the chosen subset of climate parameters was limited to annual means in temperature, annual precipitation sums, austral summer and winter temperature means and precipitation sums, as well as to the indices SAM, PDO, and MEI (cf. Table 3.5, page 48). The climate variables are at the same temporal resolution as the measured proxies, as it was shown in section 3.12. As expected, temperature and precipitation were interlinked (negative Pearson correlation coefficient of -0.4), and hence a positive correlation with one of these parameters may have induced a negative correlation with the other parameter. The detected correlations from Table A.6 are synthesized in the following paragraphs.

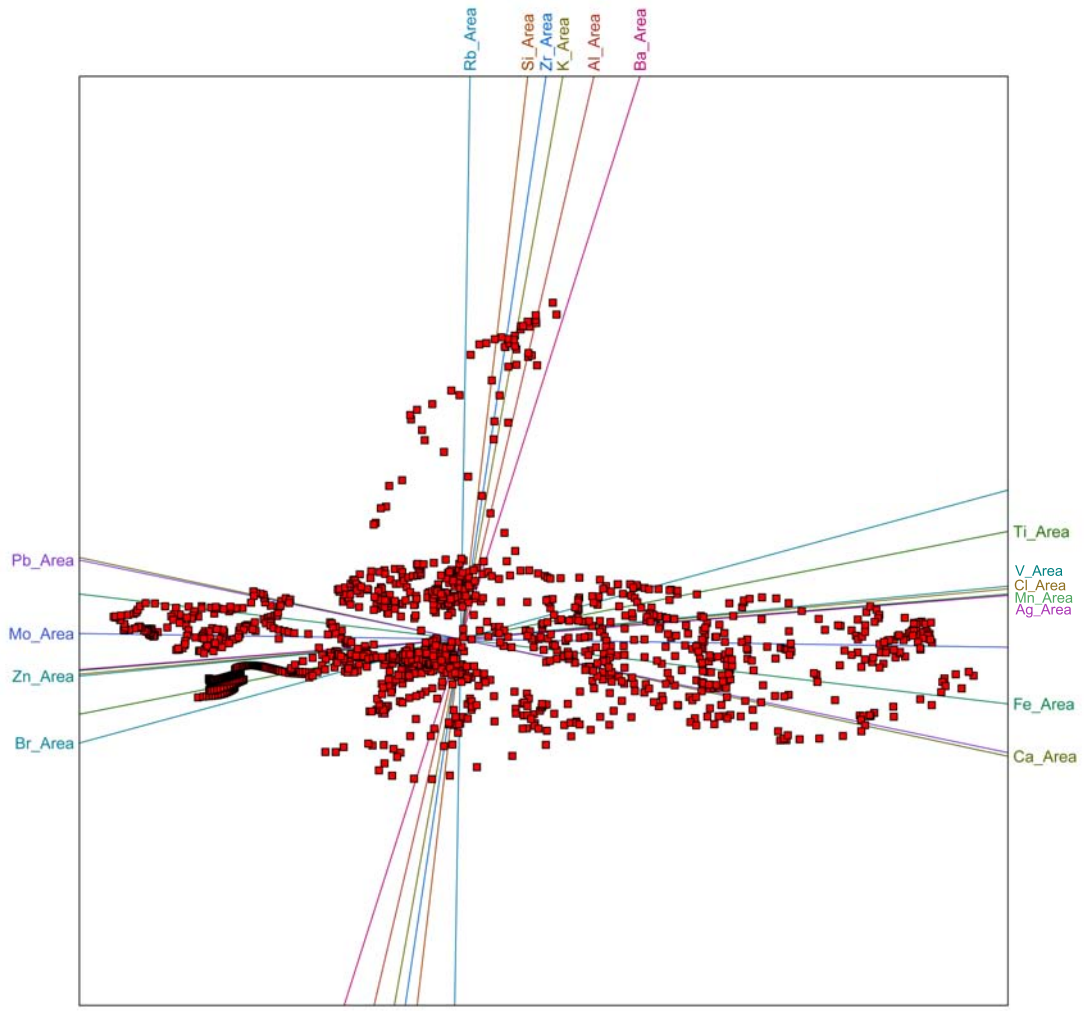

Figure 4.21: Biplot of the first two components of a PCA for a subset of variables from the XRF dataset. 87 % of the variance is explained by component 1 (horizontal axis), 9 % is explained by component 2 (vertical axis).

From the XRF scan data, the indicators for pedogenic sediment input were selected, as the intensity of pedogenic input per unit time is physically linked to the amount and intensity of precipitation. Evidently, these parameters were significantly correlated with both T and P, but only the Ca/Fe and Al/Ti ratios showed significant positive correlations of above 0.4 with (annual) precipitation. This underlined the dependency of pedogenic input on precipitation sums. On the other hand, the weak but significant anticorrelations between P and Mn/Fe or Al/Fe suggested that those ratios are not valid indicators for pedogenic sediment input for Lago Cástor. Furthermore, the Ca/Ti ratio was negatively correlated with annual temperature, which demonstrates the anticorrelation between T and P. Strong significant correlations with the climate indices were not found.

The biogenic silica flux was expected to be correlated with temperature, as a temperature increase generally affects lake productivity. For mean grain size, a positive relation to (particularly extreme) precipitation was expected. The correlations with T and P did indeed support these theories, again demonstrating the anticorrelation between those climate parameters (see Figures 4.22 and 4.23 for a visualization of these examples). The climate indices were positively correlated to BSi flux, but negatively to mean grain size. Surprisingly, the t-test revealed only low values for the significance of all of the correlations, claiming that none of them is significant at the 80 % level. This was caused by the small number of observations for which both datasets were available (N=30 for T, N=29 for P). But as the correlation coefficients were still high for both T and P, these results were not discarded from the discussion. In accordance to the changing sign between the correlations of T and P with BSi flux compared to the correlation with mean grain size, the sign of the (insignificant) correlations also changed in the expected manner, indicating that both proxies are indeed valid for the reconstruction of temperature and precipitation signals in the catchment. But as for the lack of significance, this relation could not be substantiated.

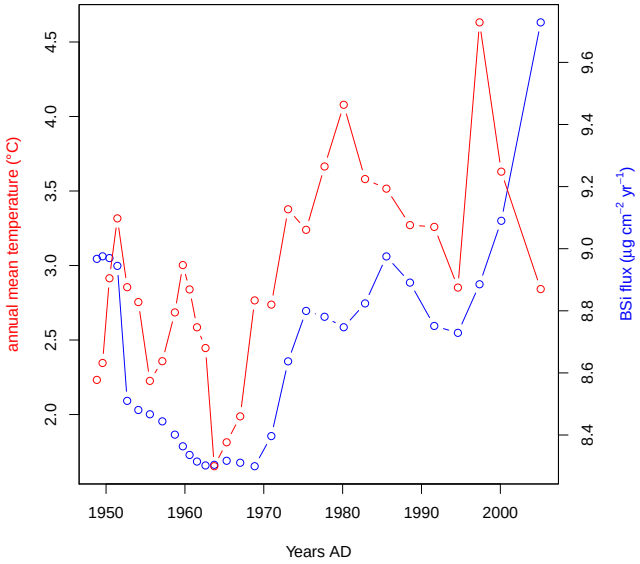

Figure 4.22: Biogenic silica versus temperature for the same time span.

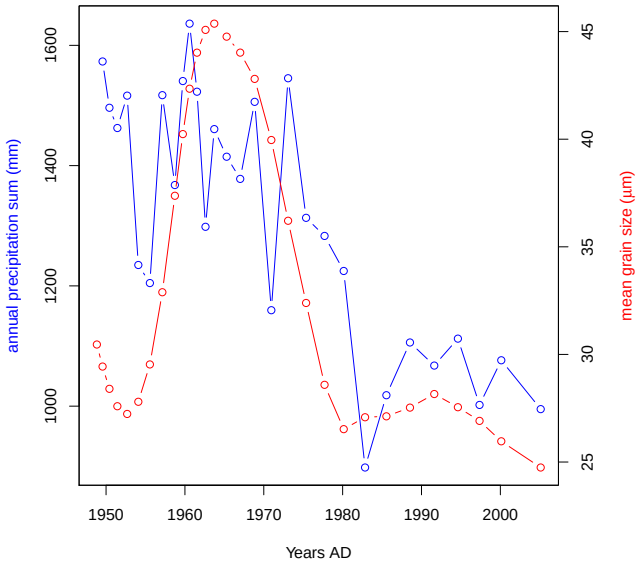

Figure 4.23: Mean grain size versus precipitation for the same time span.

The C/N ratio is not expected to correlate with climate parameters, but may still depend on them indirectly, assuming that high concentrations of algae (accompanied by high nitrogen production) depends to some extent on temperature. Hence, under the assumption of a constant input of terrestrial carbon, high nitrogen concentrations (i.e. low C/N ratios) would imply high temperatures. But as the measured carbon concentrations varied substantially over time, this relationship might have been masked. This may have caused the low correlation of C/N with both T and P. The t-statistic seemed to be an inappropriate measure for this specific parameter, as it even claimed significance for the weak correlation coefficients. Being of particular interest for the discussion of the land use change history (section 5.3.2), the C/N ratio was compared to the flux in biogenic silica during the high resolution time span of the flux (Figure 4.24). In contrast to T and P, the correlation to the SAM index was significant, although the significance was probably overestimated.

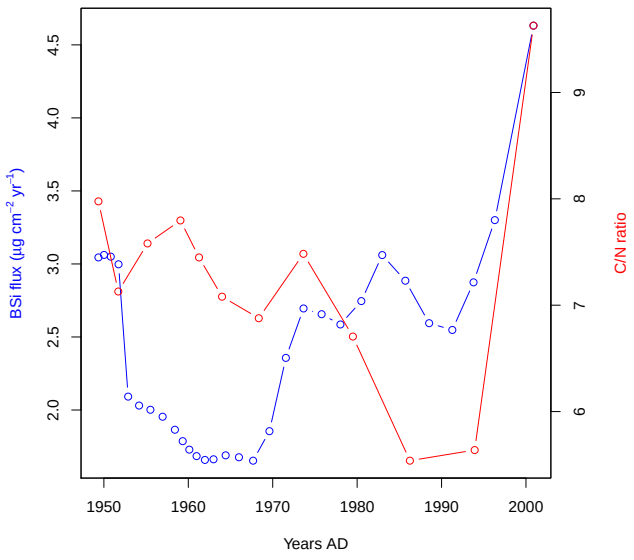

Figure 4.24: Biogenic silica flux versus C/N ratio for the same time span. Note that BSi flux is at 0.2 cm resolution and the C/N ratio at 0.5 cm resolution.

As expected from the considerations above, carbon flux correlated significantly positively with temperature. Austral summer (DJF) T clearly dominated over the correlation between organic carbon flux and austral winter (JJA) T, suggesting a strong link between temperature and plant growth and decay. However, the negative correlation with precipitation is a little surprising, as high precipitation would facilitate transport of terrestrial carbon to the lake. Nitrogen flux acted as expected and increased with temperature, and (due to the negative T-P relation) dropped with a precipitation increase. As for the C/N ratio and the carbon flux, the significant correlation of the nitrogen flux with the SAM index was most likely a product of chance.

Apart from the climate signals, some of the investigated proxies did also show indications primarily related to land use change. The stratigraphy as presented in 4.2 revealed the numerous impacts of volcanic eruptions on the lake (see discussion in section 5.1). Those impacts probably had a strong impact on the environmental conditions of the lake and its catchment for several years to decades, and to a minor extent probably even until today. Apart from "pollutants" of semi-natural origin (namely zinc), detectable pollutants of anthropogenic sources were absent (see 4.4). The redox conditions showed an abrupt increase within the last decades, potentially linked to changes in the pH level that was potentially affected by land use (see discussion in section 5.3.2). Another peak in redox conditions was found around 1300 B.C., the origin of which is most likely controlled by climate rather than by human impact. The weathering indicators were supposedly not indicating the corresponding processes, as weathering at detectable levels usually requires time scales too long to allow a weathering signal to be incorporated into the surficial lake sediments. Likewise, the validity of the proxies for pedogenic sediment input were not applicable in the lake. Their partial linkage to temperature and precipitation was shown above. The numerous peaks in the total chlorine proxy suggested a low quality of the proxy for the studied lake. For the time before AD 1900, both proxies for lithogenic content and degree of diagenesis showed only marginal trends but high variability at certain depths. The suggested drop in lithogenic content over the last centuries may have been related to the decrease in the degree of diagenesis near the sediment-water interface. But a link to a simultaneous increase in organic matter concentration seemed probable as well, as suggested by the strong increase in the organic carbon flux near the sediment-

water interface (Figure 4.16). Anyway, the carbon flux strongly supported the inapplicability of bromine (determined by the XRF scan, see Figure 4.11) as an indicator for OM, as the trends and variability between both series don't show any similarities. The rapid increase in biogenic silica over the last century may not be related to climate change alone, but may also be driven by a major change in land use during that period (see 5.3.2). The near-constant flux for the time before AD 1900 may have been due to stable (probably undisturbed) conditions in land use. The same was indicated by the grain size parameters, although the mean and median claimed that the transport of coarse grained material steadily decreased from AD 1560 till AD 1900.

5. Discussion

This chapter discusses the results with respect to the second research question. The aim of the discussion is to relate the results to historical records of land use change, and to assess the quality of the paleoclimate proxies by correlating them with climate datasets. Next to these goals, the age model and the tephrochronology are discussed, leading to the results as presented in the previous chapter.

5.1 Tephrochronology

In this section, the composition of the sampled tephra layers is compared to published reference data as outlined in the introduction (section 1.2.1). The potential tephra deposits that may be located at the study site were introduced there either. Before going into details, an estimation of the measurement uncertainties is provided.

As the differences between the first and second set of glass pills was very small, uncertainty introduced from sampling, pretreatment and measurement was negligible. The measuring accuracy was very high, as the sum of all measured element proportions was close to 100 % (cf. Table A.5). The major part of uncertainty was likely introduced from the nature of the tephra deposits themselves, or by a lack of accuracy in the depth at which the eruptive material was deposited. As the sediment cores contained more potential tephra layers (facies 1 + 2 in Figure 4.1) than the number of known volcanic eruptions with impact on the study site over the last 4000 years, the blurry dark-coloured layers (facies 3) could most likely be attributed to redeposited tephra material (cf. 3.5.1.2). Under this assumption, the actual sedimentation rate within the lower part of the sediment

record would have been considerably lower than the one assumed from the continuous age-depth model (see Figure 4.6). But as no flux parameter (except for the mass accumulation rate) went beyond the uppermost occurrence of facies 1 or 2, an exclusion of these facies from the age model was not required to gain correct flux values for the entire core. In case a calibration of the paleoenvironmental proxies was applied in future studies, the additional age model would have to be calculated beforehand.

Direct comparison of the semiquantitative XRF element counts with data from Naranjo & Stern 1998, Naranjo & Stern 2004, and Markgraf et al. 2003 revealed the following results. The lowest tephra deposit (CAS-09-1A-T4 (67.5–69.4 cm)) was analysed first. When setting the sum of the proportions of Rb, Sr, Zr and Y (Table A.5) to 100 %, the relative amounts of these elements were in proximity to the average composition of the Hudson H2 tephra Markgraf et al. 2003. Details are given in Table 5.1, clearly demonstrating that all tephra deposits other than CAS-09-1A-T4 (67.5–69.4 cm) are very different to the one presented in the mentioned publication. In Markgraf et al. 2003, the H2 tephra was described as having a green colour, which was not true for the colour of the potential tephra layer CAS-09-1A-T4 (67.5–69.4 cm). But as the same deposit was also found in a yellowish-white appearance, and a backward interpolation of the age model solely based on carbon-14 data fit almost perfectly to the calibrated radiocarbon age known for this tephra deposit, the fit of the material from CAS-09-1A-T4 (67.5–69.4 cm) to published tephra compositions was examined in greater detail (see below).

Table 5.1: Comparison of known tephra deposits with all tephra deposits from CAS-09-1. Tephra compositions apart from CAS-09-1A-T4 (67.5–69.4 cm) were added to allow a comparison. Values are given as percentages summing up to 100 %.

data source	Tephra deposit	Rb	Sr	Zr	Y
Patagonian average composition (Markgraf et al. 2003)	H2	9.48	30.72	53.60	6.19
CAS-09-1A-T1 (31.9–32.5 cm)	?	5.93	64.37	27.29	2.41
CAS-09-1A-T2 (36.5–37.1 cm)	?	5.56	60.54	31.97	1.93
CAS-09-1A-T3 (47.5–49.0 cm)	?	6.53	58.14	32.26	3.07
CAS-09-1A-T4 (67.5–69.4 cm)	potentially H2	9.52	21.99	63.32	5.17

The composition of the Macá 1540 BP eruption (Naranjo & Stern 1998) was not found in the available literature. Moreover, when assuming the final age model as given, no potential tephra deposit was found at or around the depth where it was assumed to be (at roughly 15 cm below sediment surface). All other known tephra layers from the beforementioned publications could not be found in the core for reasons of a too old deposition age or a mismatch in the spatial distribution of the deposits.

Comparing the plots from Figure 4.13 (p. 72) with equivalent plots from Gutiérrez et al. 2005 allowed for comparison of known and dated tephra layers with all sampled tephra layers of Lago Cástor at once, by simply adding the data points from 4.13 to those figures (no plotting required). A number of agreements were detected. All diagrams of sample CAS-09-3A-T1 (32.1–33.5 cm) agreed with the typical geochemical composition of tephra deposits attributed to either Cay or Macá eruptions. Considering the age model of CAS-09-1 as given, this tephra deposit would have been present at depth approximately 28 cm below sediment surface. In fact, when comparing this result with the core diagram (Figure 4.1) and Figures 4.7 – 4.12, there was a sedimentary deposit that showed characteristic colour variations, but no clear signature from the XRF scan results. As the upper and lower boundaries of this deposit were also very vague, it was not sampled and the extra age information was not incorporated into the model.

The attribution of the samples CAS-09-3A-T2 (36.1–37.4 cm), CAS-09-3A-T3 (43.0–44.1 cm), and CAS-09-1A-T1 (31.7–33.3 cm) was not straightforward for most of the diagrams of Gutiérrez et al. 2005, mainly as a cause of the intermediate position of the element ratios in between tephra originating from Hudson eruptions and material from a Macá eruption. One distinct exception was the $K_2O + Na_2O$ over SiO_2 diagram (Gutiérrez et al. 2005), which undoubtedly related this tephra composition to the Hudson volcano. Unfortunately, no tephra layer from this volcano was known that was younger than H2 and located at the study site (Naranjo & Stern 1998, Stern et al. 2007). The samples CAS-09-1A-T2 (35.7–37.6 cm) and CAS-09-1A-T3 (47.5–49.7 cm) were both very ambiguous as they showed characteristics of both the Macá and Hudson tephra. Hence, these tephra deposits could not be used as chronomarkers. The lowermost tephra CAS-09-1A-T4 (67.5–69.5 cm) showed some misfits (e.g. for TiO_2), but on the

other hand a very good correspondence for the K_2O composition, classifying the material as "High K dacite" (Gutiérrez et al. 2005). The match was strongly supported by comparing the element composition of this tephra (Table A.5) with the data from Table 2 in Naranjo & Stern 1998. The only variations to the span of composition given in this Table were negligibly small. Accordingly, the tephra layer CAS-09-1A-T4 (67.5–69.4 cm) was attributed to the Hudson H2 eruption, allowing the carbon-14 age model to be extended. The uncalibrated age of this eruption (3583 ± 88 yr BP) was calibrated to 3903 ± 171 cal. yr BP by using the same approach as presented in 5.2.1.

5.2 Dating

5.2.1 Carbon-14 Age Model

As the confidence intervals of the ages of both samples CAS-09-1A-bulk (60.5 cm) and CAS-09-1A-macro (60.5 cm) showed a clear overlap, the corresponding ages were considered as equal (see Figure 4.3 on page 59). In addition, presence of carbonates in the sediments was ruled out by the HCl test (cf. 3.4). This indicated there were no reservoir effects in the catchment.

SHCal04 was used to calibrate the radiocarbon ages. For each uncalibrated year, the OxCal calibration tool was used to determine intervals for which the probability that the uncalibrated year corresponded to one of the calibrated years within the interval was as high as 64 %. The corresponding standard deviations of the chosen intervals were added to the uncertainty estimates of the uncalibrated ages. In cases where the OxCal tool determined more than one interval (having a fraction of the total probability of 64 %), the one with the highest probability was selected. The mean value of the chosen interval was then chosen as the corresponding calibrated age. Due to the sparse number of dated samples, linear interpolation was applied to connect the points of each age-depth pair. The calibrated ages including their corresponding error intervals were then exported to an MS Excel® spreadsheet and later combined with the age model from the lead-dated core segment (cf. section 4.5).

5.2.2 Lead-210 Age Model

The fraction of supported lead-210 could not be undoubtedly determined from the first set of samples. The radium-226 activity was below detection limit for all samples, but the corresponding activity of supported ^{210}Pb did not reach the expected activity of 0 $Bq\,kg^{-1}$ for the lowest sample (sample No. 22 in Table A.2 on page 120). This activity was detected for the first of the additional measurements (No. 42 at depth of 20.75 cm), proving that the measured total ^{210}Pb activity was indeed equal to the unsupported fraction. This lead to the conclusion that no supported lead-210 radiation developed in the particular geologic environment of the catchment (cf. 2.2), but that sources of unsupported lead-210 still existed in nearby geologic environments and soils. The anomalous result of the second additional sample (No. 44 in Table A.2) was discarded, as it was marked as having been caused by a defective measurement by the Eawag laboratory. As the results from both extra measurements (No. 43 and No. 42) suggested the initial concentration of unsupported ^{210}Pb to be located in between 12 and 20 cm depth, the range from 0 cm to 10.75 cm below sediment surface was finally chosen as a data base for the age model.

As the core segment relevant for lead-210 dating contained no obvious turbidites and no tephra layers, no sediment layers needed to be excluded. Gaps in the series of original measurements of total ^{210}Pb activity as visible in the lack of data points for specific depths in Table A.2 were filled with linearly interpolated ^{210}Pb activity at 0.5 cm resolution from the two closest records from above and below the corresponding gap. Measurements of ^{210}Pb activity below detection limit at depth of 2.75 cm, 5.75 cm, and 7.75 cm (Table A.2) were treated equally after a test of all age models with a simulated radioactive activity of 0.001 Bq/kg at these depths lead to a very uneven shape of the age-depth curves.

Constraining the CRS model with the AD 1964$\pm$ 1 ^{137}Cs peak was not straightforward. As the peak was very broad and diffuse, it was assumed to be within the range of 1.5 cm to 3.5 cm total sediment depth. Using both the shape of the age-depth relation in reference to the carbon-14 model and the standard deviations from each model as evaluators, the best model was chosen (see 4.5). As SCPs were absent in the catchment, no chronomarker could be inferred from these counts to further constrain the age model.

5.3 Results in Context with other Studies

This section puts the results from chapter 4 in context with the local to regional climate history of the wider study area, and with documentary records of land use change in the Aysén region. The tephrochronology is excluded from this discussion (see section 5.1).

5.3.1 Climate

As suggested from the correlation analysis, the C/N ratio was related to temperature and precipitation. The high values from AD 300 to AD 700 (4.16) were presumably due to an unknown phase of above-average temperatures and / or below-average precipitation, which contrasts to the cold fluctuation suggested by Boninsegna et al. 2009. The extremely low values shortly before and during the AD 1000 – AD 1100 period may be a late effect of the cold and moist period spanning the time AD 900 – AD 1070 (cf. Figure 1.2). This period ended with the C/N peak in AD 1100. After that, both fluxes remained on a very low and semi-constant level, suggesting stable climate conditions or overriding influence of non-climatic effects. The latter seemed more likely, as the corresponding period was characterized by numerous temperature and moisture fluctuations (e.g. Boninsegna et al. 2009).

The actual paleoclimate proxies (biogenic silica and mean grain size) were expected to show a better performance than the indirect C/N proxy, although they were not significantly correlated to temperature and precipitation (cf. 4.11). The long-lasting cold period from AD 1270 to AD 1670 was not visible in the records, probably due to the very low resolution of the measured parameters at that time. The same was true for all other characteristic climate deviations before AD 1900 (see Figure 1.2). The sharp increase in the flux since around AD 1920 coincided with the beginning of the overall modern warming trend in Southern South America since AD 1900 or AD 1940. The trough from AD 1955 – AD 1970 (Figure 4.22) may have been due to slightly lower temperatures. Similarly, the reincrease of the BSi flux in AD 1970 could be explained by the temperature peak around AD 1980 that occurred in parallel to the drop in precipitation.

Only the AD 1976 climate shift was not found in the records. Either the age model caused the misfit (i.e. the AD 1971 BSi increase was related to the shift), or the amplitude of the shift was too small to be noticed. Indeed, a misfit of the model is beyond question for this specific case, as the reanalysis dataset showed no shift to warmer temperatures in AD 1976 either, suggesting that - at least with concern to temperature - the shift was not present in AD 1976.

The prolonged cold and moist period from AD 1270 – AD 1670 was not supported by the records of mean and medium grain size, also due to the very low temporal resolution of the parameters at that time. Anyhow, the high mean does not prove opposite climatic conditions. The AD 1720 – AD 1790 warm period (Figure 1.2) might be indicated by the lower grain size at around the onset of this period, suggesting below-average precipitation at that time. The short cold deviation around AD 1800 and the warm period AD 1850 – AD 1890 were not in contrast to the records, but an actual proof for them was not found. In contrast to temperature, the AD 1976 climate shift was visible in the records. The decrease in mean grain size indicates a trend towards less precipitation or at least a trend towards less extreme precipitation events at that time. The instrumental data supports this trend with only a few years offset. A further decrease in precipitation was not visible in the records, as both reanalysis data and mean grain size remained on a relatively stable level.

Parameters from the XRF scan did not show very promising signals of temperature or precipitation on the long term. The correlation of the proxies for pedogenic sediment with both climate variables seemed to be valid for the topmost part of the records only. The ratios of the in-situ reflectance spectroscopy were not correlated to climate parameters either. The increasing redox potential (Mn/Fe proxy) during the 20^{th} century underlined the general trend towards higher temperatures (see Figure 4.8). However, this proxy may also have been controlled by other parameters such as OM decomposition rates and hence oxygen availability.

5.3.2 Land Use Change

For the most part, the C/N data fit well to documented records of land use history (see discussion in 1.2.3). No increase in terrestrial carbon was seen from the beginning of the measurement series until AD 1800 (Figure 4.16). This is not unexpected, as the advent of colonization of this remote region was registered not before the end of the 19th century. The positive anomalies during this early period may have indicated cycles of natural forest fires, each followed by an episode of dominant aquatic productivity, that was probably accompanied by forest regrowth and decreasing soil erodibility. Still, an influence of the redeposited tephra (facies 3) could not be ruled out. Before the onset of large-scale forest burning, the C/N ratio showed an increase during the early 19th century. As this signature was rather weak, it was likely caused by climatic variations (e.g. by an increase in P) rather than by the onset of extensive anthropogenic forest burning. However, forest clearance or burning was obviously initiated by the early 20th century at the latest. The drop in the C/N ratio from values of above 10 at the beginning of the 20th century to values of below 6 in the 1990s indicates stabilizing conditions in the catchment, as it would have been favoured by early forest clearance and a rapid regrowth of the forest (see 3.9). As indicated by the dramatic increase in variability of the mean grain size and skewness over the last century, and as suggested by the higher sedimentation rates seen in the lead-210 age model (Figure 4.5), forest regrowth including afforestation did not lead to entirely stable conditions in the catchment. A clear evidence for this fact are the modern conditions of the catchment (see Figure 2.1 on page 12).

The early decrease in C/N at the beginning of the 20th century suggested that human impact on Lago Cástor was initiated sooner than stated by the literature (AD 1936), or that natural processes, like e.g. a natural increase in fire frequency, were involved. This hypothesis is supported by the above-average temperatures and below-average precipitation at that time (Boninsegna et al. 2009, see Figure 1.2 on page 7). As visible in Figure 4.24 (p. 87), the C/N ratio is (weakly) anticorrelated to biogenic silica flux. This was expected from the diminishing carbon limitation for algal growth by extensive carbon influx from increased erosion, which itself is a late effect of the deforestation (see 3.9). However, the low power of the anticorrelation indicated that intra-lake productivity (as generally

mirrored by biogenic silica concentration) was not the only cause for the drop in the C/N ratio. Obviously, the influx of carbon itself also contributed to the 20th century fall in the ratio, as suggested by the slight decrease after its maximum at the end of the 19th century (see Figure 4.16). Neither the C/N ratio, nor biogenic silica flux showed a reaction at the time of the official end of the intense forest burning period in AD 1956, but a signal was found with a delay of roughly 14 years. The increase in biogenic silica began around AD 1970, quickly followed by a drop in the C/N ratio. This delay was likely due to a prolonged period of cattle farming and a high level of erosion, followed by a rapid stabilization at around AD 1980 (decrease in terrestrial carbon influx), that has most likely been enhanced by afforestation initiatives in the Lago Cástor catchment since the late 20th century (cf. 1.2.3). The potential reasons for the rapid increase of the carbon and nitrogen flux forcing an equal reaction of C/N could not be explained solely by land use change (see section 4.8 in the results chapter).

It has to be kept in mind that temperature plays a major role in aquatic productivity and may be part of the reason for the suggested increase in biogenic silica flux in AD 1970 (see 5.3.1). The link between carbon influx and precipitation or temperature (cf. 4.11) slightly decreased the explanatory power of the C/N ratio as an indicator for land use change. The precipitation decrease over the last 50 years may have lead to a slight additional decrease in erosion rates and hence in terrestrial carbon. The temperature dependency was most likely masked by processes of higher amplitude. Mean grain size was higher during the pre-forest burning period, but it is likely that this is an effect of increased abundance of sand-sized tephra grains with depth (see Figure 4.18). But still, and despite some misfits concerning the timing of the onset of the forest burning period by European settlers, the results from this study reflect the main characteristics of the documented land use history. Equivalently to the affirmation of the human impact on the local forests, the missing documentary evidence for industrial activity was also verified (see 4.4).

6. Conclusions and Outlook

This Thesis gives far-reaching indications of paleoenvironmental conditions of Lago Cástor (North Patagonia) and its catchment, while the results are valid and applicable even beyond these boundaries. The study concentrates on climate and land use change over the period of the last 2000 years, and on the history of volcanic eruptions over the entire time span covered by the lake sediment core of roughly 4000 years, both at decadal to sub-centennial resolution. The results are discussed with respect to findings of other research within Southern South America as well as with records of temperature, precipitation, and a set of climate indices.

An age model was built by using AMS radiocarbon dates and the most valid lead-210 age model. Using X-Ray Fluorescence analysis, at least four volcanic eruption were identified and had an imprint on the lake sediments of Lago Cástor. The characteristics (colour, grain size, and composition) of the lowermost tephra layer in the core matched well to the characteristics of a tephra deposit for which the corresponding eruption age (3903 ± 171 cal. yr BP) was found in the literature. This constraint was used to extend the age model further back in time.

Besides the semiquantitative measurements for application in tephra analysis, X-Ray Fluorescence was also applied to gain qualitative element counts and ratios thereof by scanning one of the lake sediment cores, revealing numerous indicators for paleoenvironmental conditions. Measurements of in-situ reflectance spectroscopy were applied to calculate proxies for total chlorine, lithogenic content, and degree of diagenesis. Biogenic silica flux was measured and found to be a valid proxy for both paleoclimate (temperature) and land use change (productivity increase in case of high terrestrial carbon input). The carbon-to-nitrogen ratio was measured in order to reconstruct past conditions in vegetation cover and

anthropogenic land use. To complement the geochemical proxies, the grain size distribution was measured, and the mean grain size parameter was investigated as a proxy for precipitation and land use change.

The complete data set was filtered with a triangular filter in order to account for uncertainties introduced by minor offsets in sampling or measurement and presumed bioturbation. The data series were analysed with the help of summary statistics, principal component analysis, and analysis of correlation between variables at identical resolution. Although the resolution of the parameters varied, their overall quality was estimated to be high due to a minimization of sampling and measurement errors. The only major drawback in the records is the partly low sampling resolution of the geochemical proxies (cf. Figure 3.1).

The records agree that temperatures increased over the last decades, initiated by a shift in climatic conditions in the 1970s. Grain size measurements coincided with precipitation trends over at least the last century. The carbon-to-nitrogen ratio indicates an early onset of the forest burning period in the Lago Cástor catchment at the beginning of the 20th century. This is earlier than claimed by the literature, but not contrary to the results of the biogenic silica measurements. The results suggests that farming activities lasted as long as AD 1970, rapidly followed by a stabilization very probably driven by afforestation.

The results of this study demonstrate the potential of paleolimnological studies from non-varved lake sediments at medium resolution. Its strength is certainly the wealth of information extracted from the archive even at a resolution below decadal level. The exact timing of environmental events may be hampered by a weak performance (high uncertainty) within the age model, as it partially applies to the lead-210 age model used in this study. The main drawback of this study is still the lack of sufficient highly resolved datasets for the determination of proxies further back in time.

Concerning the valuable results of this study relative to the time span and resolution of proxy records within the same archive, this study provides a good basis for future studies in the field of paleolimnological research in Southern South America. The results highly suggest an extension of the acquired records in both time and space. Further efforts are particularly pressing, as the need of highly resolved quantitative paleoclimatological studies from North Patagonia is

apparently still large. As the limited resolution of the geochemical proxies used within this study is still a major drawback, it is strongly suggested to extend the dataset with records at 0.2 cm resolution downcore. At the same time, the task of calibrating the paleoenvironmental proxies is strongly recommended to be tackled within future studies. Besides, the XRF-derived patterns identified in between the chemical elements of the lake sediments of Lago Cástor can be further assessed. With the exception of the lowermost tephra deposit from core CAS-09-1, it remains an open task of relating the sampled tephra layers to their deposition age.

References

Abarzua, A. M., C. Villagran & P. I. Moreno (2004): "Deglacial and postglacial climate history in east-central Isla Grande de Chiloe, southern Chile (43 degrees S)". In: *Quaternary Research* 62.1, pp. 49–59.

Abbott, M. B. & A. P. Wolfe (2003): "Intensive Pre-Incan Metallurgy Recorded by Lake Sediments from the Bolivian Andes". In: *Science* 301.5641, pp. 1893–1895.

Appleby, P. G. (2001): "Chronostratigraphic techniques in recent sediments". In: *Tracking environmental changes using lake sediments*. Ed. by W. M. Last & J. P. Smol. Vol. 1, pp. 171–203.

Appleby, P. & F. Oldfield (1978): "The calculation of lead-210 dates assuming a constant rate of supply of unsupported 210Pb to the sediment". In: *Catena* 5.1, pp. 1–8.

Aravena, J. & B. Luckman (2009): "Spatio-temporal rainfall patterns in Southern South America". In: *International Journal of Climatology* 29.14, pp. 2106–2120.

Armesto, J., D. Manuschevich, A. Mora, C. Smith-Ramirez, R. Rozzi, A. Abarzúa & P. Marquet (2010): "From the Holocene to the Anthropocene: A historical framework for land cover change in southwestern South America in the past 15,000 years". In: *Land Use Policy* 27.2, pp. 148–160.

Barker, P., R. Telford, O. Merdaci, D. Williamson, M. Taieb, A. Vincens & E. Gibert (2000): "The sensitivity of a Tanzanian crater lake to catastrophic tephra input and four millennia of climate change". In: *The Holocene* 10.3, pp. 303–310.

Barra, R., M. Cisternas, C. Suarez, A. Araneda, O. Pinones & P. Popp (2004): "PCBs and HCHs in a salt-marsh sediment record from South-Central Chile: use of tsunami signatures and Cs-137 fallout as temporal markers". In: *Chemosphere* 55.7, pp. 965–972.

Beierle, B., S. Lamoureux, J. Cockburn & I. Spooner (2002): "A new method for visualizing sediment particle size distributions". In: *Journal of Paleolimnology* 27.2, pp. 279–283.

Beierle, B. & J. Bond (2002): "Density-induced settling of tephra through organic lakesediments". In: *Journal of Paleolimnology* 28.4, pp. 433–440.

Bennett, K. D., S. G. Haberle & S. H. Lumley (2000): "The last glacial-holocene transition in southern Chile". In: *Science* 290.5490, pp. 325–328.

Bertrand, S., F. Charlet, B. Charlier, V. Renson & N. Fagel (2008a): "Climate variability of southern Chile since the Last Glacial Maximum: a continuous sedimentological record from Lago Puyehue (40 degrees S)". In: *Journal of Paleolimnology* 39.2, pp. 179–195.

Bertrand, S., J. Castiaux & E. Juvigne (2008b): "Tephrostratigraphy of the late glacial and Holocene sediments of Puyehue Lake (Southern Volcanic Zone, Chile, 40 degrees S)". In: *Quaternary Research* 70.3, pp. 343–357.

Björck, S. & B. Wohlfarth (2001): "14 C chronostratigraphic techniques in paleolimnology". In: 1. Ed. by W. M. Last & J. P. Smol, pp. 205–245.

Boninsegna, J. A., J. Argollo, J. C. Aravena, J. Barichivich, D. Christie, M. E. Ferrero, A. Lara, C. Le Quesne, B. H. Luckman, M. Masiokas, M. Morales, J. M. Oliveira, F. Roig, A. Srur & R. Villalba (2009): "Dendroclimatological reconstructions in South America: A review". In: *Palaeogeography, Palaeoclimatology, Palaeoecology* 281.3-4, pp. 210–228.

Bown, F. & A. Rivera (2007): "Climate changes and recent glacier behaviour in the Chilean Lake District". In: *Global and Planetary Change* 59.1-4, pp. 79–86.

Clapperton, C. (1994): "The quaternary glaciation of Chile: a review". In: *Revista Chilena de Historia Natural* 67, pp. 369–383.

Cohen, A. (2003): *Paleolimnology: the history and evolution of lake systems*. Oxford University Press, USA.

Compagnucci, R. & D. Araneo (2007): "Alcances de El Niño como predictor del caudal de los ríos andinos argentinos". In: *Ingenieria Hidraulica En Mexico* 22.3, pp. 23–35.

Conley, D. J. (1998): "An interlaboratory comparison for the measurement of biogenic silica in sediments". In: *Marine Chemistry* 63.1-2, pp. 39 –48.

Conley, D. & C. Schelske (2001): "Biogenic Silica". In: *Tracking environmental change using lake sediments*. Ed. by W. M. Last & J. P. Smol. Vol. 1. Springer, pp. 281–293.

Cortese, G., R. Gersonde, C. Hillenbrand & G. Kuhn (2004): "Opal sedimentation shifts in the World Ocean over the last 15 Myr". In: *Earth and planetary science letters* 224.3-4, pp. 509–527.

Das, B., R. D. Vinebrooke, A. Sanchez-Azofeifa, B. Rivard & A. P. Wolfe (2005): "Inferring sedimentary chlorophyll concentrations with reflectance spectroscopy: a novel approach to reconstructing historical changes in the trophic status of mountain lakes". In: *Canadian Journal of Fisheries and Aquatic Sciences* 62.5, pp. 1067–1078.

Das, B., R. Nordin & A. Mazumder (2008): "An alternative approach to reconstructing organic matter accumulation with contrasting watershed disturbance histories from lake sediments". In: *Environmental Pollution* 155.1, pp. 117–124.

Departmento de Hidráulica e Ambiente, - (2006): "Deliverables 2.6 & 2.8 - Chile". In: *ECOMANAGE - Integrated Ecological Coastal Zone Management System*. Lisboa, p. 42.

Diaz, M., F. Pedrozo, C. Reynolds & P. Temporetti (2007): "Chemical composition and the nitrogen-regulated trophic state of Patagonian lakes". In: *Limnologica - Ecology and Management of Inland Waters* 37.1, pp. 17–27.

Dijkshoorn, J. A., J. R. M. Huting & P. Tempel (2005): *Update of the 1:5 million Soil and Terrain Database for Latin America and the Caribbean (SOTERLAC; version 2.0)*. Tech. rep. 2005/01. ISRIC - World Soil Information, Wageningen.

Falvey, M. & R. D. Garreaud (2009): "Regional cooling in a warming world: Recent temperature trends in the southeast Pacific and along the west coast of subtropical South America (1979-2006)". In: *Journal of Geophysical Research-Atmospheres* 114.

Folk, R. (1964): "A review of grain-size parameters". In: *Sedimentology* 6.2, pp. 73–93.

Garreaud, R. D. & P. Aceituno (2007): "Atmospheric circulation and climatic variability". In: *The physical geography of South America*. Ed. by T. Veblen, K. Young & A. Orme. New York: Oxford University Press, pp. 45–59.

Garreaud, R. D. & M. Falvey (2009): "The coastal winds off western subtropical South America in future climate scenarios". In: *International Journal of Climatology* 29.4, pp. 543–554.

Garreaud, R. D., M. Vuille, R. Compagnucci & J. Marengo (2009): "Present-day South American climate". In: *Palaeogeography, Palaeoclimatology, Palaeoecology* 281.3-4, pp. 180–195.

Gerritse, R. & R. George (1988): "The role of soil organic matter in the geochemical cycling of chloride and bromide". In: *Journal of Hydrology* 101.1-4, pp. 83–95.

Geyh, M. A., M. Grosjean, L. Nunez & U. Schotterer (1999): "Radiocarbon reservoir effect and the timing of the late-glacial/early Holocene humid phase in the Atacama Desert (Northern Chile)". In: *Quaternary Research* 52.2, pp. 143–153.

Giese, B. S., S. C. Urizar & N. S. Fuckar (2002): "Southern Hemisphere Origins of the 1976 Climate Shift". In: *Geophysical Research Letters* 29.2.

Giesecke, A., A. Capera, I. Leschiutta, E. Migliorini & L. Valverde (2009): "The CERESIS earthquake catalogue and database of the Andean Region: background, characteristics and examples of use". In: *Annals of Geophysics* 47.2-3.

Gillett, N., T. Kell & P. Jones (2006): "Regional climate impacts of the Southern Annular Mode". In: *Geophys. Res. Lett* 33, p. L23704.

Gilli, A., D. Ariztegui, F. S. Anselmetti, J. A. McKenzie, V. Markgraf, I. Hajdas & R. D. McCulloch (2005): "Mid-Holocene strengthening of the Southern westerlies in South America - Sedimentological evidences from Lago Cardiel, Argentina (49 degrees S)". In: *Global and Planetary Change* 49.1-2, pp. 75–93.

Glasser, N. F., S. Harrison, V. Winchester & M. Aniya (2004): "Late Pleistocene and Holocene palaeoclimate and glacier fluctuations in Patagonia". In: *Global and Planetary Change* 43.1-2, pp. 79 –101.

Gutiérrez, F., A. Gioncada, O. González Ferran, A. Lahsen & R. Mazzuoli (2005): "The Hudson Volcano and surrounding monogenetic centres (Chilean Patagonia): An example of volcanism associated with ridge-trench collision environment". In: *Journal of Volcanology and Geothermal Research* 145.3-4, pp. 207–233.

Haberzettl, T., M. Fey, A. Lucke, N. Maidana, C. Mayr, C. Ohlendorf, F. Schabitz, G. H. Schleser, M. Wille & B. Zolitschka (2005): "Climatically induced lake level changes during the last two millennia as reflected in sediments of Laguna Potrok Aike, southern Patagonia (Santa Cruz, Argentina)". In: *Journal of Paleolimnology* 33.3, pp. 283–302.

Hakanson L. & Jansson, M. (2001): *Principles of Lake Sedimentology*. Ed. by W. M. Last & J. P. Smol. Vol. 1.

Haug, G., D. Sigman, R. Tiedemann, T. Pederson & M. Sarnthein (1999): "Onset of permanent stratification in the subarctic Pacific Ocean". In: *Nature* 401.6755, pp. 779–782.

Horne, A. & C. Goldman (1994): *Limnology*. New York: McGraw-Hill.

Iriondo, M. H. (1997): "Models of deposition of loess and loessoids in the upper quaternary of South America". In: *Journal of South American Earth Sciences* 10.1, pp. 71–79.

Ivins, E. R. & T. S. James (2004): "Bedrock response to Llanquihue Holocene and present-day glaciation in southernmost South America". In: *Geophysical Research Letters* 31.24.

Jenny, B., D. Wilhelm & B. L. Valero-Garces (2003): "The Southern Westerlies in Central Chile: Holocene precipitation estimates based on a water balance model for Laguna Aculeo (33 degrees 50 ' S)". In: *Climate Dynamics* 20.2-3, pp. 269–280.

Kendall, M. (1962): *Rank Correlation Methods*. London.

Kilian, R, M Hohner, H Biester, H. Wallrabe-Adams & C. Stern (2003): "Holocene peat and lake sediment tephra record from the southernmost Chilean Andes (53-55 S)". In: *Revista Geologica De Chile* 30, pp. 23–37.

Kitzberger, T. & T. Veblen (2003): "Influences of Climate on Fire in Northern Patagonia, Argentina". In: pp. 296–321.

Koinig, K. A., W. Shotyk, A. F. Lotter, C. Ohlendorf & M. Sturm (2003): "9000 years of geochemical evolution of lithogenic major and trace elements in the sediment of an alpine lake - the role of climate, vegetation, and land-use history". In: *Journal of Paleolimnology* 30.3, pp. 307–320.

Kottek, M., J. Grieser, C. Beck, B. Rudolf & F. Rubel (2006): "World Map of the Koppen-Geiger climate classification updated". In: *Meteorologische Zeitschrift* 15.3, pp. 259–264.

Lamy, F., D. Hebbeln, U. Rohl & G. Wefer (2001): "Holocene rainfall variability in southern Chile: a marine record of latitudinal shifts of the Southern Westerlies". In: *Earth and Planetary Science Letters* 185.3-4, pp. 369–382.

Last, W. (2001): "Textural analysis of lake sediments". In: *Tracking environmental changes using lake sediments*. Ed. by W. M. Last & J. P. Smol. Vol. 1. Springer, pp. 41–81.

Longmore, M. E., B. M. O'Leary & C. W. Rose (1983): "Caesium-137 profiles in the sediments of a partial-meromictic lake on Great Sandy Island (Fraser Island), Queensland, Australia". In: *Hydrobiologia* 103.1, pp. 21–27.

Markgraf, V., C. Whitlock & S. Haberle (2007): "Vegetation and fire history during the last 18,000 cal yr BP in Southern Patagonia: Mallin Pollux, Coyhaique, Province Aisen (45 degrees 41 ' 30"S, 71 degrees 50' 30"W, 640m elevation)". In: *Palaeogeography Palaeoclimatology Palaeoecology* 254.3-4, pp. 492–507.

Markgraf, V., J. P. Bradbury, A. Schwalb, S. J. Burns, C. Stern, D. Ariztegui, A. Gilli, F. S. Anselmetti, S. Stine & N. Maidana (2003): "Holocene palaeoclimates of southern Patagonia: limnological and environmental history of Lago Cardiel, Argentina". In: *The Holocene* 13.4, pp. 581–591.

Masiokas, M. H., A. Rivera, L. E. Espizua, R. Villalba, S. Delgado & J. C. Aravena (2009): "Glacier fluctuations in extratropical South America during the past 1000 years". In: *Palaeogeography, Palaeoclimatology, Palaeoecology* 281.3-4, pp. 242–268.

McCormac, F. G., A. G. Hogg, P. G. Blackwell, C. E. Buck, T. F. G. Higham & P. J. Reimer (2004): "SHCal04 Southern Hemisphere calibration, 0-11.0 cal kyr BP". In: *Radiocarbon* 46.3, pp. 1087–1092.

Meyers, P. (1994): "Preservation of elemental and isotopic source identification of sedimentary organic matter". In: *Chemical Geology* 114.3-4, pp. 289–302.

Meyers, P. & J. Teranes (2001): "Sediment organic matter". In: *Tracking environmental change using lake sediments* 1. Ed. by W. M. Last & J. P. Smol, pp. 239–269.

Moberg, A., D. Sonechkin, K. Holmgren, N. Datsenko & W. Karlén (2005): "Highly variable Northern Hemisphere temperatures reconstructed from low-and high-resolution proxy data". In: *Nature* 433.7026, pp. 613–617.

Montgomery, D., G. Balco & S. Willett (2001): "Climate, tectonics, and the morphology of the Andes". In: *Geology* 29.7, pp. 579–582.

Morales, M., R. Barberena, J. B. Belardi, L. Borrero, V. Cortegoso, V. Durán, A. Guerci, R. Goñi, A. Gil, G. Neme, H. Yacobaccio & M. Zárate (2009): "Reviewing human-environment interactions in arid regions of southern South America during the past 3000 years". In: *Palaeogeography, Palaeoclimatology, Palaeoecology* 281.3-4, pp. 283–295.

Moy, C., P. Moreno, R. Dunbar, M. Kaplan, J. Francois, R. Villalba & T. Haberzettl (2009): "Climate Change in Southern South America During the Last Two Millennia". In: *Past Climate Variability in South America and Surrounding Regions*, pp. 353–393.

Municipalidad de Coihaique, - (2010): *Acerca de Nosotros*. URL: http://www.coyhaique.cl/portalmunicipalidad/somos.php.

Naranjo, J. A. & C. R. Stern (1998): "Holocene explosive activity of Hudson Volcano, southern Andes". In: *Bulletin of Volcanology* 59.4, pp. 291–306.

— (2004): "Holocene tephrochronology of the southernmost part (42 degrees 30' – 45 degrees S) of the Andean Southern Volcanic Zone". In: *Revista Geologica De Chile* 31.2, pp. 225–240.

Neukom, R., J. Luterbacher, R. Villalba, M. Küttel, D. Frank, P. Jones, M. Grosjean, J. Esper, L. Lopez & H. Wanner (2010a): "Multi-centennial summer and winter precipitation variability in southern South America". In: *Geophysical Research Letters* 37.14, p. L14708.

Neukom, R., J. Luterbacher, R. Villalba, M. Küttel, D. Frank, P. Jones, M. Grosjean, H. Wanner, J. Aravena, D. Black, et al. (2010b): "Multiproxy summer and winter surface air temperature field reconstructions for southern South America covering the past centuries". In: *Climate Dynamics*, pp. 1–17.

Neves, R., J. Baretta & M. Mateus (2008): *Perspectives on integrated coastal zone management in South America*. Lisboa (Portugal). In Press.

Niwa, Y., T. Sugai, Y. Saegusa, T. Ogami & E. Sasao (2010): "Use of electrical conductivity to analyze depositional environments: Example of a Holocene delta sequence on the Nobi Plain, central Japan". In: *Quaternary International*.

Ohlendorf, C. & M. Sturm (2008): "A modified method for biogenic silica determination". In: *Journal of Paleolimnology* 39.1, pp. 137–142.

Orihashi, Y, J. Naranjo, A Motoki, H Sumino, D Hirata, R Anma & K Nagao (2004): "Quaternary volcanic activity of Hudson and Lautaro volcanoes, Chilean Patagonia: New constraints from K-Ar ages". In: *Revista Geologica De Chile* 31, pp. 207–224.

Oyarzun, C., C. Aracena, P. Rutherford, R. Godoy & A. Deschrijver (2007): "Effects of land use conversion from native forests to exotic plantations on nitrogen and phosphorus retention in catchments of southern chile". In: *Water Air and Soil Pollution* 179.1-4, pp. 341–350.

Pankhurst, R. J. & F. Hervé (2007): "Introduction and Overview". In: *The Geology of Chile*. Ed. by T. Moreno & W. Gibbons, pp. 1–4.

Parada, M. A., A. Lahsen & C. Palacios (2001): "Ages and geochemistry of Mesozoic-Eocene back-arc volcanic rocks in the Aysen region of the Patagonian Andes, Chile". In: *Revista Geologica De Chile* 28.1, pp. 25–46.

Peel, M., B. Finlayson & T. McMahon (2007): "Updated world map of the Köppen-Geiger climate classification". In: *Hydrology and Earth System Sciences Discussions* 4.2, pp. 439–473.

Peralta, M., S. Gonzalez, A. Carpinelli & A. Kühne (1979): "Suelos y erosión". In: *Perspectivas de desarrollo de los recursos de la Región Aysén del General Carlos Ibañez del Campo*. Ed. by IREN-CORFO.

Quadrelli, R. & J. Wallace (2004): "A simplified linear framework for interpreting patterns of Northern Hemisphere wintertime climate variability". In: *Journal of Climate* 17, pp. 3728–3744.

Quintanilla, V (2008): "Estado de recuperación del bosque nativo en una cuenca nord-patagónica de Chile, perturbada por grandes fuegos acaecidos 50 años atrás (44º-45º S)". In: *Revista de Geografía Norte Grande* 39, pp. 73–92.

Ragueneau, O., B. Quéguiner & P. Tréguer (1996): "Contrast in biological responses to tidally-induced vertical mixing for two macrotidal ecosystems of western Europe". In: *Estuarine, Coastal and Shelf Science* 42.5, pp. 645–665.

Ramsey, C. (2001): "Development of the radiocarbon calibration program". In: *Radiocarbon* 43.2 A, pp. 355–363.

Rein, B. & F. Sirocko (2002): "In-situ reflectance spectroscopy - analysing techniques for high-resolution pigment logging in sediment cores". In: *International Journal of Earth Sciences* 91.5, pp. 950–954.

— (2003): "In-situ reflectance spectroscopy - analysing techniques for high-resolution pigment logging in sediment cores". In: *International Journal of Earth Sciences* 92.1, pp. 143–143.

Renberg, I. & M. Wik (1985): "Soot Particle Counting in Recent Lake Sediments - An Indirect Dating Method". In: *Ecological Bulletins* 37, pp. 53–57.

Richter, T., S. van der Gaast, B. Koster, A. Vaars, R. Gieles, H. de Stigter, H. De Haas & T. van Weering (2006): "The Avaatech XRF Core Scanner: technical description and applications to NE Atlantic sediments". In: *Geological Society London, Special Publications* 267.1, pp. 39–50.

Rose, N. (2001): "Fly-ash Particles". In: *Tracking Environmental Change Using Lake Sediments*. Ed. by W.M. Last & J. P. Smol. Vol. 1. Springer, pp. 319–349.

Rosenbluth, B., H. A. Fuenzalida & P. Aceituno (1997): "Recent temperature variations in southern South America". In: *International Journal of Climatology* 17.1, pp. 67–85.

Rothwell, R & F. Rack (2006): "New techniques in sediment core analysis". In: p. 33.

Royston, J. (1982): "An extension of Shapiro and Wilk's W test for normality to large samples". In: *Applied Statistics* 31.2, pp. 115–124.

Schnyder, D. (2007): "Handbuch Spectrolino". (unpublished).

Servicio Nacional de Geologia y Mineria, ed. (2004): *Mapa Geológico de Chile: Versión Digital, Escala 1:1,000,000*.

Solomon, S. (2007): *Climate Change 2007: the physical science basis: contribution of Working Group I to the Fourth Assessment Report of the Intergovernmental Panel on Climate Change*. Cambridge University Press.

Spearman, C. (1987): "The proof and measurement of association between two things". In: *The American journal of psychology* 100.3, pp. 441–471.

Stern, C. R., H. Moreno, L. López-Escobar, J. E. Clavero, L. E. Lara, J. A. Naranjo, M. A. Parada & M. A. Skewes (2007): "Chilean Volcanoes". In: *The Geology of Chile*. Ed. by T. Moreno & W. Gibbons. London, pp. 147–178.

Stern, C. (2007): "Holocene tephrochronology record of large explosive eruptions in the southernmost Patagonian Andes". In: *Bulletin of Volcanology* 70.4, pp. 435–454.

Swann, G. (2009): "A comparison of the Si/Al and Si/time wet-alkaline digestion methods for measurement of biogenic silica in lake sediments". In: *Journal of Paleolimnology*, pp. 1–11.

Thompson, D. W. J. & S. Solomon (2002): "Interpretation of Recent Southern Hemisphere Climate Change". In: *Science* 296.5569, pp. 895–899.

Thompson, R. & R. Clark (1989): "Sequence slotting for stratigraphic correlation between cores: theory and practice". In: *Journal of Paleolimnology* 2.3, pp. 173–184.

Thomson, S. (2002): "Late Cenozoic geomorphic and tectonic evolution of the Patagonian Andes between latitudes 42 S and 46 S: An appraisal based on fission-track results from the transpressional intra-arc Liquiñe-Ofqui fault zone". In: *Geological Society of America Bulletin* 114.9, pp. 1159–1173.

Thorarinsson, S. (1949): "Some Tephrochronological Contributions to the Volcanology and Glaciology of Iceland". In: *Geografiska Annaler* 31, pp. 239–256.

Trachsel, M., M. Grosjean, D. Schnyder, C. Kamenik & B. Rein (2010): "Scanning reflectance spectroscopy (380 - 730 nm): a novel method for quantitative highresolution climate reconstructions from minerogenic lake sediments". In: –. (in press).

Turney, C. & J. Lowe (2001): "Tephrochronology". In: *Tracking environmental changes using lake sediments*. Ed. by W. M. Last & J. P. Smol. Vol. 1, pp. 451–471.

Urrutia, R., M. Yevenes & R. Barra (2002): "Determinación de los niveles basales de metales traza en sedimentos de tres lagos andinos de Chile: lagos Chungará, Laja y Castor". In: *Boletin De La Sociedad Chilena De Quimica* 47, pp. 457–467.

Urrutia, R., A. Araneda, F. Cruces, L. Torres, L. Chirinos, H. C. Treutler, N. Fagel, S. Bertrand, I. Alvial, R. Barra & E. Chapron (2007): "Changes in diatom, pollen, and chironomid assemblages in response to a recent volcanic event in Lake Galletué (Chilean Andes)". In: *Limnologica - Ecology and Management of Inland Waters* 37.1, pp. 49–62.

Van Oldenborgh, G., S. Drijfhout, A. Ulden, R. Haarsma, A. Sterl, C. Severijns, W. Hazeleger & H. Dijkstra (2009): "Western Europe is warming much faster than expected". In: *Climate of the Past* 5.1, pp. 1–12.

Veblen, T., T. Kitzberger & A. Lara (1992): "Disturbance and forest dynamics along a transect from Andean rain forest to Patagonian shrubland". In: *Journal of Vegetation Science* 3.4, pp. 507–520.

Villalba, R., M. Grosjean & T. Kiefer (2009): "Long-term multi-proxy climate reconstructions and dynamics in South America (LOTRED-SA): State of the art and perspectives". In: *Palaeogeography, Palaeoclimatology, Palaeoecology* 281.3-4, pp. 175–179.

Vogt, K. A., R. Dahlgren, F. Ugolini, D. Zabowski, E. E. Moore & R. Zasoski (1987): "Aluminum, Fe, Ca, Mg, K, Mn, Cu, Zn and P in Above- and Belowground Biomass. II. Pools and Circulation in a Subalpine Abies amabilis Stand". In: *Biogeochemistry* 4.3, pp. 295–311.

von Gunten, L., M. Grosjean, B. Rein, R. Urrutia & P. Appleby (2009a): "A quantitative high-resolution summer temperature reconstruction based on sedimentary pigments from Laguna Aculeo, central Chile, back to AD 850". In: *Holocene* 19.6, pp. 873–881.

von Gunten, L., M. Grosjean, J. Beer, P. Grob, A. Morales & R. Urrutia (2009b): "Age modeling of young non-varved lake sediments: methods and limits. Examples from two lakes in Central Chile". In: *Journal of Paleolimnology* 42.3, pp. 401–412.

von Gunten, L., M. Grosjean, U. Eggenberger, P. Grob, R. Urrutia & A. Morales (2009c): "Pollution and eutrophication history AD 1800-2005 as recorded in sediments from five lakes in Central Chile". In: *Global and Planetary Change* 68.3, pp. 198–208.

Weltje, G. J. & R. Tjallingii (2008): "Calibration of XRF core scanners for quantitative geochemical logging of sediment cores: Theory and application". In: *Earth and Planetary Science Letters* 274.3-4, pp. 423–438.

Wersin, P., P. Höhener, R. Giovanoli & W. Stumm (1991): "Early diagenetic influences on iron transformations in a freshwater lake sediment". In: *Chemical Geology* 90.3-4, pp. 233–252.

Wik, M. & I. Renberg (1996): "Environmental records of carbonaceous fly-ash particles from fossil-fuel combustion". In: *Journal of Paleolimnology* 15.3, pp. 193–206.

Wolfe, A. P., R. D. Vinebrooke, N. Michelutti, B. Rivard & B. Das (2006): "Experimental calibration of lake-sediment spectral reflectance to chlorophyll a concentrations: methodology and paleolimnological validation". In: *Journal of Paleolimnology* 36.1, pp. 91–100.

Zar, J. H. (1972): "Significance Testing of the Spearman Rank Correlation Coefficient". In: *Journal of the American Statistical Association* 67.339, pp. 578–580.

Zolitschka, B., J. Mingram, S. Gaast, J. Jansen & R. Naumann (2002): "Sediment logging techniques". In: *Tracking environmental change using lake sediments*. Ed. by J.P. Last W.M. & Smohl. Springer, pp. 137–153.

A. Appendix

Table A.1: List of all elements acquired by XRF core scanning. Columns represent the voltage required to measure the corresponding element count rates.

10 kV	30 kV	50 kV
Al	Zn	Ag
Si	Br	Sn
P	Rb	Te
S	Sr	Ba
Cl	Zr	
K	Mo	
Ca	Pb	
Ti	Bi	
V		
Cr		
Mn		
Fe		
Rh		

Table A.2: Raw data of the Pb-210-dated subset of samples from core CAS-09-3A obtained from Eawag Dübendorf.

sample [No.]	average depth [cm]	Ra-226 [Bq / kg]	Cs-137 [Bq / kg]	Pb-210 [Bq / kg]	2-sigma error [Bq / kg]
1	0.25	0.00	16.13	109.00	31.27
3	1.25	0.00	5.67	97.55	59.32
4	1.75	0.00	14.27	39.89	75.42
5	2.25	0.00	16.38	83.03	73.22
6	2.75	0.00	16.48	0.00	0.00
7	3.25	0.00	17.67	59.84	64.39
8	3.75	0.00	10.41	37.49	59.76
10	4.75	0.00	8.55	52.93	55.34
11	5.25	0.00	6.00	46.00	65.82
12	5.75	0.00	3.61	0.00	0.00
14	6.75	0.00	5.41	54.73	45.93
16	7.75	0.00	0.00	0.00	0.00
18	8.75	0.00	3.88	24.00	42.02
21	10.25	0.00	3.00	39.00	30.75
22	10.75	0.00	0.00	24.00	42.38
42	20.75	0.00	0.00	0.00	0.00
44	21.75	11.89	3.59	3.21	22.53

Table A.3: Sample data for the determination of conventional XRF analyses at 5 mm resolution. Samples marked with an asterisk belong to the second set of glass pills. Note that the LOI was determined from the source material that was used to prepare both sets of glass pills.

id (core name + tephra number + sampling range [cm below sediment surface])	LOI [%]	pill weight [g]	powder pill (P) or glass pill (G)
CAS-09-1A-T1-xrf (31.9–32.5)	0.59	6.4522	G
CAS-09-1A-T2-xrf (36.5–37.1)	0.70	6.2284	G
CAS-09-1A-T3-xrf (47.5–49.0)	0.87	6.3175	G
CAS-09-1A-T4-xrf-G (68.0–69.0)	4.10	–	G
CAS-09-1A-T4-xrf-P (67.5–69.4)	4.27	4.8761	P
CAS-09-3A-T1-xrf (32.5–33.0)	0.39	6.4100	G
CAS-09-3A-T2-xrf (36.5–37.1)	0.35	6.0744	G
CAS-09-3A-T3-xrf (43.2–44.0)	0.53	6.1528	G
CAS-09-1A-T1-xrf* (31.9–32.5)	0.59	5.1084	G
CAS-09-1A-T2-xrf* (36.5–37.1)	0.70	6.4389	G
CAS-09-1A-T3-xrf* (47.5–49.0)	0.87	6.2336	G
CAS-09-3A-T1-xrf* (32.5–33.0)	0.39	6.836	G
CAS-09-3A-T2-xrf* (36.5–37.1)	0.35	6.884	G
CAS-09-3A-T3-xrf* (43.2–44.0)	0.53	6.3733	G

Table A.4: Data base for the stratigraphic correlation of CAS-09-1A with CAS-09-3A with the help of the in-situ reflectance specroscopy ratio $\frac{R_{700}}{R_{675}}$ for the lead-210 dated segment of CAS-09-3A. Rows in bold indicate depths at which the cores were matched.

CAS-09-1A		CAS-09-3A	
total sediment depth [cm]	$\frac{R_{700}}{R_{675}}$	depth below sediment surface [cm]	$\frac{R_{700}}{R_{675}}$
0.00	**1.202997565**	**0.00**	**1.182971353**
0.20	1.190618693	0.20	1.175383314
0.40	1.155376917	0.40	1.161861295
0.60	1.148258767	0.60	1.146542848
0.80	1.143556662	0.80	1.122996766
1.00	1.105766214	1.00	1.10335667
1.20	1.09998881	1.20	1.10003158
1.40	1.102829239	1.40	1.098160825
1.60	1.076340124	1.60	1.095525026
1.80	**1.084859401**	**1.80**	**1.078291948**
2.00	1.083670091	1.98	1.094561875
2.20	1.093947631	2.16	1.080216515
2.40	1.097026496	2.35	1.077244796
2.60	1.079503708	2.53	1.080362213
2.80	1.092471889	2.71	1.068988616
3.00	1.117750614	2.89	1.096154599
3.20	1.113016284	3.07	1.093744085
3.40	1.108548205	3.25	1.046256217
3.60	1.10706271	3.44	1.078139976
3.80	1.125112236	3.62	1.086769116
4.00	**1.12438444**	**3.80**	**1.099792769**
4.20	1.116249594	4.02	1.101472181
4.40	1.111625448	4.24	1.088632791

(continued on next page)

(continued from last page)

CAS-09-1A		CAS-09-3A	
total sediment depth	$\frac{R_{700}}{R_{675}}$	total sediment depth	$\frac{R_{700}}{R_{675}}$
4.60	1.106983019	4.47	1.089289263
4.80	1.107289175	4.69	1.090135895
5.00	1.104506796	4.91	1.101375757
5.20	1.112400219	5.13	1.09656404
5.40	1.11546956	5.36	1.089009236
5.60	1.113952154	5.58	1.07957112
5.80	**1.100581389**	**5.80**	**1.067800494**
6.00	1.110081886	6.00	1.085746293
6.20	1.122354224	6.20	1.091836362
6.40	1.116582519	6.40	1.089340877
6.60	1.11131499	6.60	1.083734785
6.80	1.09922699	6.80	1.082740956
7.00	1.104610667	7.00	1.091203782
7.20	**1.107276456**	**7.20**	**1.093919852**
7.40	1.103921638	7.36	1.090723575
7.60	1.097785116	7.51	1.080694662
7.80	1.096876026	7.67	1.093400002
8.00	1.09314514	7.83	1.096354281
8.20	1.085678494	7.99	1.088801916
8.40	1.078063385	8.14	1.093430121
8.60	1.078322533	8.30	1.092226438
8.80	1.080448029	8.46	1.096144967
9.00	1.074924223	8.61	1.088465276
9.20	1.070970116	8.77	1.082764172
9.40	1.06127357	8.93	1.078562913
9.60	1.062345409	9.09	1.069983617
9.80	1.069958351	9.24	1.07082986
10.00	**1.07170144**	**9.40**	**1.051092299**

Table A.5: Aggregated semiquantitative results of the XRF analysis of both glass pills and the powder pill (CAS-09-1A-T4 only). Results of the glass pills correspond to averages of the results of the two measurement series CAS-09-XA-TX-xrf and CAS-09-XA-TX-xrf*. Depth of the corresponding samples as indicated in Figure A.3. All values given in percent (LOI in weight percent; cf. section 4.6).

	CAS-09-3A-T1	CAS-09-3A-T2	CAS-09-3A-T3	CAS-09-1A-T1	CAS-09-1A-T2	CAS-09-1A-T3	CAS-09-1A-T4
SiO_2	51.765	53.705	53.920	53.700	55.740	56.235	64.0100
TiO_2	0.997	1.210	1.305	1.275	1.185	1.525	0.4860
Al_2O_3	19.795	19.010	18.280	18.420	18.380	17.050	15.6500
Fe_2O_3	7.020	7.240	7.520	7.535	7.145	7.945	2.6400
MnO	0.114	0.119	0.125	0.127	0.124	0.135	0.0864
MgO	6.000	4.340	4.410	4.550	3.905	3.705	1.1800
CaO	8.905	7.780	7.730	7.675	7.055	6.520	2.0700
K_2O	0.822	1.210	1.159	1.180	1.365	1.325	3.100
Na_2O	3.445	4.150	4.145	4.155	3.895	4.185	4.2600
P_2O_5	0.414	0.567	0.580	0.574	0.556	0.687	0.1020
Cr_2O_3	0.023	0.013	0.013	0.018	0.014	0.010	NA
Rb_2O	0.004	0.006	0.005	0.006	0.006	0.007	0.0094
SrO	0.074	0.073	0.068	0.069	0.068	0.061	0.0217
Y_2O_3	0.001	0.002	0.003	0.003	0.002	0.003	0.0051
ZrO_2	0.024	0.030	0.030	0.029	0.036	0.034	0.0625
CuO	0.001	0.002	0.005	0.005	0.006	0.005	NA
Cs_2O	0.080	0.043	0.078	0.088	0.067	0.064	0.0120
V_2O_5	0.030	0.044	0.034	0.041	0.034	0.048	0.0100
BaO	0.153	0.133	0.172	0.204	0.152	0.175	0.1270
CeO_2	0.075	0.030	0.041	0.030	0.056	0.025	0.0120

(continued on next page)

(continued from last page)

	CAS-09-3A-T1	CAS-09-3A-T2	CAS-09-3A-T3	CAS-09-1A-T1	CAS-09-1A-T2	CAS-09-1A-T3	CAS-09-1A-T4
Nd_2O_3	0.025	0.011	0.022	0.011	0.025	0.020	0.0062
PbO	0.016	0.016	0.017	0.017	0.015	0.017	0.0035
WO_3	NA	0.002	0.005	0.003	0.003	0.004	0.0036
HfO_2	0.004	NA	NA	0.008	NA	0.005	NA
Ta_2O_5	0.003	NA	0.005	NA	0.003	0.004	NA
SO_3	0.088	0.123	0.145	0.124	0.069	0.103	0.026
Cl	0.145	0.120	0.155	0.150	0.074	0.091	0.111
Co_3O_4	0.003	NA	0.003	0.005	0.002	0.001	0.010
ZnO	0.009	0.012	0.014	0.011	0.014	0.013	0.007
Ga_2O_3	0.003	NA	0.002	0.002	NA	NA	0.002
MoO_3	0.005	0.009	0.007	0.009	0.009	0.005	NA
In_2O_3	0.008	NA	0.007	0.006	0.004	NA	NA
Sb_2O_3	NA	NA	0.011	0.004	NA	NA	NA
TeO_2	0.008	NA	0.017	0.008	0.012	0.015	NA
Bi_2O_3	0.004	0.004	0.004	0.002	0.003	0.003	NA
sum	100.013	99.989	100.012	100.026	100.015	100.017	NA
LOI	0.390	0.350	0.530	0.590	0.700	0.870	4.271

Table A.6: List of Spearman rank correlation coefficients ρ for a chosen set of measures. The test statistic was calculated with the two-tailed t-test. Significant correlations at the 80 % level ($\alpha = 0.2$) are printed in bold, significant correlations at the 90 % level ($\alpha = 0.1$) are printed in bold italics. The significance of the correlations was adapted for the corrected degrees of freedom of the corresponding measured value (see text in section 3.12). Note that the climate reanalysis dataset only covers a fraction of the time span of all measured parameters.

measured parameter	climate parameter	Spearman's rho	t-test statistic
Mn / Fe	annual T	***-0.1121***	1.7985
Mn / Fe	DJF T	**-0.0324**	1.4058
Mn / Fe	JJA T	-0.0907	1.1998
Mn / Fe	annual P	***-0.1885***	-1.7793
Mn / Fe	DJF P	**-0.1510**	-1.5972
Mn / Fe	JJA P	**-0.2147**	-1.4741
Mn / Fe	annual SAM	***-0.1480***	1.7863
Mn / Fe	annual PDO	0.2219	0.2589
Mn / Fe	annual ENSO	0.2077	0.2800
Al / Fe	annual T	***0.0680***	1.7528
Al / Fe	DJF T	**-0.1082**	1.3197
Al / Fe	JJA T	0.3358	1.1798
Al / Fe	annual P	***-0.1279***	-1.7738
Al / Fe	DJF P	**-0.1870**	-1.5911
Al / Fe	JJA P	**-0.1799**	-1.4693
Al / Fe	annual SAM	***-0.2765***	1.6460
Al / Fe	annual PDO	-0.0035	0.2331
Al / Fe	annual MEI	-0.0932	0.2490

(continued on next page)

(continued from last page)

measured parameter	climate parameter	Spearman's rho	t-test statistic
Ca / Fe	annual T	-0.6188	1.0666
Ca / Fe	DJF T	-0.4031	0.4997
Ca / Fe	JJA T	-0.6171	0.8317
Ca / Fe	annual P	**0.6300**	-1.5738
Ca / Fe	DJF P	**0.5582**	-1.3872
Ca / Fe	JJA P	**0.4073**	-1.2909
Ca / Fe	annual SAM	-0.2678	0.5615
Ca / Fe	annual PDO	-0.2750	-0.0385
Ca / Fe	annual MEI	-0.1886	-0.0478
Al / Ti	annual T	***-0.3327***	1.8132
Al / Ti	DJF T	**-0.1263**	1.3701
Al / Ti	JJA T	**-0.3914**	1.3287
Al / Ti	annual P	**0.4845**	-1.3738
Al / Ti	DJF P	0.3416	-1.1588
Al / Ti	JJA P	0.4466	-1.0482
Al / Ti	annual SAM	**-0.1212**	1.5357
Al / Ti	annual PDO	-0.1458	0.5705
Al / Ti	annual MEI	-0.1634	0.6010
Ca / Ti	annual T	**-0.4426**	1.5870
Ca / Ti	DJF T	-0.1540	1.1052
Ca / Ti	JJA T	-0.6362	1.2289
Ca / Ti	annual P	0.6052	-1.2573
Ca / Ti	DJF P	0.5231	-1.0445
Ca / Ti	JJA P	0.5185	-0.9439
Ca / Ti	annual SAM	-0.0422	1.2035
Ca / Ti	annual PDO	-0.1919	0.4828
Ca / Ti	annual MEI	-0.1505	0.4976

(continued on next page)

(continued from last page)

measured parameter	climate parameter	Spearman's rho	t-test statistic
BSi flux (0.2)	annual T	0.7465	0.2074
BSi flux (0.2)	DJF T	0.7227	0.2142
BSi flux (0.2)	JJA T	0.6207	0.2246
BSi flux (0.2)	annual P	-0.7223	0.1557
BSi flux (0.2)	DJF P	-0.6462	0.1700
BSi flux (0.2)	JJA P	-0.4086	0.3126
BSi flux (0.2)	annual SAM	0.3856	0.3311
BSi flux (0.2)	annual PDO	0.5619	0.3270
BSi flux (0.2)	annual MEI	0.2224	0.6575
Mean grain size (0.2)	annual T	-0.7873	-0.2057
Mean grain size (0.2)	DJF T	-0.7643	-0.2111
Mean grain size (0.2)	JJA T	-0.6261	-0.2763
Mean grain size (0.2)	annual P	0.7693	-0.2681
Mean grain size (0.2)	DJF P	0.6960	-0.2978
Mean grain size (0.2)	JJA P	0.4140	-0.4090
Mean grain size (0.2)	annual SAM	-0.3794	-0.4346
Mean grain size (0.2)	annual PDO	-0.7074	-0.1663
Mean grain size (0.2)	annual MEI	-0.4202	-0.2246
C / N	annual T	***0.2038***	-3.0886
C / N	DJF T	***0.1092***	-2.4962
C / N	JJA T	***0.1438***	-2.7133
C / N	annual P	***-0.2135***	2.4910
C / N	DJF P	***-0.2119***	2.4794
C / N	JJA P	0.2464	0.6954
C / N	annual SAM	***0.4607***	-4.8454
C / N	annual PDO	-0.4899	0.3017
C / N	annual MEI	-0.4421	-0.3141

(continued on next page)

(continued from last page)

measured parameter	climate parameter	Spearman's rho	t-test statistic
C flux	annual T	**0.3726**	-1.6139
C flux	DJF T	***0.7098***	-1.7867
C flux	JJA T	***0.5047***	-1.6857
C flux	annual P	***-0.7822***	2.1919
C flux	DJF P	***-0.5344***	1.9797
C flux	JJA P	-0.4086	0.7791
C flux	annual SAM	***0.7773***	-2.7787
C flux	annual PDO	0.0142	0.4589
C flux	annual MEI	0.2221	-0.0651
N flux	annual T	**0.4870**	-1.6701
N flux	DJF T	***0.7249***	-1.8195
N flux	JJA T	***0.5991***	-1.7301
N flux	annual P	***-0.8113***	2.2604
N flux	DJF P	***-0.6330***	2.0660
N flux	JJA P	-0.5560	0.8048
N flux	annual SAM	***0.6077***	-2.8825
N flux	annual PDO	0.1207	0.4831
N flux	annual MEI	0.3021	-0.0558

Declaration

under Art. 28 Para. 2 RSL 05

Last, first name:	Wartenburger, Richard
Matriculation number:	08-129-595
Programme:	MSc in Climate Sciences Master Thesis
Thesis title:	A paleoenvironmental Reconstruction from Lago Cástor, North Patagonian Andes
Thesis supervisor:	Martin Grosjean

I hereby declare that this submission is my own work and that, to the best of my knowledge and belief, it contains no material previously published or written by another person, except where due acknowledgement has been made in the text. In accordance with academic rules and ethical conduct, I have fully cited and referenced all material and results that are not original to this work. I am well aware of the fact that, on the basis of Article 36 Paragraph 1 Letter o of the University Law of 5 September 1996, the Senate is entitled to deny the title awarded on the basis of this work if proven otherwise.

Bern, 08/07/2010

Richard Wartenburger

Unterschrift